University of Alberta

Numerical Modeling of the Thermal Interaction between a Low Reynolds Number Viscous Flow and a Shape Memory Alloy Undergoing Shape Change

by

Michael Steven Joseph Wojcichowsky ©

A thesis submitted to the Faculty of Graduate Studies and Research in partial fulfillment of the requirements for the degree of Master of Science.

Department of Mechanical Engineering

Edmonton, Alberta
Spring 2003

National Library
of Canada

Acquisitions and
Bibliographic Services

395 Wellington Street
Ottawa ON K1A 0N4
Canada

Bibliothèque nationale
du Canada

Acquisitions et
services bibliographiques

395, rue Wellington
Ottawa ON K1A 0N4
Canada

Your file Votre référence

Our file Notre référence

The author has granted a non-exclusive licence allowing the National Library of Canada to reproduce, loan, distribute or sell copies of this thesis in microform, paper or electronic formats.

L'auteur a accordé une licence non exclusive permettant à la Bibliothèque nationale du Canada de reproduire, prêter, distribuer ou vendre des copies de cette thèse sous la forme de microfiche/film, de reproduction sur papier ou sur format électronique.

The author retains ownership of the copyright in this thesis. Neither the thesis nor substantial extracts from it may be printed or otherwise reproduced without the author's permission.

L'auteur conserve la propriété du droit d'auteur qui protège cette thèse. Ni la thèse ni des extraits substantiels de celle-ci ne doivent être imprimés ou autrement reproduits sans son autorisation.

0-612-82365-2

Canadä

University of Alberta

Library Release Form

Name of Author: Michael Steven Joseph Wojcichowsky

Title of Thesis: Numerical Modeling of the Thermal Interaction between a Low Reynolds Number Viscous Flow and a Shape Memory Alloy Undergoing Shape Change

Degree: Master of Science

Year this Degree Granted: 2003

Permission is hereby granted to the University of Alberta to reproduce single copies of this thesis and to lend or sell such copies for private, scholarly, or scientific research purposes only.

The author reserves all other publication and other rights in association with the copyright in the thesis, and except as hereinbefore provided, neither the thesis nor any substantial portion thereof may be printed or otherwise reproduced in any material form whatever without the author's prior written permission.

M. W Jan. 22, 2003

Michael Steven Joseph
Wojcichowsky
15812 80 Street
Edmonton,AB
Canada, T5Z 2V2

The Laws of Thermodynamics for Dummies: You can't win. You can't break even. And you can't get out of the game.

—Anon

The most exciting phrase to hear in science, the one that heralds new discoveries is not "Eureka!! I've found it!", but "That's funny...."

—Isaac Asimov

University of Alberta

Faculty of Graduate Studies and Research

The undersigned certify that they have read, and recommend to the Faculty of Graduate Studies and Research for acceptance, a thesis entitled Numerical Modeling of the Thermal Interaction between a Low Reynolds Number Viscous Flow and a Shape Memory Alloy Undergoing Shape Change submitted by Michael Steven Joseph Wojcichowsky in partial fulfillment of the requirements for the degree of Master of Science.

Dr. J. Yokota (Supervisor)

Dr. P. Steffler

Dr. W. Moussa

Date Jan. 22, 2003

To my parents

ABSTRACT

A numerical scheme that models the thermal fluid-solid interaction between a low Reynold's number viscous flow and a shape memory alloy (SMA) undergoing shape change has been developed. The phase change of the SMA is modeled by the temperature dependance of the thermal conductivity, and the dependance of the shape of the solid on the average cross-sectional phase. Physically accurate boundary conditions are presented that allow for the investigation of shape change on the actuation behaviour of SMA wires.

The scheme automatically satisfies the geometric conservation law, a consequence of moving boundary and deforming grid problems. Therefore saving computational effort, since it need not be advanced through time as though it is a physical transport equation.

Results indicate that shape change has a considerable effect on actuation behaviour. Actuator designers can use shape change to control actuation times, which depend upon the path of shape change and the actual engineered shapes.

ACKNOWLEDGEMENTS

I would firstly like to extend my sincerest thanks to my supervisor Jeff W. Yokota. His incredible knowledge and experience in the fields of fluid dynamics and numerical methods made this work possible.

Secondly, I would like to acknowledge Dr. Jonathan Mark Janus, who was generous enough to send me a copy of his master's thesis.

I would also like to thank my lab mates, and fellow suckers for punishment, Marty Lastiwka and Chris Sideroff for keeping things interesting over the last two years. They have become life long friends. I will always remember the good times out at the pub and the countless hours spent challenging each other's skill at Starcraft.

I would also like to say that I owe my parents an enormous debt of gratitude. They taught me the value of hard work, and their love and support has always given me the drive to excel.

Finally, I would like to thank the Natural Sciences and Engineering Research Council of Canada for financially supporting this work through a PGS A scholarship.

CONTENTS

1 Introduction **1**
- 1.1 Shape Memory Alloys 1
- 1.2 Moving Boundaries, Deforming Grids, and the Geometric Conservation Law 6

2 Problem Description **9**

3 Governing Equations **12**
- 3.1 General Form of Equations 12
- 3.2 Governing Equations in the Fluid Region 14
  - 3.2.1 Boussinesq Approximation 14
  - 3.2.2 Simplification of Conservation of Mass 15
  - 3.2.3 Simplification of Momentum 16
  - 3.2.4 The Vorticity Transport Equation 17
  - 3.2.5 Simplification of the Energy Equation 19
  - 3.2.6 Conservation Form of the Equations 20
  - 3.2.7 Velocity Decomposition 21
- 3.3 Governing Equations in the Solid Region 23
  - 3.3.1 Equations of Motion 23
  - 3.3.2 Property Model of Shape Memory Alloys 25
  - 3.3.3 Mathematical Representation of Phase 28
  - 3.3.4 Modeling of the Thermal Conductivity 31
  - 3.3.5 Latent Heat of Transformation 32
  - 3.3.6 Energy Equation in the Solid Revisited 33
- 3.4 Nondimensionalization of the Equations 34
- 3.5 Transformation to Generalized Coordinates and the Geometric Conservation Law 37
  - 3.5.1 Transformations and the Jacobian 37

3.5.2 Transformation of Conservation of Mass 41
3.5.3 Transformation of the Vorticity Transport and Energy Equations 42
3.5.4 Transformation of the Energy Equation in the Solid . . 49

4 Numerical Formulation **50**
4.1 Solution Sequence 50
4.2 Solution of the Energy Equation in the Solid 53
4.2.1 Discretization of Energy Equation 53
4.2.2 Iterative Time Integration Scheme of the Energy Equation in the Solid 58
4.2.3 Newton Iteration Solution of Temperature 60
4.3 Solution of the Vorticity and Energy Transport Equations in the Fluid 61
4.3.1 Discretization of the Model Equation 61
4.3.2 Construction of the Convective Terms 64
4.3.3 Construction of the Diffusive Terms 66
4.3.4 Second Order Accurate Multistage Time Integration of the Transport Equations 68
4.4 Convergence of the Viscous Stream Function 69
4.4.1 Approximate LU Factorization 70
4.4.2 Multigrid Convergence Acceleration 74
4.5 Numerical Stability and the Global Timestep 78
4.6 Numerical Domain 79
4.6.1 Initial Grid Construction 84
4.6.2 Grid Generation Procedure for Changing Grid 90
4.6.3 Solid Grid Generation 93
4.7 Boundary Conditions 93
4.7.1 Periodic Boundary 93
4.7.2 Inflow Boundary 94
4.7.3 Outflow Boundary 94
4.7.4 Solid Boundary 95
4.7.5 Thermal Interaction Boundary Condition 100

5 Results **103**
5.1 Fluid and Solid Material Properties 103
5.2 Initial Periodic Flow Field 105
5.3 Constant Geometry Test Cases 112

5.3.1 Simulation of 0.5mm Diameter SMA Wire 112
5.3.2 Comparison to a Lumped Heat Capacitance Model . . 122
5.3.3 Simulation of 0.7mm Diameter SMA wire 128
5.4 SMA Wires Undergoing Shape Change 130
5.4.1 Shape Change from Small Diameter to Large Diameter Cross-Section 130
5.4.2 Shape Change from Large Diameter to Small Diameter Cross-section 139
5.4.3 Shape Change from Circular Cross-section to an Elliptic Cross-section 142

6 Conclusions **150**

LIST OF FIGURES

2.1 Problem Domain 10

3.1 Shear Deformation of a Monocrystal Undergoing Transformation between Austenite and Martensite 26
3.2 Mapping from (x, y) to (ξ, η) Coordinate System 37
3.3 Space-Time Grid Cell 38

4.1 Computational Finite Volume Grid Cell 54
4.2 Multigrid Grid Levels 75
4.3 Schematic of Three Level 'W' Cycle used in Multigrid Scheme 78
4.4 Developed Grid in Fluid Domain 82
4.5 Developed Grid in Solid Domain 83
4.6 O-Grid Mapping to Computational Space 84
4.7 Unsmoothed Grid in the Fluid Domain 88
4.8 Smoothed Grid in the Fluid Domain 89
4.9 Constructed Grid Around Elliptical SMA 92
4.10 Solid Boundary Cell 96
4.11 Heat Transfer at Boundary Cell 101

5.1(a) Vorticity Contours in Fluid Region, t = 0.008s 107
5.1(b) Vorticity Contours in Fluid Region, t = 0.016s 108
5.1(c) Vorticity Contours in Fluid Region, t = 0.024s 109
5.1(d) Vorticity Contours in Fluid Region, t = 0.032s 110
5.1(e) Vorticity Contours in Fluid Region, t = 0.040s 111
5.2(a) Temperature Contours of 0.5mm Diameter Constant Geometry, t = 0.02s 115
5.2(b) Temperature Contours of 0.5mm Diameter Constant Geometry, t = 0.03s 116
5.2(c) Temperature Contours of 0.5mm Diameter Constant Geometry, t = 0.04s 117

5.2(d) Temperature Contours of 0.5mm Diameter Constant Geometry, t = 0.05s 118
5.2(e) Temperature Contours of 0.5mm Diameter Constant Geometry, t = 0.06s 119
5.3 Average Temperature History for 0.5mm Diameter Constant Geometry 120
5.4 Average Phase History for 0.5mm Diameter Constant Geometry 121
5.5 Comparison Between Lumped Heat Capacitance and 2D Temperature Histories 126
5.6 Comparison Between Lumped Heat Capacitance and 2D Phase Histories 127
5.7 Comparison Between Constant Geometry Phase Histories . 129
5.8(a) Small Circle to Large Circle Vorticity Contours, t = 0.008s 133
5.8(b) Small Circle to Large Circle Vorticity Contours, t = 0.016s 134
5.8(c) Small Circle to Large Circle Vorticity Contours, t = 0.024s 135
5.8(d) Small Circle to Large Circle Vorticity Contours, t = 0.032s 136
5.8(e) Small Circle to Large Circle Vorticity Contours, t = 0.040s 137
5.9 Comparison Between Constant and Changing Geometry Phase Histories 138
5.10 Comparison Between Constant and Changing Geometry Phase Histories 141
5.11(a) Circle to Ellipse Vorticity Contours, t = 0.002s 144
5.11(b) Circle to Ellipse Vorticity Contours, t = 0.012s 145
5.11(c) Circle to Ellipse Vorticity Contours, t = 0.022s 146
5.11(d) Circle to Ellipse Vorticity Contours, t = 0.032s 147
5.11(e) Circle to Ellipse Vorticity Contours, t = 0.042s 148
5.12 Comparison Between Circle to Circle and Circle to Ellipse Changing Geometry Phase Histories 149

NOMENCLATURE

LATIN SYMBOLS

A_f^o	Austenite transformation finish temperature
A_s^o	Austenite transformation start temperature
$\vec{b}$	Specific body force
c	Wave speed
c_p	Specific heat capacity
$\tilde{D}$	Strain rate tensor
e	Specific internal energy
$G(T)$	Phase function for SMA
g	Gravitational acceleration
Gr	Grashof number
H	Specific latent heat of transformation
J	Jacobian of the transformation
J_{2D}	2D Jacobian of the transformation
k	Thermal conductivity
L	Reference length

L	Lower diagonal implicit operator
M_f^o	Martensite transformation finish temperature
M_s^o	Martensite transformation start temperature
N	Time level
$\vec{n}$	Unit vector normal to surface W
$P(T)$	Phase function for SMA
P	Pressure
Pe	Peclet number
Pr	Prantl number
$\vec{q}$	Heat flux
$\vec{R}$	Surface force
r	Relaxation parameter
Re	Reynolds number
S	Normal distribution standard deviation
T	Temperature
T_∞	Freestream temperature
$\tilde{T}$	Symmetric Cauchy stress tensor
U	Transformed contravariant ξ velocity
U_∞	Freestream velocity
U	Lower diagonal implicit operator
u	x velocity
V	Transformed contravariant η velocity
v	y velocity
$\vec{v}$	Velocity vector (2D)
W	Control volume surface
(x, y, t)	Eulerian coordinates in space and time

GREEK SYMBOLS

α_i	Multi-step stage coefficient
β	Volumetric thermal expansion coefficient
Δt	Time step
δ	Difference operator; δ^+ forward, δ^- backward, δ central
δ_{ij}	Kronecker delta matrix
λ	Implicit parameter
μ	Viscosity
ν	Kinematic viscosity
ξ	Austenitic volume fraction
ρ	Density
σ_e	Effective stress
τ_{ij}	Viscous stress tensor
ϕ	Irrotational potential
ψ	Viscous correction stream function
Ω	Control volume
ω	Vorticity
(ξ, η, τ)	Computational coordinates in space and time

CHAPTER 1

INTRODUCTION

1.1 Shape Memory Alloys

Shape memory alloys (SMA's) are a unique group of metals that have the ability to 'remember' their shape after large deformations [8], [47]. This ability is known as the shape memory effect (SME) and was first discovered over 50 years ago in a gold-cadmium alloy [26]. In the 1960's it was discovered in alloys of nickel and titanium [10], [40], [58] and alloys using other materials were discovered later [29], [60]. Nickel-titanium alloys are still the most common, due to the fact that they tend to exhibit the most desirable combination of material properties [35].

The shape memory effect (SME) is due to the fact that SMA's exist in two distinct solid crystalline phases. The global shape change is a direct result of the different microscopic crystal structure at each of these solid phases. Therefore each engineered shape of the SMA corresponds to a solid phase [46]. SMA's can be trained to change form from one shape to another only once and stay there permanently, known as the one-way effect; or the SMA can be trained to change between two shapes over and over, known as the two-way effect [39]. The two solid phases are referred to as austenite (the high temperature phase) and martensite (the low temperature phase). The mechanism of phase change is through either a change in temperature or a change in the applied stress. The phase transformation is analogous to the phase transformation of water to ice, except that it is a non-isothermal solid to solid transformation [46].

Current SMA's are capable of sustaining recoverable strains of up to 10% depending on the exact composition of the alloy [26]. The alloy composition also has a very large effect on the temperatures at which phase transformation occurs, and on the thermodynamic properties such as conductivity and heat capacitance [1], [5].

The usefulness of SMA's is in their ability to change shape in response to external temperature changes and applied stress. This has led to a large amount of research into a wide range of applications for SMA's. The most promising applications include the shape control of lifting surfaces in aerodynamic bodies [3], [4], biomedical applications [50], [13], [51], vibration control [43], and as actuators in mechanical systems [1], [18], [28], [32], [54].

Research into the design of SMA actuators generally falls into four main categories: constitutive modeling, experimental determination of SMA mechanical properties, determination of and the influence of changing thermal and electrical properties, and modelling of the heat transfer between the SMA and its surrounding environment [6]. The current work is of the fourth category, an investigation into the effect of two-dimensional shape change on the thermal fluid-solid interaction of an SMA wire and a viscous cross flow.

Constitutive modeling, which is by far the most extensive area of research, is the attempt to develop analytical models to describe the behaviour of shape memory alloys. A detailed description of the various models can be found in Birman [8]. These constitutive models describe in detail the relationships between stress (σ), strain (ϵ), temperature (T), and phase (ξ).

The current constitutive models can readily be applied to one-dimensional predictions of overall length change of an SMA wire. They can also describe the thermal behaviour of SMA's in multiple dimensions. They unfortunately do not provide a relationship between local shape and phase in a multi-dimensional sense. Although the exact relationship between multidimensional shape and local phase of an SMA is not known, it is of interest to designers to understand the effect that shape change might have on the prediction of transient actuation behaviour of SMA wires. The goal of the current work is not to develop a new consitutive model, therefore the existing constitutive model proposed by Bhattacharyya and Lagoudas [5] will be used to describe the thermal behaviour of the SMA, and a simple idealized shape change model will be used to determine the shape.

Experimental determination of SMA mechanical properties has also been extensively investigated. This research involves the experimental determination of mechanical constants as well as stress-strain relationships and fatigue properties at various temperatures, and for various alloys. Representative works in this area are those of Miller and Lagoudas [36], and Shaw and Kyriakides [47].

The thermal and electrical properties of SMA's are highly sensitive to the phase. Experimental and numerical studies have been performed that investigate both the nature of and the effect of changing material propeties on actuation behaviour of SMA's. Faulkner *et al* [20] developed experimental methods to determine the phase dependance of the thermal conductivity and electrical resistivity. Numerical studies that accounted for changing material properties include Amalraj *et al* [1], Bhattacharyya *et al* [7], and Reaume [42]. These studies show the importance of including changing material property models, therefore the current work includes a changing property model similar to Reaume [42].

Recently research has been done that numerically investigated the transient behaviour of SMA wires undergoing phase change, where the phase change is driven by heat transfer to a surrounding environment. Most of these numerical investigations use the lumped heat capacitance assumption. This means that the temperature of the SMA was assumed to be uniform throughout, and the heat transfer to the environment was modeled using a heat transfer coefficient. These investigations can be found in Bhattacharyya *et al* [6], Faulkner *et al* [20], Shahin *et al* [46], and Matsuzaki *et al* [34]. The main problem with this method is the determination of a heat transfer coefficient that mimics the real multidimensional problem. The heat transfer coefficient is a single constant parameter that is supposed to account for all of the thermodynamic effects due to conditions in the boundary layer, surface geometry, fluid properties, and transport properties [22]. To perform a numerical calculation that accounts for shape change, it would be difficult to find a heat transfer coefficient that could capture the true fluid-solid interaction.

Amalraj *et al* [1] performed a numerical simulation on a one-dimensional wire, thus moving away from the lumped heat capacitance assumption. However, the boundary conditions on the SMA were set to be convective and again employed a heat transfer coefficient. Reaume [42] was the first to fully eliminate the use of a heat transfer coefficient by accurately modeling the flow field around an infinitely long two-dimensional SMA wire cross-section in cross flow.

From the literature, none of the previous work in this field has attempted to capture the effect of two dimensional shape change on the thermal fluid-solid interaction between an SMA and its surrounding environment and is the focus of the current work. This work continues the work of Reaume [42] by developing new numerical techniques that accommodate for the two-dimensional cross-sectional shape change of SMA wires. Thus allowing the study of the effect of shape change on the transient actuation behaviour of SMA wires.

1.2 Moving Boundaries, Deforming Grids, and the Geometric Conservation Law

Free and moving boundary problems occur in a variety of physical situations. Typical moving boundary situations include solid-liquid phase change problems, fluid and structure interaction, and free surface flows [49]. The combination of fluid flow and moving boundaries interacting with that flow increase the complexity of computationally simulating those situations.

Computational solutions of transient thermo-fluid problems are often performed on domains that are discretized into a boundary fitted grid of finite volumes. By virtue of the boundary movement, the entire grid itself must move and deform as the simulation evolves. Therefore each individual finite volume is not stationary with respect to the continuum being modeled.

Thomas and Lombard [52] first noted that in addition to the three physical conservation equations of mass, momentum, and energy, a fourth equation must be satisfied, in problems with deforming grids, to avoid spurious source terms. These source terms manifested themselves as large flow errors, oscillations, and instabilities. This fourth equation was the so-called geometric conservation law (GCL), sometimes called the Jacobian transport equation [49]. The GCL has been the focus of much research over the last twenty years since its discovery [19]. The GCL is merely a consequence of the finite volume method of solving the transport equations, and is by no means due to the actual physics of the problem. The GCL has a simple geometric interpretation, namely, that the rate of change of the volume of a grid cell equals the algebraic sum of volumes swept by the faces of that control volume, thus total volume is conserved. Hence the name geometric conservation law [49].

Thomas and Lombard [52] satisfied the geometric conservation law by calculating the volume of the grid cell at the next time increment, using the same time-marching scheme used to solve the physical transport equations. What this means is that the volume of a grid cell at any given time is not calculated from the position of the grid at that time, but updated in time as if it is a physical transport equation [49].

Demirdžić and Perić [15] [16] along with Shyy *et al* [49] showed how they could implicitly satisfy the GCL. This is done by computing all of the grid cell volumes using the grid points at the given time-step, and computing the grid velocities at the faces of the control volume in such a way that the discrete form of the GCL is satisfied. Zwart and Raithby [66] later showed that satisfying the GCL this way is, in essence, applying a finite volume treatment to an integrated space-time grid cell.

The two methods of ensuring geometric conservation described above represent the two main schools of thought and are the current state of the art. Examples which employ the first method can be found in [52], [49], [33], [25], [17]. Examples which employ the second method can be found in [15], [16], [49], [66], [19], [48].

In the current work the solid boundaries of the shape memory alloy wire are moving due to the shape change. A boundary fitted grid is used to solve the appropriate conservation equations in both the fluid and the solid, therefore GCL satisfaction is of extreme importance. A numerical scheme has been developed that automatically satisfies the GCL. Therefore the GCL will not be treated as a physical transport equation. Automatic satisfaction is numerically more efficient in that the Jacobian transport equation is not time advanced, therefore only the three physical conservation equations are being solved, one less than the method of Thomas and Lombard [52]. This follows closely with the philosophy of the second method of GCL satisfaction described above [15] [16] [49].

In addition to automatic GCL satisfaction, boundary conditions that accurately capture the motion of the solid boundaries have been developed and applied to the numerical approximation. These boundary conditions are vital in that they are the numerical source of the unsteadiness in the fluid-solid interaction and undoubtedly have a substantial influence on the heat transfer between the SMA and the fluid.

CHAPTER 2

PROBLEM DESCRIPTION

The purpose of the current work was to develop a numerical technique that models the interaction between a shape memory alloy (SMA) and a low Reynolds number viscous flow. The numerical technique developed here is unique in that it takes into account the physical effect the shape change has on both the fluid and the solid. The numerical technique developed will be demonstrated with a particular numerical experiment described below.

Consider an infinite cascade of SMA wires in a cross flow, illustrated in Figure (2.1). The wires themselves are infinitely long in the third dimension. Infinitely long wires allow for the assumption that 3D effects are negligible. The assumption of a 2D flow field is common in numerical calculations since it greatly reduces the computational cost. This is valid as long as the desired effects are captured in the 2D plane.

The SMA wires are initially in their low temperature or martensitic phase, at an initial temperature of 273K. The local phase of the SMA wire will be calculated in the solid domain. Mathematically the phase will be represented by the variable ξ, with $\xi = 0$ representing fully martensitic phase and $\xi = 1$

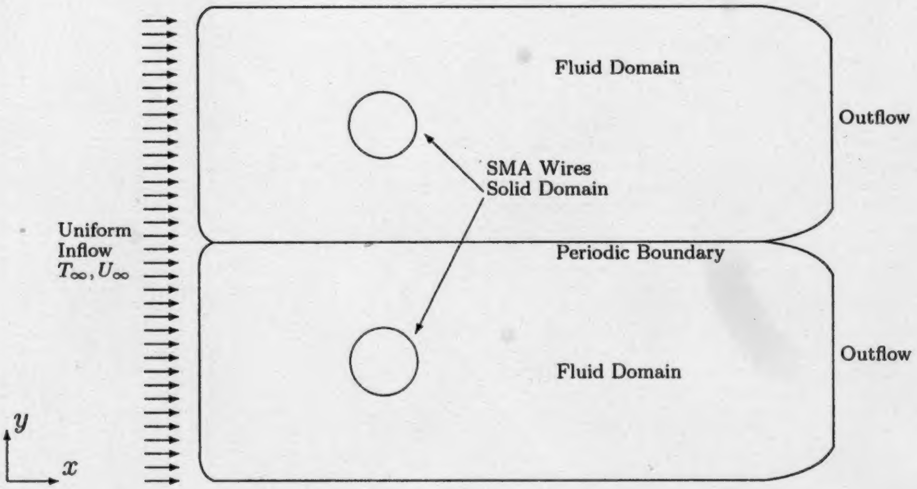

Figure 2.1: Problem Domain

representing fully austenitic phase, and $0 < \xi < 1$ indicating partial phase change. The measure of actuation will be defined by the area weighted average cross-sectional phase, ξ_{av}, with $\xi_{av} = 0$ indicating zero actuation and $\xi_{av} = 1$ indicating full actuation. The fluid is incompressible and viscous, with a free stream velocity of $U_\infty = 0.1$m/s, and free stream temperature of $T_\infty = 310$K.

The warm viscous fluid will transiently heat the SMA wires, thus causing them to actuate and change phase from martensite to austenite. The focus of the current work is to allow the cross-sectional shape of the SMA wires to change as they actuate. Unfortunately there is not a detailed theoretical or empirical model for the relationship between phase and local shape change in the literature. However, it is still important for designers to have an understanding as to the effect that shape change might have. Therefore, an idealized model between global cross-sectional shape and the average cross-sectional phase is used. This model consists of allowing a parameter of the shape, generally the diameter, change with average phase. The cross-sectional area will be allowed to change shape between two similar geometries, namely a large diameter circle to a small diameter circle, and the diameter will be linearly dependant upon average phase. It will also be allowed to change between two dissimilar geometries, namely a small diameter circle to an elliptical shape, and the major axis length will be linearly dependant upon average phase. The effect that these shape changes have on the actuation behaviour is the primary interest.

It is obvious that as the cross-sectional area changes, the solid boundary will impart momentum to the flow. This will transiently affect the flow field and ultimately influence the rate of heat transfer into the solid. The actuation rate and behaviour of the SMA wire will likely be influenced by a change in heat transfer rates. The developed numerical technique will shed light on this influence.

The real value of the developed numerical scheme is to provide actuator designers some insight into the effect that the thermal fluid-solid interaction has on the prediction of SMA actuation behaviours. In addition, the developed code will give designers the ability to explore the effect that different engineered cross-sections will have on those actuation behaviours.

CHAPTER 3

GOVERNING EQUATIONS

3.1 General Form of Equations

The equations which are relevant to this problem are the conservation of mass, momentum and energy. They are shown below in integral form for a volume Ω bounded by a surface W:

$$\frac{D}{Dt}\iiint\limits_{\Omega} \rho\, d\Omega = \iiint\limits_{\Omega} \left[\frac{D\rho}{Dt} + \rho\nabla\cdot\vec{v}\right] d\Omega = 0 \tag{3.1}$$

$$\frac{D}{Dt}\iiint\limits_{\Omega} \rho\vec{v}\, d\Omega = \iiint\limits_{\Omega} \rho\vec{b}\, d\Omega + \iint\limits_{W} \vec{R}\, dW \tag{3.2}$$

$$\begin{aligned}\frac{D}{Dt}\iiint\limits_{\Omega} \rho(e + \frac{1}{2}(\vec{v}\cdot\vec{v}))\, d\Omega = -\iint\limits_{W}(\vec{n}\cdot\vec{q})\, dW \quad &+ \quad \iint\limits_{W}(\vec{R}\cdot\vec{v})\, dW \\ &+ \quad \iiint\limits_{\Omega} \rho(\vec{b}\cdot\vec{v})\, d\Omega\end{aligned} \tag{3.3}$$

(For definitions of the variables used, please see the Nomenclature section at the beginning of the text.)

Assuming that $\vec{R} = \vec{n}\cdot\tilde{T}$ (where $\tilde{T}$ is the symmetric Cauchy stress tensor) and by applying Gauss' Theorem and the Reynolds Transport Theorem [38]

[45] to the above equations it is possible to write them in differential form (both vector and tensor notation are shown).

$$\frac{\partial \rho}{\partial t} + \nabla \cdot (\rho \vec{v}) = 0 \quad ; \quad \frac{\partial \rho}{\partial t} + (\rho v_i)_{,i} = 0 \tag{3.4}$$

$$\rho \frac{D\vec{v}}{Dt} = \rho \vec{b} + \nabla \cdot \tilde{T} \quad ; \quad \rho \frac{Dv_i}{Dt} = \rho b_i + \frac{\partial T_{ji}}{\partial x_j} \tag{3.5}$$

$$\rho \frac{De}{Dt} = -\nabla \cdot \vec{q} + \tilde{T} : \tilde{D} \quad ; \quad \rho \frac{De}{Dt} = -q_{i,i} + T_{ij} D_{ij} \tag{3.6}$$

Where:

$$\tilde{D} = D_{ij} = \frac{1}{2}\left(\frac{\partial v_i}{\partial x_j} + \frac{\partial v_j}{\partial x_i}\right)$$

is the strain rate tensor. Assuming that the stress tensor is comprised of two parts: $T_{ij} = -P\delta_{ij} + \tau_{ij}$. Where P is the pressure and τ_{ij} is the viscous stress tensor the conservation of mass, momentum, and energy equations become:

$$\frac{\partial \rho}{\partial t} + (\rho v_i)_{,i} = 0 \tag{3.7}$$

$$\rho \frac{Dv_i}{Dt} = \rho b_i - \frac{\partial P}{\partial x_i} + \frac{\partial \tau_{ji}}{\partial x_j} \tag{3.8}$$

$$\rho \frac{De}{Dt} = -q_{i,i} - P(\frac{\partial v_i}{\partial x_i}) + \tau_{ij}(\frac{\partial v_i}{\partial x_j}) \tag{3.9}$$

It is also assumed that only conservative body forces are present (and in particular only gravity will be considered). The differential form of the equations is desirable because it allows for easier manipulation of the equations. However, their above form is very general and can be applied to a wide range of problems. The following sections describe the modification of the equations such that they better suit the problem being considered.

3.2 Governing Equations in the Fluid Region

3.2.1 Boussinesq Approximation

The fluid equations will be simplified by employing the Boussinesq approximation. Boussinesq first pointed out that in low speed incompressible fluid dynamics problems, natural convection can be modeled by allowing changes in density to be applied only in the body force term of the momentum equation. These density variations are very small and due only to moderate variations in the temperature of the fluid (not pressure) [11], [24], [57]. This is done to model the influence of natural convection due to thermal gradients in the flow. This approximation is valid when the size of the coefficient of volumetric expansion (β) is small. It is generally in the range of 10^{-3} to 10^{-4} for fluids being considered in this work. To apply the Boussinesq approximation we must first assume an incompressible flow, with the added assumption that the density (ρ) in the body force term can vary slightly. In addition ρ is only a function of temperature (T). By expanding the Taylor series with respect to temperature, and ignoring second order and higher terms we get:

$$\rho(T) = \rho_o + \frac{d\rho}{dT}dT \tag{3.10}$$

Knowing that the coefficient of volumetric expansion is [22]:

$$\beta \equiv -\frac{1}{\rho}\left.\frac{\partial\rho}{\partial T}\right|_P \tag{3.11}$$

We can write the following knowing that density is only a function of temperature:

$$\beta \equiv -\frac{1}{\rho}\left.\frac{\partial\rho}{\partial T}\right|_P = -\frac{1}{\rho}\frac{d\rho}{dT} \tag{3.12}$$

Applying this to Equation (3.10) we get:

$$\rho(T) = \rho_o - \rho_o \beta dT \tag{3.13}$$

Using the approximation $dT = \Delta T$ we arrive at:

$$\rho(T) = \rho_o(1 - \beta \Delta T) \tag{3.14}$$

Equation (3.14) now becomes the density equation of state for the fluid. Since β is in the range 10^{-3} to 10^{-4} moderate changes in T result in small changes in ρ. Values for β and ρ_o used in this work are $\beta = 0.361 \times 10^{-3}\mathrm{K}^{-1}$ and $\rho_o = 1050\frac{\mathrm{kg}}{\mathrm{m}^3}$, the estimated thermal expansion coefficient and density of blood at 37°C [22]. The current work began with a code by Reaume [42]. That work modeled the transient heating of an SMA wire in a cross-flow where the fluid was blood at 37°C. The current work uses the same fluid properties for comparison purposes.

The assumption that the fluid equation of state is only dependent on temperature means that $\rho \neq f(P)$. This assumption requires that the fluid flow must have small enough Mach numbers ($Ma < 0.3$) such that pressure will not cause density gradients. Approximating the speed of sound to be that of blood at 37°C ($v_{sound} = 1480\frac{\mathrm{m}}{\mathrm{s}}$) and a background flow velocity of $0.1\frac{\mathrm{m}}{\mathrm{s}}$, gives a Mach number of, $Ma = 6.8 \times 10^{-5}$. This is well below the limiting Mach number.

3.2.2 Simplification of Conservation of Mass

As stated in the previous section one of the major assumptions we apply to the basic equations is incompressibility. The incompressiblity assumption is valid because of the extremely low Mach number ($Ma = 6.8 \times 10^{-5}$) flow being modeled. By applying this to the conservation of mass (3.4) we get:

$$\rho_o \frac{\partial v_i}{\partial x_i} = 0 \qquad ; \qquad \rho_o \nabla \cdot \vec{v} = 0 \tag{3.15}$$

3.2.3 Simplification of Momentum

The first simplification applied to the momentum equation (3.8) is the assumption of a Newtonian fluid with constant viscosity. It is understood that blood is often modeled with a varying viscosity. The model often used is that of a Casson fluid [56]. Viscosity will not be modeled in this manner since the rheology of the fluid is not the primary interest of the current work; the thermal interaction between the fluid and solid is the primary interest. A constant viscosity is a reasonable first approximation. The viscous stress tensor is defined as:

$$\tau_{ij} = -\frac{2}{3}\mu \frac{\partial v_k}{\partial x_k}\delta_{ij} + \mu\left(\frac{\partial v_i}{\partial x_j} + \frac{\partial v_j}{\partial x_i}\right) \tag{3.16}$$

By applying continuity (3.15) the first term goes to zero and the following can be shown to be true:

$$\frac{\partial \tau_{ji}}{\partial x_j} = \mu v_{i,jj} \qquad ; \qquad \nabla \cdot \tilde{\tau} = \mu \nabla^2 \vec{v} \tag{3.17}$$

The second simplification applied is the assumption that only conservative body forces are present; and gravity is the only one. Gravity can be written as a potential:

$$b_i = -\frac{\partial (gy)}{\partial x_i} \qquad ; \qquad \vec{b} = -\nabla (gy) \tag{3.18}$$

Applying equations (3.17) and (3.18) to (3.8) we get:

$$\rho\frac{Dv_i}{Dt} = -\rho\frac{\partial(gy)}{\partial x_i} - \frac{\partial P}{\partial x_i} + \mu v_{i,jj} \quad ; \quad \rho\frac{D\vec{v}}{Dt} = -\rho\nabla(gy) - \nabla P + \mu\nabla^2\vec{v} \tag{3.19}$$

The final simplification applied to the momentum equation is the Boussinesq approximation. To apply the Bousinesq approximation fully we only treat density as a variable in the body force term. Substituting Eqn. (3.14) into the body force term of Eqn.(3.19) we get:

$$\rho_o\frac{Dv_i}{Dt} = -(\rho_o - \rho_o\beta\Delta T)\frac{\partial(gy)}{\partial x_i} - \frac{\partial P}{\partial x_i} + \mu v_{i,jj} \tag{3.20}$$

It can be seen from the above equation that when temperature changes are on the order of 10^0, the accelerations due to natural convection are on the order of $10^{-4}\frac{\mathrm{m}}{\mathrm{s}^2}$. Although small, the motion due to natural convection is included for completeness. By dividing out the density (ρ_o) Eqn.(3.20) reduces to:

$$\begin{aligned}\frac{Dv_i}{Dt} &= -(1-\beta\Delta T)\frac{\partial(gy)}{\partial x_i} - \frac{1}{\rho_o}\frac{\partial P}{\partial x_i} + \frac{\mu}{\rho_o}v_{i,jj} \\ \frac{D\vec{v}}{Dt} &= -(1-\beta\Delta T)\nabla(gy) - \frac{1}{\rho_o}\nabla P + \frac{\mu}{\rho_o}\nabla^2\vec{v}\end{aligned} \tag{3.21}$$

3.2.4 The Vorticity Transport Equation

The next major step in deriving the equations in the fluid region is to convert the momentum equation (3.21) to the vorticity transport equation. This is done to eliminate pressure as an independent variable. So we take the curl of Eqn. (3.21) (Note that $\nu = \frac{\mu}{\rho_o}$):

$$\nabla \times \frac{D\vec{v}}{Dt} = \nabla \times \left[-(1-\beta\Delta T)\nabla(gy) - \frac{1}{\rho_o}\nabla P + \nu\nabla^2\vec{v}\right] \tag{3.22}$$

Carrying through we get (in tensor notation recall that ϵ_{mni} is the permutation tensor) :

$$\begin{aligned}
\frac{\partial \omega_m}{\partial t} + \frac{\partial \omega_m}{\partial x_l} v_l + \frac{\partial v_l}{\partial x_l} \omega_m - \frac{\partial \omega_q}{\partial x_q} v_m &- \frac{\partial v_m}{\partial x_q} \omega_q \\
= \epsilon_{mni} \beta g \frac{\partial T}{\partial x_n} \frac{\partial y}{\partial x_i} &- \frac{1}{\rho_o} \epsilon_{mni} \frac{\partial}{\partial x_n} \left(\frac{\partial P}{\partial x_i} \right) + \nu \omega_{m,jj} \\
\frac{\partial \vec{\omega}}{\partial t} + (\vec{v} \cdot \nabla) \vec{\omega} + \vec{\omega} (\nabla \cdot \vec{v}) - \vec{v} (\nabla \cdot \vec{\omega}) &- (\vec{\omega} \cdot \nabla) \vec{v} \\
= \beta g (\nabla T \times \nabla y) &- \frac{1}{\rho_o} (\nabla \times \nabla P) + \nu \nabla^2 \vec{\omega} \quad (3.23)
\end{aligned}$$

We can see that the third term on the left hand side is zero by conservation of mass (3.15). The fourth term on the left hand side is also zero since it represents the divergence of the curl of velocity. The fifth term is also zero since we only have a 2D flow domain, so vorticity (ω) only has a (z or $q = 3$) component, and velocity has (x, y or $q = 1, 2$) components. Finally the second term on the right hand side is zero since it represents the curl of the gradient of pressure, thus eliminating pressure as an independent variable from the equation. So the vorticity transport equation finally takes the form:

$$\begin{aligned}
\frac{D\omega_m}{Dt} &= \epsilon_{mni} \beta g \frac{\partial T}{\partial x_n} \frac{\partial y}{\partial x_i} + \nu \omega_{m,jj} \\
\frac{D\vec{\omega}}{Dt} &= \beta g \nabla T \times \nabla y + \nu \nabla^2 \vec{\omega} \qquad (3.24)
\end{aligned}$$

It can be seen in the equation above (3.24) that the Boussinesq approximation allows the same benefits of an incompressibility assumption, while providing for some vorticity generation due to buoyancy forces induced by the natural convection of heat. This equation is commonly used in the study of viscous flows with natural convective heat transfer effects [31], [37], [58], [57], [41].

3.2.5 Simplification of the Energy Equation

Starting with the energy equation (3.9):

$$\rho\frac{De}{Dt} = -q_{i,i} - P(\frac{\partial v_i}{\partial x_i}) + \tau_{ij}(\frac{\partial v_i}{\partial x_j})$$

The first major assumption applied to the energy equation in the fluid is that internal energy (e) exactly equals the heat capacity multiplied by the temperature ($e = c_p T$). This changes the primitive or independent variable in the energy equation to temperature (T). Heat conduction in the energy equation will be modeled using Fourier's law ($\vec{q} = -k\nabla T$). Also the viscous heating term in Eq. (3.6) ($\tau_{ij}\frac{\partial v_i}{\partial x_j}$) will be neglected as a first approximation [31], since the heat transfer due to the convection from the solid will tend to be several orders of magnitude higher than the heat generation due to viscous friction. In fact it is only for high Mach number flows or high speed friction flows (as in lubricating oils) that viscous heating may not be neglected [22]. An additional test to determine whether viscous heating can be neglected is by computing the Eckert number (Ec). The Eckert number is defined as Ec $= \frac{U_\infty^2}{c_p(T-T_\infty)}$, where U_∞ is the freestream velocity, c_p is the thermal heat capacity, and $T - T_\infty$ is the difference between the surface temperature and the freestream temperature. If the Eckert number is small the viscous heating can be neglected [22]. Using the initial solid temperature as T, the Eckert number for the current flow is $Ec = 7 \times 10^{-8}$, thus confirming the assumption to neglect viscous heating. Finally the ($P\frac{\partial v_i}{\partial x_i}$) term is zero because of continuity. Applying these to (3.9) we get:

$$\rho \frac{D(c_p T)}{Dt} = \frac{\partial}{\partial x_i}\left(k \frac{\partial T}{\partial x_i}\right) \quad ; \quad \rho \frac{D(c_p T)}{Dt} = \nabla(k \nabla T) \tag{3.25}$$

Since the flow regime is incompressible and has a low Reynolds number (Re), changes in heat capacity (c_p) and thermal conductivity (k) would be due to relatively large thermal changes. And since only moderate temperature variations are expected, constant c_p and k values are assumed. So the energy equation becomes :

$$\rho c_p \frac{DT}{Dt} = kT_{,ii} \quad ; \quad \rho c_p \frac{DT}{Dt} = k \nabla^2 T \tag{3.26}$$

Recall that the assumption of an incompressible flow is employed, thus $\rho = \rho_o$ in the above equation. Therefore the final form of the energy equation is :

$$\rho_o c_p \frac{DT}{Dt} = kT_{,ii} \qquad ; \qquad \rho_o c_p \frac{DT}{Dt} = k \nabla^2 T \tag{3.27}$$

Note that the material properties used in this work are those used by Reaume [42] and are that of blood at 37°C, so $c_p = 3.85 \times 10^3 \frac{\mathrm{J}}{\mathrm{kgK}}$, $k = 0.5 \frac{\mathrm{W}}{\mathrm{mK}}$, and $\rho_o = 1050 \frac{\mathrm{kg}}{\mathrm{m}^3}$.

3.2.6 Conservation Form of the Equations

The three governing equations of conservation of mass, vorticity transport, and energy (3.15, 3.24, and 3.27 respectively) will now be written in strong conservation form and expanded into the cartesian coordinates x and y. Strong conservation form is useful in that all variables appear inside either time or space derivatives.

The conservation of mass, Equation (3.15), is easily transformed into strong conservation form by dividing density (ρ_o) out of the equation. Note that for simplicity fluid density (ρ_o) will from this section onward be simply given the Greek symbol ρ. Conservation of mass becomes:

$$\frac{\partial u}{\partial x} + \frac{\partial v}{\partial y} = 0 \tag{3.28}$$

Expanding out the material derivatives of vorticity and energy, as well as writing in cartesian coordinates we get:

$$\frac{\partial \omega}{\partial t} + u\frac{\partial \omega}{\partial x} + v\frac{\partial \omega}{\partial y} = \beta g\frac{\partial T}{\partial x} + \nu\left(\frac{\partial^2 \omega}{\partial x^2} + \frac{\partial^2 \omega}{\partial y^2}\right) \tag{3.29}$$

$$\frac{\partial T}{\partial t} + u\frac{\partial T}{\partial x} + v\frac{\partial T}{\partial y} = \frac{k}{c_p\rho}\left(\frac{\partial^2 T}{\partial x^2} + \frac{\partial^2 T}{\partial y^2}\right) \tag{3.30}$$

By applying conservation of mass ($\frac{\partial u}{\partial x} + \frac{\partial v}{\partial y} = 0$) we can move the u and v velocities into the spatial derivatives. The vorticity and energy equations become:

$$\frac{\partial \omega}{\partial t} + \frac{\partial (u\omega)}{\partial x} + \frac{\partial (v\omega)}{\partial y} = \beta g\frac{\partial T}{\partial x} + \nu\left(\frac{\partial^2 \omega}{\partial x^2} + \frac{\partial^2 \omega}{\partial y^2}\right) \tag{3.31}$$

$$\frac{\partial T}{\partial t} + \frac{\partial (uT)}{\partial x} + \frac{\partial (vT)}{\partial y} = \frac{k}{c_p\rho}\left(\frac{\partial^2 T}{\partial x^2} + \frac{\partial^2 T}{\partial y^2}\right) \tag{3.32}$$

The above equations (3.28), (3.31), and (3.32) are the equations that will be solved in the fluid domain.

3.2.7 Velocity Decomposition

Since the momentum equation was transformed into the vorticity transport equation (Equation 3.31), velocity is no longer a primitive variable in the equations of motion. Velocity does not appear inside a time derivative, therefore the cartesian u and v velocities are not advanced through time explicitly. To construct the cartesian velocities an inviscid potential-viscous stream function decomposition is employed. The decomposition involves separating the velocities into an inviscid potential flow and a viscous correction [64].

$$u = U_\infty + \frac{\partial \phi}{\partial x} - \frac{\partial \psi}{\partial y} \tag{3.33}$$

$$v = \frac{\partial \phi}{\partial y} + \frac{\partial \psi}{\partial x} \tag{3.34}$$

Where ϕ is an irrotational potential, ψ is the viscous correction stream function, and U_∞ is the background free stream velocity.

In two dimensions the vorticity can be written as:

$$\omega = \frac{\partial v}{\partial x} - \frac{\partial u}{\partial y} \tag{3.35}$$

Applying Equations (3.33) and (3.34) we are left with a relationship between ψ and ω:

$$\omega = \frac{\partial^2 \psi}{\partial x^2} + \frac{\partial^2 \psi}{\partial y^2} \tag{3.36}$$

This elliptic equation will be used to compute the viscous stream function from the vorticity at each time step.

By applying Equations (3.33) and (3.34) to the conservation of mass, Equation (3.28), we get:

$$\frac{\partial^2 \phi}{\partial x^2} + \frac{\partial^2 \phi}{\partial y^2} - \frac{\partial^2 \psi}{\partial y \partial x} + \frac{\partial^2 \psi}{\partial x \partial y} = 0 \tag{3.37}$$

Analytically the mixed partial derivatives of ψ cancel one another out. Numerically there is some truncation error associated with the construction of each of these two terms, which may not cancel out. This truncation error could potentially violate continuity if the two ψ derivatives are dropped. Thus for completeness, the equation that is used to construct the inviscid potential keeps these two terms as source terms. Therefore ensuring that there is no violation of continuity whatsoever by the streamfunction terms. The resulting equation used to construct the inviscid potential is:

$$\frac{\partial^2\phi}{\partial x^2} + \frac{\partial^2\phi}{\partial y^2} = \frac{\partial^2\psi}{\partial y\partial x} - \frac{\partial^2\psi}{\partial x\partial y} \tag{3.38}$$

To satisfy conservation of mass, the above elliptic partial differential equation must also be solved every timestep.

3.3 Governing Equations in the Solid Region

3.3.1 Equations of Motion

The solid region of the domain is a shape memory alloy with changing geometry. The shape change of the solid will induce some Eulerian velocities in the cross-section of the SMA wire. To compute these velocities the momentum equation (3.8) and the continuity equation (3.7) would need to be solved in the solid. This would require a detailed model of the behaviour of the viscous stress tensor (τ_{ij}) in two dimensions, in addition to a detailed relationship between local shape change and local phase. As discussed earlier, the material science has yet to provide the detailed mathematical models that are required to perform these calculations, and the development of a new constitutive model is beyond the scope of the current work. Therefore, as a first approximation, the Eulerian velocities (v_i) will be assumed to be zero, and continuity and momentum, Equations (3.8) and (3.7) respectively, will not be solved in the solid. However, it will be shown later that the shape change will be mathematically felt through the grid point velocities in the transformation of the energy equation to generalized coordinates. Eulerian velocities of zero reduce the energy equation (3.9) to (Note that since $v_i = 0$ the material time derivative reduces to a partial derivative):

$$\rho \frac{\partial e}{\partial t} = -q_{i,i} \tag{3.39}$$

Once again applying Fourier's law ($\vec{q} = -k \nabla T$) we get (in both tensor and vector notation):

$$\rho \frac{\partial e}{\partial t} = \frac{\partial}{\partial x_i}\left(k \frac{\partial T}{\partial x_i}\right) \quad ; \quad \rho \frac{\partial e}{\partial t} = \nabla \cdot (k \nabla T) \tag{3.40}$$

Unlike the fluid region, the solid region cannot be assumed to have constant thermal conductivity (k), as SMA's change phase from martensite to austenite or vice versa the thermal conductivity can change by an order of magnitude [42], [1]. It also cannot be assumed that specific internal energy (e) is exactly the thermal heat capacity (c_p) multiplied by the temperature (T). Accompanying the sensible energy of temperature change there must also be a latent energy term caused by the transformation of phase (ξ) from martensite to austenite [1], [5], [42]. The modeling of the shape memory alloy properties will be explained in the subsequent sections.

3.3.2 Property Model of Shape Memory Alloys

Shape memory alloys (SMA's) exist in two distinct solid states or phases, depending on the stress and temperature to which it is subjected. The difference between the two solid phases is characterized by a different microscopic crystal structure. These two material phases are referred to as austenite (sometimes called the parent phase or the high temperature phase) and martensite (sometimes called the child phase or the low temperature phase). The phase names are not references to the different phases of steel. They are only used to indicate the relative temperature at which the specific phase exists [60].

The shape memory effect (SME) is the process in which a SMA is mechanically "trained" to return to its original shape when heated above its transformation temperature. The SME is a direct result of the different crystal structure at each of the two phases. If an initially austenitic SMA is loaded such that the SMA undergoes a stress induced phase change (see Figure 3.1) at an ambient temperature between the austenitic start temperature (A_s^o) and the martensitic start temperature (M_s^o), the SMA will retain its deformed shape [9]. It in essence remembers its old austenitic shape, even though it is in a new configuration. The deformed shape is due to the shear deformation at the microscopic level of a single monocrystal, illustrated in Figure (3.1), [8]. Due to this shear there is little total volume change of an SMA undergoing shape change, therefore it is assumed that there is no net density change, i.e. ρ is constant in the solid [1] [5] [6].

When heated the single SMA crystal changes phase and shape back to its original austenitic crystal configuration. In turn the global macroscopic

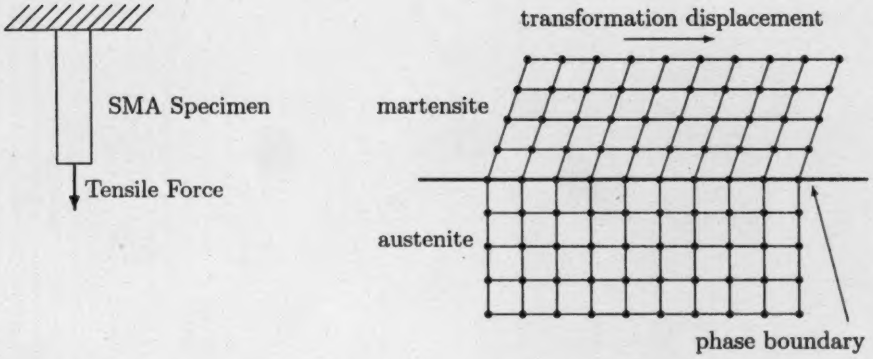

SMA Monocrystal

Figure 3.1: Shear Deformation of a Monocrystal Undergoing Transformation between Austenite and Martensite

shape of the SMA specimen returns to its austenitic shape. This is a single cycle of the SME. If upon cooling the SMA retains the austenitic shape (i.e. it doesn't change shape again), it is called the one-way effect. It is possible to train SMA specimens to repeat the shape change process, changing between two trained shapes, this is known as the two-way effect [39].

The austenitic phase can transform into several variants of the martensitic phase. All of the martensitic variants have identical crystal structure, but differ from one another by a rigid body rotation. When phase change is induced by applying stress to the SMA, the variants that are oriented in such a way that they displace in the direction of loading are the ones that form. This process is known as martensitic de-twinning. The macroscopic or global shape change is due to the sum of all the small monocrystal shear deformations. This is the micromechanical cause of shape change in

SMA's. If martensite is formed by a purely thermal transformation (i.e. not stress induced) then the variants formed are random, and no net global length change results, therefore no shape memory effect. This is known as a self-accommodating martensitic transformation. The present work assumes shape change, therefore detwinned martensite is the initial state of the SMA.

Individual monocrystals of SMA undergo stress-free thermal transformations at a single temperature. They only exist in one state at any given temperature, this is known as a first order phase transition [5]. Polycrystals are a cluster of monocrystals, and their thermal behaviour is different than any single monocrystal in the cluster. Polycrystals tend to change phase in a more gradual manner, not at a single temperature. They have transformation start and finish temperatures indicating that they can exist in partial phase change; existing at some mixture of austenite and martensite phases. This is due to some of the monocrystals being in austenitic phase and some of the monocrystals being in martensitic phase. The reasons for the difference in behaviour are discussed by Bhattacharyya and Lagoudas [5]. One of the major reasons is that the transformation temperatures are extremely sensitive to alloying elements. Each individual crystal may have a different alloy composition than the average alloy composition of the entire polycrystal. Therefore parts of the polycrystal change phase at different temperatures, leading to a more gradual poycrystalline phase change.

The present work discretizes the solid domain into small grid cells. The cells are very large compared with the size of the individual monocrystals and therefore are treated as a single polycrystal. Instead of modeling countless individual monocrystals, an entire grid cell will be assumed to be uniform in phase and material properties.

This cell averaged approach has limitations in that it cannot be used to describe a monocrystalline SMA. It can only be applied to problems where the SMA being studied is a polycrystal. The cell averaged material phase model allows for the phase (ξ) of the SMA to exist in varying combinations of austenite and martensite.

The material properties of SMA's are often highly dependent on the phase (ξ) of the sample. The material properties that can be modeled as variable are the thermal conductivity (k), electrical resistivity (ρ_E), and the specific heat capacity (C_p) [1]. In the current work only the thermal conductivity (k) will be modeled as a function of phase, while the density (ρ) and specific heat capacity (C_p) will be assumed constant. This approximation is reasonable since the thermal conductivity (k) in Ni-Ti alloys changes by an order of magnitude from martensite to austenite, where the heat capacity changes by no more than 11% [1], [42]. The density is constant, as discussed earlier, because of the shearing nature of monocrystalline shape change.

3.3.3 Mathematical Representation of Phase

Shape memory alloys are materials that undergo a change in crystal structure (i.e. a solid phase change) in response to applied stress or temperature change. The SMA possesses different material properties in each of its two phases and during phase transformation. Therefore it is of great importance to mathematically represent phase such that the aforementioned material properties can be determined.

Let ξ be the austenitic volume fraction of the SMA. ξ ranges between

0 and 1; when $\xi = 0$ the material is all martensite, when $\xi = 1$ the material is all austenite. Experiments have shown that phase is a function of temperature (T) and stress (σ) [5]. Consider the following representation of phase for a SMA including both temperature (T) and stress (σ), as derived by Bhattacharyya and Lagoudas [5]:

$$\xi_{MA}(T,\sigma) = \int_{As}^{T} G(\hat{T},\sigma)d\hat{T} \tag{3.41}$$

Where:

$$A_s = A_s^o + \frac{\sigma}{D_A} \qquad ; \qquad A_f = A_f^o + \frac{\sigma}{D_A} \tag{3.42}$$

ξ_{MA} is the austenitic volume fraction for the martensite to austenite transformation. A_s is the austenite start temperature and A_f is the austenite finish temperature. Equation (3.42) shows that the start and finish temperatures are functions of the stress free start and finish temperatures (A_s^o and A_f^o) and the effective stress (σ) state of the SMA. D_A is a measure of the stress needed to cause a change in A_s and A_f by 1^oC [42], [5]. It is obvious that the stress state of the SMA has a large effect on its thermal behaviour. The assumption of a zero stress state ($\sigma = o$) is taken in the current work. This greatly simplifies the problem in that we remove stress from the phase model formulation. This is an important limitation since SMA's, when used as actuators, are often required to carry a load.

Equation (3.41) is only for phase transformations from martensite to austenite. An analogous equation exists for the austenite to martensite phase transformation:

$$\xi_{AM}(T,\sigma) = 1 + \int_{Ms}^{T} P(\hat{T},\sigma)d\hat{T} \tag{3.43}$$

Where:

$$M_s = M_s^o + \frac{\sigma}{D_M} \qquad ; \qquad M_f = M_f^o + \frac{\sigma}{D_M} \tag{3.44}$$

Where M_s^o and M_f^o are the martensitic start and finish temperatures respectively. The stress free functional forms of Equations (3.41) and (3.43) are:

$$\xi_{MA}(T) = \int_{A_S^o}^{T} G(\hat{T})d\hat{T} \tag{3.45}$$

$$\xi_{AM}(T) = 1 + \int_{M_S^o}^{T} P(\hat{T})d\hat{T} \tag{3.46}$$

The two functions P and G were experimentally determined to be normal distributions [30], [5]:

$$P(T) = \frac{1}{S\sqrt{2\pi}} \exp\left[-\frac{1}{2}\left[\frac{T - \frac{1}{2}(M_s^o + M_f^o)}{S}\right]^2\right] \tag{3.47}$$

$$G(T) = \frac{1}{S\sqrt{2\pi}} \exp\left[-\frac{1}{2}\left[\frac{T - \frac{1}{2}(A_s^o + A_f^o)}{S}\right]^2\right] \tag{3.48}$$

where $S = 1.5$ is the standard deviation of the normal distribution.

Unfortunately Equations (3.45) and (3.46) cannot be integrated analytically, and the computational cost of numerically integrating these two equations in every grid cell in the solid domain would be very high. Reaume [42] developed approximate functions for these two equations that had a maximum error of 1.05% from the numerically integrated solution. This is considered acceptable considering the savings in computational time. The two functions are:

$$\xi_{MA} = \frac{1}{2}\left(1 + \tanh\left(0.563\left(T - \left(\frac{A_s^o + A_f^o}{2}\right)\right)\right)\right) \tag{3.49}$$

$$\xi_{AM} = \frac{1}{2}\left(1 + \tanh\left(0.563\left(T - \left(\frac{M_s^o + M_f^o}{2}\right)\right)\right)\right) \tag{3.50}$$

In the above equations it should be reiterated that T is the polycrystal's temperature at any given time, and the phase (ξ) is a result of this temperature. All parameters that depend upon phase are ultimately functions of temperature through these two state equations.

3.3.4 Modeling of the Thermal Conductivity

As stated earlier, the thermal conductivity (k) will not be assumed constant with respect to temperature (T). Thermal conductivity of SMA's can vary by an order of magnitude between the martensitic and austenitic phases. It is therefore a function of phase (ξ) and ultimately a function of temperature (T). The values of thermal conductivity at the two states are, $k_M = 1.8\frac{\mathrm{W}}{\mathrm{mK}}$ and $k_A = 18\frac{\mathrm{W}}{\mathrm{mK}}$, [1], [42]. Where the subscripts indicate martensitic (k_M) or austenitic (k_A) thermal conductivities. It is assumed that the thermal conductivity is a linear function of phase (ξ, recalling that $0 \leq \xi \leq 1$), and is similar to an equation for simple mixing [1]:

$$k(\xi) = k_M + \xi(k_A - k_M) \tag{3.51}$$

This is the most common approximation for thermal conductivity from the literature [1], [5], [6], [20]. Applying the approximations for phase, Equations (3.49) and (3.50), to Equation (3.51), we get thermal conductivity as a function of temperature (T):

$$k_{MA} = k_M + \frac{1}{2}\left(1 + \tanh\left(0.563\left(T - \left(\frac{A_s^o + A_f^o}{2}\right)\right)\right)\right)(k_A - k_M) \tag{3.52}$$

$$k_{AM} = k_M + \frac{1}{2}\left(1 + \tanh\left(0.563\left(T - \left(\frac{M_s^o + M_f^o}{2}\right)\right)\right)\right)(k_A - k_M) \quad (3.53)$$

These are the two equations used in the numerical experiment to determine thermal conductivity.

3.3.5 Latent Heat of Transformation

The zero stress transformation of a shape memory alloy's crystal structure requires either a release or an absorption of heat energy. As the SMA changes phase from martensite to austenite latent energy is required to rearrange the crystal structure, as the SMA changes phase from austenite to martensite latent energy is released into the surroundings. A parallel can be drawn between the transformation of water from solid to liquid or liquid to solid. The former requires energy, the latter releases energy. The SMA studied in this work has a latent energy of transformation almost seven times greater than the sensible energy required to change the temperature of the solid through its phase transformation range. Therefore it is necessary to include a latent energy term (H) in the formulation of the specific internal energy (e) [1], [5], [6], [42]:

$$e(T) = c_p T + H\xi(T) \quad (3.54)$$

where c_p is the specific heat capacity, and H is the latent heat of transformation. Once again we can replace the phase (ξ) with the approximations for phase given in Equations (3.49) and (3.50):

$$e_{MA}(T) = c_p T + H\frac{1}{2}\left(1 + \tanh\left(0.563\left(T - \left(\frac{A_s^o + A_f^o}{2}\right)\right)\right)\right) \quad (3.55)$$

$$e_{AM}(T) = c_p T + H\frac{1}{2}\left(1 + \tanh\left(0.563\left(T - \left(\frac{M_s^o + M_f^o}{2}\right)\right)\right)\right) \tag{3.56}$$

These are the two equations in the numerical experiment that will be used to construct the specific internal energy (e).

3.3.6 Energy Equation in the Solid Revisited

Now that the specific internal energy in the solid has been completely defined by Equation (3.54) we can now completely state the energy equation in the solid. By substituting Equation (3.54) into (3.40) and writing it in cartesian coordinates we get:

$$\rho\frac{\partial(c_p T + H\xi(T))}{\partial t} = \frac{\partial}{\partial x}\left(k\frac{\partial(T)}{\partial x}\right) + \frac{\partial}{\partial y}\left(k\frac{\partial(T)}{\partial y}\right) \tag{3.57}$$

By assuming a constant density in the solid we can move ρ into the time derivative leaving us with:

$$\frac{\partial(\rho c_p T + \rho H\xi(T))}{\partial t} = \frac{\partial}{\partial x}\left(k\frac{\partial(T)}{\partial x}\right) + \frac{\partial}{\partial y}\left(k\frac{\partial(T)}{\partial y}\right) \tag{3.58}$$

This is the final form of the energy equation that will be solved in the solid.

It should be noted that the cross-sectional shape (and area) of the solid is changing but the density of the solid remains constant. Therefore, there is an increase in the mass of the solid in the 2D plane as the area of the solid increases (and vice versa). This increase in mass is assumed to come from the third dimension, in other words as the 2D solid increases in area, the length of the solid in the third dimension must get smaller to maintain conservation of mass. This movement of matter into the 2D plane results in an increase in the total energy of the solid in the 2D plane, but will not affect the calculation of the specific internal energy, which is the primitive variable in the energy equation in the solid (3.58).

3.4 Nondimensionalization of the Equations

A common practice in numerical calculations and in fluid dynamics in general is to nondimensionalize the governing equations. This is done such that the relative magnitudes and relative changes in magnitude of variables can be compared to some reference values that are relevant to the experiment. Reference values for velocity, length, and temperature must therefore be chosen in the fluid region. A length of $L = 1\text{mm}$, will be used as the reference length. The freestream velocity of the fluid, U_∞, will be used as the reference velocity. The initial temperature of the solid, $T^{(solid)}_{(initial)}$, will be used as the reference temperature. Using these reference values, the variables in the conservation of mass (3.28), vorticity transport (3.31), and energy (3.32) equations become (Note that the $*$ indicates a dimensionless quantity):

$$\begin{aligned} x^* &= \frac{x}{L};\ y^* = \frac{y}{L};\ t^* = \frac{tU_\infty}{L};\ T^* = \frac{T}{T^{(solid)}_{(initial)}};\ u^* = \frac{u}{U_\infty}; \\ v^* &= \frac{v}{U_\infty};\ \omega^* = \frac{\omega L}{U_\infty} \end{aligned} \tag{3.59}$$

To nondimensionalize the fluid equations (3.28, 3.31, and 3.32), we simply apply the relationships in Equation (3.59) :

$$\frac{\partial u^*}{\partial x^*} + \frac{\partial v^*}{\partial y^*} = 0 \tag{3.60}$$

$$\frac{\partial \omega^*}{\partial t^*} + \frac{\partial (u^*\omega^*)}{\partial x^*} + \frac{\partial (v^*\omega^*)}{\partial y^*} = \frac{\beta g T^{(initial)}_{(solid)} L}{U_\infty}\frac{\partial T^*}{\partial x^*} + \frac{\nu}{U_\infty L}\left(\frac{\partial^2 \omega^*}{\partial x^{*2}} + \frac{\partial^2 \omega^*}{\partial y^{*2}}\right) \tag{3.61}$$

$$\frac{\partial T^*}{\partial t^*} + \frac{\partial (u^*T^*)}{\partial x^*} + \frac{\partial (v^*T^*)}{\partial y^*} = \frac{k}{c_p \rho U_\infty L}\left(\frac{\partial^2 T^*}{\partial x^{*2}} + \frac{\partial^2 T^*}{\partial y^{*2}}\right) \tag{3.62}$$

We can now define the Reynolds number, Prantl number, and Grashof number as:

$$\begin{aligned} Re &= \left[\frac{\rho U_\infty L}{\mu}\right] \\ Pr &= \left[\frac{c_p \mu}{k}\right] \\ Gr &= \left[\frac{g\beta T^{(solid)}_{(initial)} L^3 \rho^2}{\mu^2}\right] \end{aligned} \tag{3.63}$$

Thus our nondimensional equations become:

$$\frac{\partial u^*}{\partial x^*} + \frac{\partial v^*}{\partial y^*} = 0 \tag{3.64}$$

$$\frac{\partial \omega^*}{\partial t^*} + \frac{\partial (u^* \omega^*)}{\partial x^*} + \frac{\partial (v^* \omega^*)}{\partial y^*} = \left[\frac{Gr}{Re^2}\right] \frac{\partial T^*}{\partial x^*} + \left[\frac{1}{Re}\right] \left(\frac{\partial^2 \omega^*}{\partial x^{*2}} + \frac{\partial^2 \omega^*}{\partial y^{*2}}\right) \tag{3.65}$$

$$\frac{\partial T^*}{\partial t^*} + \frac{\partial (u^* T^*)}{\partial x^*} + \frac{\partial (v^* T^*)}{\partial y^*} = \left[\frac{1}{RePr}\right] \left(\frac{\partial^2 T^*}{\partial x^{*2}} + \frac{\partial^2 T^*}{\partial y^{*2}}\right) \tag{3.66}$$

The energy equation in the solid (3.58) requires the nondimensionalization of two additional variables, specific internal energy (e) and thermal conductivity (k). Their nondimensional counterparts are defined as:

$$k^* = \frac{k(T)}{k_M}; \; e^* = \frac{e}{c_p T^{(solid)}_{(initial)}} \tag{3.67}$$

Where k_M is the thermal conductivity of the SMA in its martensitic phase, and the specific heat capacity (c_p) and density (ρ) are for the solid. Applying these to the energy equation in the solid (3.58) we get:

$$\frac{\partial e^*}{\partial t^*} = \frac{k_M}{\rho c_p U_\infty L} \left[\frac{\partial}{\partial x^*}\left(k^* \frac{\partial (T^*)}{\partial x^*}\right) + \frac{\partial}{\partial y^*}\left(k^* \frac{\partial (T^*)}{\partial y^*}\right)\right] \tag{3.68}$$

We can define the Peclet number as :

$$Pe = \left[\frac{\rho c_p U_\infty L}{k_M}\right] \tag{3.69}$$

Where all constants, except for U_∞, are for the solid. Thus our nondimensional equation in the solid becomes:

$$\frac{\partial e^*}{\partial t^*} = \left[\frac{1}{Pe}\right]\left[\frac{\partial}{\partial x^*}\left(k^*\frac{\partial(T^*)}{\partial x^*}\right) + \frac{\partial}{\partial y^*}\left(k^*\frac{\partial(T^*)}{\partial y^*}\right)\right] \tag{3.70}$$

For brevity the '$*$' in the equations will be dropped, and all variables will be assumed nondimensionalized from now on. So the three fluid equations are:

$$\frac{\partial u}{\partial x} + \frac{\partial v}{\partial y} = 0 \tag{3.71}$$

$$\frac{\partial \omega}{\partial t} + \frac{\partial(u\omega)}{\partial x} + \frac{\partial(v\omega)}{\partial y} = \left[\frac{Gr}{Re^2}\right]\frac{\partial T}{\partial x} + \left[\frac{1}{Re}\right]\left(\frac{\partial^2\omega}{\partial x^2} + \frac{\partial^2\omega}{\partial y^2}\right) \tag{3.72}$$

$$\frac{\partial T}{\partial t} + \frac{\partial(uT)}{\partial x} + \frac{\partial(vT)}{\partial y} = \left[\frac{1}{RePr}\right]\left(\frac{\partial^2 T}{\partial x^2} + \frac{\partial^2 T}{\partial y^2}\right) \tag{3.73}$$

And the energy equation in the solid is:

$$\frac{\partial e}{\partial t} = \left[\frac{1}{Pe}\right]\left[\frac{\partial}{\partial x}\left(k\frac{\partial T}{\partial x}\right) + \frac{\partial}{\partial y}\left(k\frac{\partial T}{\partial y}\right)\right] \tag{3.74}$$

It should be noted that the Reynolds number is based on the length scale of L = 1mm and not on the characteristic length of the solid, due to the fact that the solid in the problem is changing shape, and therefore it's length scale would change as the simulation evolved in time. The diameters of the SMA wire in the current problem change between 0.5mm and 0.7mm, the choice of a length scale of 1mm was made due to its propinquity to these diameters.

3.5 Transformation to Generalized Coordinates and the Geometric Conservation Law

3.5.1 Transformations and the Jacobian

The partial differential equations derived will be numerically solved on a domain that is discretized into many small finite volume elements. The discretized mesh is a structured boundary fitted mesh such that each element in physical space (x, y) has a corresponding element in computational space (ξ, η). The computational domain is a generalized orthogonal curvilinear coordinate system. The (x, y) coordinates are transformed onto the (ξ, η) coordinates through a simple one to one mapping as illustrated in Figure (3.2) [53] [59].

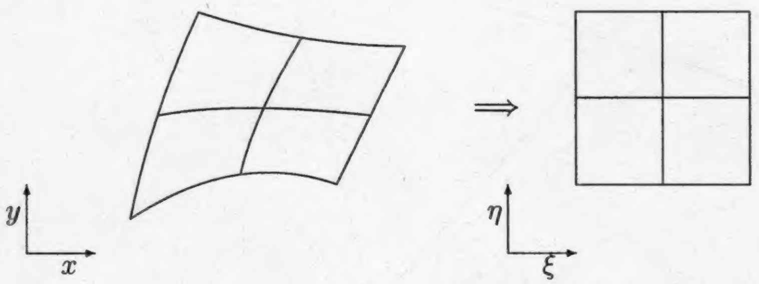

Figure 3.2: Mapping from (x, y) to (ξ, η) Coordinate System

In the current problem, due to the shape change of the solid, the coordinates in physical space (x, y) are not constant. They have time dependence, thus the mapping between the two coordinate systems is constantly changing.

A consequence of this is that we may no longer think of the domain strictly in two dimensions, the two dimensional grid can be thought of as having a third time dimension. A single space-time grid cell is shown in Figure (3.3).

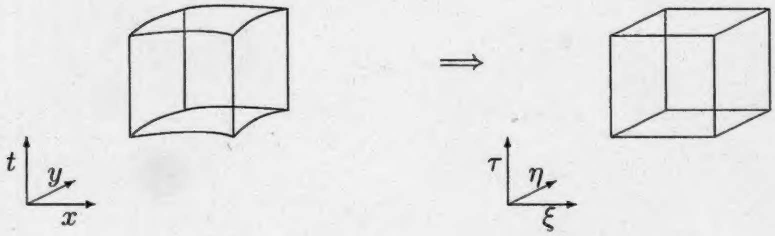

Figure 3.3: Space-Time Grid Cell

The transformed generalized coordinates are now written as:

$$\xi = \xi(x, y, t)\ ;\ \eta = \eta(x, y, t)\ ;\ \tau = \tau(x, y, t) \tag{3.75}$$

And through the one to one mapping the corollary is:

$$x = x(\xi, \eta, \tau)\ ;\ y = y(\xi, \eta, \tau)\ ;\ t = t(\xi, \eta, \tau) \tag{3.76}$$

Where:

$$\Delta\xi = \Delta\eta = \Delta\tau = 1 \tag{3.77}$$

The choice of the change in variables equaling unity is arbitrary. This value could be chosen to be any constant, but unity is the simplest choice. The

Jacobian for this transformation is (note subscripts represent partial derivatives):

$$J = \frac{\partial(x,y,t)}{\partial(\xi,\eta,\tau)} = \begin{bmatrix} x_\xi & x_\eta & x_\tau \\ y_\xi & y_\eta & y_\tau \\ t_\xi & t_\eta & t_\tau \end{bmatrix} \tag{3.78}$$

The inverse of the Jacobian can be computed, through Cramer's rule and simple linear algebra, to be:

$$\begin{aligned} J^{-1} &= \begin{bmatrix} \xi_x & \xi_y & \xi_t \\ \eta_x & \eta_y & \eta_t \\ \tau_x & \tau_y & \tau_t \end{bmatrix} \\ &= \frac{1}{||J||} \begin{bmatrix} (y_\eta t_\tau - y_\tau t_\eta) & (x_\tau t_\eta - x_\eta t_\tau) & (x_\eta y_\tau - x_\tau y_\eta) \\ (y_\tau t_\xi - y_\xi t_\tau) & (x_\xi t_\tau - x_\tau t_\xi) & (x_\tau y_\xi - x_\xi y_\tau) \\ (y_\xi t_\eta - y_\eta t_\xi) & (x_\eta t_\xi - x_\xi t_\eta) & (x_\xi y_\eta - x_\eta y_\xi) \end{bmatrix} \end{aligned} \tag{3.79}$$

Where $||J||$ is the determinant of the Jacobian (J). We will have some restrictions on t that will simplify the transformation. Firstly the timestep size (Δt) in the numerical scheme will be held constant. Secondly t will not be allowed to change with respect to ξ and η, and consequently τ will not change with respect to x and y. This means that the grid points exist at discrete points in time, the time level does not change as you move spatially through the grid. Therefore:

$$\frac{\partial t}{\partial \xi} = 0 \ ; \ \frac{\partial t}{\partial \eta} = 0 \ ; \ \frac{\partial t}{\partial \tau} = \frac{\Delta t}{\Delta \tau} = \Delta t \tag{3.80}$$

Likewise:

$$\frac{\partial \tau}{\partial x} = 0 \ ; \ \frac{\partial \tau}{\partial y} = 0 \ ; \ \frac{\partial \tau}{\partial t} = \frac{\Delta \tau}{\Delta t} = \frac{1}{\Delta t} \tag{3.81}$$

Thus:

$$J = \begin{bmatrix} x_\xi & x_\eta & x_\tau \\ y_\xi & y_\eta & y_\tau \\ 0 & 0 & \Delta t \end{bmatrix} \tag{3.82}$$

$$\begin{aligned} J^{-1} &= \begin{bmatrix} \xi_x & \xi_y & \xi_t \\ \eta_x & \eta_y & \eta_t \\ 0 & 0 & \frac{1}{\Delta t} \end{bmatrix} \\ &= \frac{1}{||J||} \begin{bmatrix} y_\eta \Delta t & -x_\eta \Delta t & (x_\eta y_\tau - x_\tau y_\eta) \\ -y_\xi \Delta t & x_\xi \Delta t & (x_\tau y_\xi - x_\xi y_\tau) \\ 0 & 0 & (x_\xi y_\eta - x_\eta y_\xi) \end{bmatrix} \end{aligned} \tag{3.83}$$

Where:

$$||J|| = \Delta t (x_\xi y_\eta - x_\eta y_\xi) = \Delta t ||J||_{2D} \tag{3.84}$$

Note that $||J||_{2D} = (x_\xi y_\eta - x_\eta y_\xi)$ is known as the two dimensional determinant of the Jacobian. The geometric derivatives (y_η, x_ξ etc.) are often referred to as the geometrics of the transformation [2].

The chain rule must be invoked to expand partial derivatives in x, y, and t to partial derivatives in ξ, η, and τ. All derivatives will be expanded using the following:

$$\frac{\partial}{\partial t} = \frac{\partial}{\partial \tau}\frac{\partial \tau}{\partial t} + \frac{\partial}{\partial \xi}\frac{\partial \xi}{\partial t} + \frac{\partial}{\partial \eta}\frac{\partial \eta}{\partial t} \tag{3.85}$$

$$\frac{\partial}{\partial x} = \frac{\partial}{\partial \xi}\frac{\partial \xi}{\partial x} + \frac{\partial}{\partial \eta}\frac{\partial \eta}{\partial x} \tag{3.86}$$

$$\frac{\partial}{\partial y} = \frac{\partial}{\partial \xi}\frac{\partial \xi}{\partial y} + \frac{\partial}{\partial \eta}\frac{\partial \eta}{\partial y} \tag{3.87}$$

3.5.2 Transformation of Conservation of Mass

Applying Equations (3.86) and (3.87) to the conservation of mass, Equation (3.71), we get (note that subscripts imply partial differentiation):

$$\frac{\partial u}{\partial \xi}\xi_x + \frac{\partial u}{\partial \eta}\eta_x + \frac{\partial v}{\partial \xi}\xi_y + \frac{\partial v}{\partial \eta}\eta_y = 0 \tag{3.88}$$

Multiplying Equation (3.88) by the determinant of the Jacobian, Equation (3.84), and using the relationship between the geometric derivatives shown in Equation (3.83) we get:

$$\frac{\partial u}{\partial \xi}(y_\eta \Delta t) + \frac{\partial u}{\partial \eta}(-y_\xi \Delta t) + \frac{\partial v}{\partial \xi}(-x_\eta \Delta t) + \frac{\partial v}{\partial \eta}(x_\xi \Delta t) = 0 \tag{3.89}$$

Bringing all geometric terms inside the derivatives and moving all non-differentiated terms to the right hand side we get :

$$\begin{aligned} \frac{\partial[u y_\eta \Delta t + v(-x_\eta)\Delta t]}{\partial \xi} &+ \frac{\partial[u(-y_\xi)\Delta t + v x_\xi \Delta t]}{\partial \eta} \\ &= u(y_{\eta\xi} - y_{\xi\eta})\Delta t + v(x_{\xi\eta} - x_{\eta\xi})\Delta t \end{aligned} \tag{3.90}$$

It is obvious from the above equation that the mixed geometric derivative differences on the right hand side are equal to zero ($y_{\eta\xi} - y_{\xi\eta} = 0$ and $x_{\xi\eta} - x_{\eta\xi} = 0$) analytically, due to the commutative property of differentiation, this is sometimes referred to as a geometric conservation law [52] or a geometric condition [62]. Thus the numerical scheme used to construct the spatial geometric derivatives is required to also satisfy the commutative property (i.e. satisfy the geometric conservation law). If not, errors in conservation of mass would develop thus giving spurious results. The use of a finite volume formulation whose geometric terms are defined on the faces of mesh cells enforces the commutative property automatically [62]. This is the type of scheme used in the current work.

By assuming that the geometric conservation law is satisfied and by dividing out the time step (Δt), Equation (3.90) reduces to:

$$\frac{\partial[uy_\eta + v(-x_\eta)]}{\partial\xi} + \frac{\partial[u(-y_\xi) + vx_\xi]}{\partial\eta} = 0 \tag{3.91}$$

3.5.3 Transformation of the Vorticity Transport and Energy Equations

The vorticity transport equation (3.72) and the energy equation in the fluid (3.73) are both viscous scalar transport equations. They both involve hyperbolic convective derivatives and elliptic dissipation derivatives. The transformation of these two similar equations will be demonstrated on the model equation below:

$$\frac{\partial W}{\partial t} + \frac{\partial(uW)}{\partial x} + \frac{\partial(vW)}{\partial y} = \frac{\partial^2 W}{\partial x^2} + \frac{\partial^2 W}{\partial y^2} \tag{3.92}$$

In the above equation W represents the primitive variable (either ω or T in the vorticity transport and energy equations).

Applying Equations (3.85), (3.86) and (3.87) to the model equation (3.92), we get (subscripts imply partial differentiation):

$$\frac{\partial W}{\partial\tau}\tau_t + \frac{\partial W}{\partial\xi}\xi_t + \frac{\partial W}{\partial\eta}\eta_t + \frac{\partial(uW)}{\partial\xi}\xi_x + \frac{\partial(uW)}{\partial\eta}\eta_x$$

$$+\frac{\partial(vW)}{\partial\xi}\xi_y+\frac{\partial(vW)}{\partial\eta}\eta_y=\frac{\partial A}{\partial\xi}\xi_x+\frac{\partial A}{\partial\eta}\eta_x+\frac{\partial B}{\partial\xi}\xi_y+\frac{\partial B}{\partial\eta}\eta_y \tag{3.93}$$

Where:

$$A=\left[\frac{\partial W}{\partial\xi}\xi_x+\frac{\partial W}{\partial\eta}\eta_x\right]\ ;\ B=\left[\frac{\partial W}{\partial\xi}\xi_y+\frac{\partial W}{\partial\eta}\eta_y\right] \tag{3.94}$$

Multiplying Equation (3.93) by the determinant of the Jacobian, Equation (3.84), and using the relationship between the geometric derivatives shown in Equation (3.83) we get:

$$\begin{aligned}\frac{\partial W}{\partial\tau}\frac{\Delta t(x_\xi y_\eta-x_\eta y_\xi)}{\Delta t}&+\frac{\partial W}{\partial\xi}(x_\eta y_\tau-x_\tau y_\eta)+\frac{\partial W}{\partial\eta}(x_\tau y_\xi-x_\xi y_\tau)\\&+\frac{\partial(uW)}{\partial\xi}(y_\eta\Delta t)+\frac{\partial(uW)}{\partial\eta}(-y_\xi\Delta t)+\frac{\partial(vW)}{\partial\xi}(-x_\eta\Delta t)\\&+\frac{\partial(vW)}{\partial\eta}(x_\xi\Delta t)=\frac{\partial A}{\partial\xi}(y_\eta\Delta t)+\frac{\partial A}{\partial\eta}(-y_\xi\Delta t)\\&+\frac{\partial B}{\partial\xi}(-x_\eta\Delta t)+\frac{\partial B}{\partial\eta}(x_\xi\Delta t)\end{aligned} \tag{3.95}$$

Bringing all geometric terms inside the derivatives and moving all non-differentiated terms to the right hand side and lumping them into a variable called GCL we get:

$$\begin{aligned}\frac{\partial[W||J||_{2D}]}{\partial\tau}&+\frac{\partial[W(uy_\eta\Delta t+v(-x_\eta)\Delta t-x_\tau y_\eta-y_\tau(-x_\eta))]}{\partial\xi}\\&+\frac{\partial[W(u(-y_\xi)\Delta t+vx_\xi\Delta t-x_\tau(-y_\xi)-y_\tau x_\xi)]}{\partial\eta}\\&=\frac{\partial(Ay_\eta\Delta t-Bx_\eta\Delta t)}{\partial\xi}+\frac{\partial(Bx_\xi\Delta t-Ay_\xi\Delta t)}{\partial\eta}\\&+GCL\end{aligned} \tag{3.96}$$

Noting that:

$$\begin{aligned}\frac{\partial(Ay_\eta\Delta t - Bx_\eta\Delta t)}{\partial\xi} &= \frac{\partial}{\partial\xi}\left[\left(\frac{y_\eta^2 + x_\eta^2}{||J||_{2D}}\right)\Delta t\frac{\partial W}{\partial\xi}\right.\\ &\left. + \left(\frac{-y_\xi y_\eta - x_\xi x_\eta}{||J||_{2D}}\right)\Delta t\frac{\partial W}{\partial\eta}\right]\end{aligned} \tag{3.97}$$

$$\begin{aligned}\frac{\partial(Bx_\xi\Delta t - Ay_\xi\Delta t)}{\partial\eta} &= \frac{\partial}{\partial\eta}\left[\left(\frac{-y_\xi y_\eta - x_\xi x_\eta}{||J||_{2D}}\right)\Delta t\frac{\partial W}{\partial\xi}\right.\\ &\left. + \left(\frac{y_\xi^2 + x_\xi^2}{||J||_{2D}}\right)\Delta t\frac{\partial W}{\partial\eta}\right]\end{aligned} \tag{3.98}$$

And:

$$\begin{aligned}&GCL = (uW - A)(y_{\eta\xi} - y_{\xi\eta})\Delta t + (vW - B)(x_{\xi\eta} - x_{\eta\xi})\Delta t\\ &+W\left[\frac{\partial||J||_{2D}}{\partial\tau} + \frac{\partial[-x_\tau y_\eta - y_\tau(-x_\eta)]}{\partial\xi} + \frac{\partial[-x_\tau(-y_\xi) - y_\tau x_\xi]}{\partial\eta}\right]\end{aligned} \tag{3.99}$$

This is a more complicated Geometric Conservation Law (GCL) than was found for the conservation of mass equation since it now involves time derivatives. As previously mentioned the numerical scheme must ensure that the commutative property of partial differentiation is upheld. A finite volume formulation whose geometric terms are defined on the faces of mesh cells enforces this spatially. Therefore we can assume that $(y_{\eta\xi} - y_{\xi\eta}) = 0$ and $(x_{\xi\eta} - x_{\eta\xi}) = 0$ through our numerical scheme. Thus we get:

$$GCL = W\left[\frac{\partial||J||_{2D}}{\partial\tau} + \frac{\partial[-x_\tau y_\eta - y_\tau(-x_\eta)]}{\partial\xi} + \frac{\partial[-x_\tau(-y_\xi) - y_\tau x_\xi]}{\partial\eta}\right] \tag{3.100}$$

Expanding out the differentiation we get:

$$\begin{aligned}GCL &= W[x_\tau(y_{\xi\eta} - y_{\eta\xi}) + y_\tau(x_{\eta\xi} - x_{\xi\eta}) + x_\xi(y_{\eta\tau} - y_{\tau\eta}) \\ &+ y_\xi(x_{\tau\eta} - x_{\eta\tau}) + x_\eta(y_{\tau\xi} - y_{\xi\tau}) + y_\eta(x_{\xi\tau} - x_{\tau\xi})]\end{aligned} \tag{3.101}$$

Again we find that the GCL is a series of differences between mixed derivatives and analytically, through the commutative property of partial differentiation, should equal zero exactly. Thus the numerical scheme used to solve the fluid equations must ensure that the following geometric conservation law (in conservation form) is satisfied, in this form it is sometimes referred to as the Jacobian transport equation [49]:

$$\frac{\partial ||J||_{2D}}{\partial \tau} + \frac{\partial[-x_\tau y_\eta - y_\tau(-x_\eta)]}{\partial \xi} + \frac{\partial[-x_\tau(-y_\xi) - y_\tau x_\xi]}{\partial \eta} = 0 \tag{3.102}$$

Or expanded into its spatial and temporal geometrics:

$$\begin{aligned}&x_\tau(y_{\xi\eta} - y_{\eta\xi}) + y_\tau(x_{\eta\xi} - x_{\xi\eta}) + x_\xi(y_{\eta\tau} - y_{\tau\eta}) \\ + \; &y_\xi(x_{\tau\eta} - x_{\eta\tau}) + x_\eta(y_{\tau\xi} - y_{\xi\tau}) + y_\eta(x_{\xi\tau} - x_{\tau\xi}) = 0\end{aligned} \tag{3.103}$$

Equation (3.102) can be interpreted as the rate of change of the volume a grid cell equals the algebraic sum of volumes swept by the boundaries of the control volumes [49], [17], [15]. Thomas and Lombard [52] were the first to cast the GCL in conservation form, Equation (3.102). They found that if the GCL was not satisfied they would get spurious results. They suggested that the GCL in its conservation form should be solved using the same numerical time advancing scheme that the equations of motion are solved with, to ensure its satisfaction. In essence this means that the determinant of the 2D

Jacobian ($||J||_{2D}$), which can be interpreted to be the volume of a grid cell, is not computed from the actual grid locations at a given time step, but from the time advancement of Equation (3.102), as if it is a physical transport equation.

In light of the knowledge that the commutative property of mixed derivatives (i.e $x_{\eta\xi}$ etc.) is upheld through the finite volume formulation spatially, it stands to reason that one should be able to automatically satisfy the GCL through a similar approach on the temporal geometrics (i.e. geometrics involving time differentiation, $x_{\tau\eta}$ etc.). This is done by using a numerical procedure that treats time in a finite volume manner and thus computes grid velocities on the faces of the control volumes in the time direction [49]. This is the type of numerical scheme that is used in the current work.

$\begin{bmatrix} u \\ v \end{bmatrix}$ are the real fluid velocities in the (x, y) directions respectively in the physical domain.

$\begin{bmatrix} U \\ V \end{bmatrix}$ are the transformed contravariant velocities in the (ξ, η) directions on the computational grid. The two sets of velocities are related by the coordinate transformation shown below:

$$\begin{bmatrix} U \\ V \\ \frac{1}{\Delta t} \end{bmatrix} = \frac{\partial(\xi, \eta, \tau)}{\partial(x, y, t)} \begin{bmatrix} u \\ v \\ 1 \end{bmatrix} = J^{-1} \begin{bmatrix} u \\ v \\ 1 \end{bmatrix}$$

$$\begin{bmatrix} U \\ V \\ \frac{1}{\Delta t} \end{bmatrix} = \frac{1}{||J||_{2D}\Delta t} \begin{bmatrix} y_\eta \Delta t & -x_\eta \Delta t & (x_\eta y_\tau - x_\tau y_\eta) \\ -y_\xi \Delta t & x_\xi \Delta t & (x_\tau y_\xi - x_\xi y_\tau) \\ 0 & 0 & ||J||_{2D} \end{bmatrix} \begin{bmatrix} u \\ v \\ 1 \end{bmatrix}$$

Expanding this out we see that :

$$||J||_{2D}\Delta t U = u y_\eta \Delta t + v(-x_\eta)\Delta t - x_\tau y_\eta - y_\tau(-x_\eta) \tag{3.104}$$

$$||J||_{2D}\Delta t V = u(-y_\xi)\Delta t + v x_\xi \Delta t - x_\tau(-y_\xi) - y_\tau x_\xi \tag{3.105}$$

Applying these to our model equation (3.96) we get:

$$\begin{aligned} &\frac{\partial[W||J||_{2D}]}{\partial\tau} + \frac{\partial[W||J||_{2D}\Delta t U]}{\partial\xi} + \frac{\partial[W||J||_{2D}\Delta t V]}{\partial\eta} \\ &= \frac{\partial(A y_\eta \Delta t - B x_\eta \Delta t)}{\partial\xi} + \frac{\partial(B x_\xi \Delta t - A y_\xi \Delta t)}{\partial\eta} \end{aligned} \tag{3.106}$$

If we apply the transformations done to the model equation (3.92) to the vorticity transport equation (3.72) and the energy equation (3.73) we get:

VORTICITY

$$\begin{aligned} \frac{\partial[\omega||J||_{2D}]}{\partial\tau} &+ \frac{\partial[\omega||J||_{2D}\Delta t U]}{\partial\xi} + \frac{\partial[\omega||J||_{2D}\Delta t V]}{\partial\eta} \\ &= \left[\frac{Gr}{Re^2}\right]\left[\frac{\partial[T y_\eta \Delta t]}{\partial\xi} + \frac{\partial[T(-y_\xi)\Delta t]}{\partial\eta}\right] \\ &+ \left[\frac{1}{Re}\right]\left[\frac{\partial(A y_\eta \Delta t - B x_\eta \Delta t)}{\partial\xi} + \frac{\partial(B x_\xi \Delta t - A y_\xi \Delta t)}{\partial\eta}\right] \end{aligned} \tag{3.107}$$

Noting that in the above equation:

$$\begin{aligned} \frac{\partial(A y_\eta \Delta t - B x_\eta \Delta t)}{\partial\xi} &= \frac{\partial}{\partial\xi}\left[\left(\frac{y_\eta^2 + x_\eta^2}{||J||_{2D}}\right)\Delta t\frac{\partial\omega}{\partial\xi}\right. \\ &\left. + \left(\frac{-y_\xi y_\eta - x_\xi x_\eta}{||J||_{2D}}\right)\Delta t\frac{\partial\omega}{\partial\eta}\right] \end{aligned} \tag{3.108}$$

$$\begin{aligned}\frac{\partial(Bx_\xi\Delta t - Ay_\xi\Delta t)}{\partial\eta} &= \frac{\partial}{\partial\eta}\left[\left(\frac{-y_\xi y_\eta - x_\xi x_\eta}{||J||_{2D}}\right)\Delta t\frac{\partial\omega}{\partial\xi}\right. \\ &\quad \left. + \left(\frac{y_\xi^2 + x_\xi^2}{||J||_{2D}}\right)\Delta t\frac{\partial\omega}{\partial\eta}\right] \qquad (3.109)\end{aligned}$$

ENERGY

$$\begin{aligned}&\frac{\partial[T||J||_{2D}]}{\partial\tau} + \frac{\partial[T||J||_{2D}\Delta tU]}{\partial\xi} + \frac{\partial[T||J||_{2D}\Delta tV]}{\partial\eta} \\ &\quad = \left[\frac{1}{RePr}\right]\left[\frac{\partial(Ay_\eta\Delta t - Bx_\eta\Delta t)}{\partial\xi} + \frac{\partial(Bx_\xi\Delta t - Ay_\xi\Delta t)}{\partial\eta}\right] \qquad (3.110)\end{aligned}$$

Noting that in the above equation:

$$\begin{aligned}\frac{\partial(Ay_\eta\Delta t - Bx_\eta\Delta t)}{\partial\xi} &= \frac{\partial}{\partial\xi}\left[\left(\frac{y_\eta^2 + x_\eta^2}{||J||_{2D}}\right)\Delta t\frac{\partial T}{\partial\xi}\right. \\ &\quad \left. + \left(\frac{-y_\xi y_\eta - x_\xi x_\eta}{||J||_{2D}}\right)\Delta t\frac{\partial T}{\partial\eta}\right] \qquad (3.111)\end{aligned}$$

$$\begin{aligned}\frac{\partial(Bx_\xi\Delta t - Ay_\xi\Delta t)}{\partial\eta} &= \frac{\partial}{\partial\eta}\left[\left(\frac{-y_\xi y_\eta - x_\xi x_\eta}{||J||_{2D}}\right)\Delta t\frac{\partial T}{\partial\xi}\right. \\ &\quad \left. + \left(\frac{y_\xi^2 + x_\xi^2}{||J||_{2D}}\right)\Delta t\frac{\partial T}{\partial\eta}\right] \qquad (3.112)\end{aligned}$$

These two equations along with the conservation of mass (3.91) are the three conservation equations solved in computational space.

3.5.4 Transformation of the Energy Equation in the Solid

Applying the transformation to generalized coordinates to the energy equation in the solid (3.74) we get:

SOLID ENERGY

$$\frac{\partial[e||J||_{2D}]}{\partial\tau} + \frac{\partial[e(-x_\tau y_\eta - y_\tau(-x_\eta))]}{\partial\xi} + \frac{\partial[e(-x_\tau(-y_\xi) - y_\tau x_\xi)]}{\partial\eta}$$

$$= \left[\frac{1}{Pe}\right]\left[\frac{\partial(Ay_\eta\Delta t - Bx_\eta\Delta t)}{\partial\xi} + \frac{\partial(Bx_\xi\Delta t - Ay_\xi\Delta t)}{\partial\eta}\right] \qquad (3.113)$$

Noting that in the above equation:

$$\frac{\partial(Ay_\eta\Delta t - Bx_\eta\Delta t)}{\partial\xi} = \frac{\partial}{\partial\xi}\left[k\left(\frac{y_\eta^2 + x_\eta^2}{||J||_{2D}}\right)\Delta t\frac{\partial T}{\partial\xi} + k\left(\frac{-y_\xi y_\eta - x_\xi x_\eta}{||J||_{2D}}\right)\Delta t\frac{\partial T}{\partial\eta}\right] \qquad (3.114)$$

$$\frac{\partial(Bx_\xi\Delta t - Ay_\xi\Delta t)}{\partial\eta} = \frac{\partial}{\partial\eta}\left[k\left(\frac{-y_\xi y_\eta - x_\xi x_\eta}{||J||_{2D}}\right)\Delta t\frac{\partial T}{\partial\xi} + k\left(\frac{y_\xi^2 + x_\xi^2}{||J||_{2D}}\right)\Delta t\frac{\partial T}{\partial\eta}\right] \qquad (3.115)$$

The tranformed energy equation in the solid contains grid velocity terms (x_τ and y_τ). These grid velocities allow the movement of the solid boundary to be felt by the energy equation. It should also be noted here that the geometric conservation law must also be satisfied in the solid to prevent spurious energy source terms. The numerical scheme used to solve this equation will be described in detail in the next chapter.

CHAPTER 4

NUMERICAL FORMULATION

4.1 Solution Sequence

The equations derived in the previous chapter will now be solved numerically using the following sequence of steps for a single timestep.

I: Begin the time stepping by solving the energy equation in the solid (3.113). Time advancement of Equation (3.113) is achieved through a second order accurate single step technique, that is geometrically conservative in time. Jameson's four level multistage scheme is used to iterate the single step formulation to convergence at each time step. This equation requires iteration because the grid at the next timestep is not yet known, the solid grid changes with each iteration until a converged solution is found. The new SMA shape is calculated from the average cross-sectional phase of the solid at the next timestep. Once a converged solution in the solid is found, the grid in the fluid region is then constructed. The spatial derivatives are computed using a linear interpolation of the differentiated variables.

II: The primitive variable in the time derivative of Equation (3.113) is the internal energy (e). So Equation (3.54) must be solved for the temperature.

$$e = c_p T + H\xi(T)$$

This is a highly non-linear equation, due to the complicated mathematical representation of phase, Equation (3.49). It is analytically impossible to solve for temperature (T) as a function of internal energy (e), therefore a Newton root finding method is employed to converge a solution for T corresponding to a given e.

III: The next item in the sequence is to time advance the viscous vorticity transport equation and the energy equation in the fluid, i.e. solving Equations (3.107) and (3.110). Since we know the grid at the next timestep no iteration is required to do the time integration. The time integration of these two equations is accomplished through a two stage, second order accurate, explicit multistage scheme. Linear interpolation is used to construct spatial second derivatives (or viscous derivatives). A Uniformly Non-oscillatory, 2nd order (UNO2) accurate interpolation will be used to construct the spatial first derivatives (or convective derivatives).

IV: Due to the velocity decomposition shown in Equations (3.33) and (3.34), the viscous stream function (ψ) is required to calculate the velocity field at the next timestep. The relationship between the viscous stream function and the vorticity is the following:

$$\frac{\partial^2 \psi}{\partial x^2} + \frac{\partial^2 \psi}{\partial y^2} = \omega \tag{4.1}$$

Equation (4.1) represents the viscous correction to the inviscid potential flow that would exist without vorticity. This elliptic equation will be solved using an approximate LU factorization scheme. The convergence to steady state is accelerated by the application of a multigrid procedure.

V: The final item in the sequence is that the conservation of mass equation (3.91) must be satisfied. This is done by applying the velocity decomposition, Equations (3.33) and (3.34), to the conservation of mass equation. This results in the following elliptic equation (shown in Cartesian coordinates for brevity):

$$\frac{\partial^2 \phi}{\partial x^2} + \frac{\partial^2 \phi}{\partial y^2} = \frac{\partial^2 \psi}{\partial y \partial x} - \frac{\partial^2 \psi}{\partial x \partial y} \tag{4.2}$$

So to satisfy continuity only the above equation needs to be solved for ϕ. Equation (4.2) is solved using an approximate LU factorization scheme. Once again the convergence to steady state is accelerated by the application of a multigrid procedure. This is the same technique used to solve the viscous correction equation (4.1), except that there is a different source term on the right hand side of Equation (4.2).

This sequence of steps must be completed for each time increment to maintain a time accurate solution of the primitive variables.

4.2 Solution of the Energy Equation in the Solid

4.2.1 Discretization of Energy Equation

Recall that the transformed energy equation in the solid is:

$$\begin{aligned}&\frac{\partial[e||J||_{2D}]}{\partial\tau} + \frac{\partial[e(-x_\tau y_\eta - y_\tau(-x_\eta))]}{\partial\xi} + \frac{\partial[e(-x_\tau(-y_\xi) - y_\tau x_\xi)]}{\partial\eta} \\ &= \left[\frac{1}{Pe}\right]\left[\frac{\partial(Ay_\eta\Delta t - Bx_\eta\Delta t)}{\partial\xi} + \frac{\partial(Bx_\xi\Delta t - Ay_\xi\Delta t)}{\partial\eta}\right]\end{aligned} \tag{4.3}$$

Noting that in the above equation:

$$\begin{aligned}\frac{\partial(Ay_\eta\Delta t - Bx_\eta\Delta t)}{\partial\xi} &= \frac{\partial}{\partial\xi}\left[k\left(\frac{y_\eta^2 + x_\eta^2}{||J||_{2D}}\right)\Delta t\frac{\partial T}{\partial\xi}\right. \\ &\quad \left. + k\left(\frac{-y_\xi y_\eta - x_\xi x_\eta}{||J||_{2D}}\right)\Delta t\frac{\partial T}{\partial\eta}\right]\end{aligned} \tag{4.4}$$

$$\begin{aligned}\frac{\partial(Bx_\xi\Delta t - Ay_\xi\Delta t)}{\partial\eta} &= \frac{\partial}{\partial\eta}\left[k\left(\frac{-y_\xi y_\eta - x_\xi x_\eta}{||J||_{2D}}\right)\Delta t\frac{\partial T}{\partial\xi}\right. \\ &\quad \left. + k\left(\frac{y_\xi^2 + x_\xi^2}{||J||_{2D}}\right)\Delta t\frac{\partial T}{\partial\eta}\right]\end{aligned} \tag{4.5}$$

Writing equation (4.3) in the form:

$$\begin{aligned}\frac{\partial e||J||_{2D}}{\partial\tau} &= -\frac{\partial G}{\partial\xi} - \frac{\partial H}{\partial\eta} + \frac{\partial I}{\partial\xi} + \frac{\partial K}{\partial\eta} \\ \frac{\partial e||J||_{2D}}{\partial\tau} &= \mathrm{Res}(e, T, ||J||_{2D})\end{aligned} \tag{4.6}$$

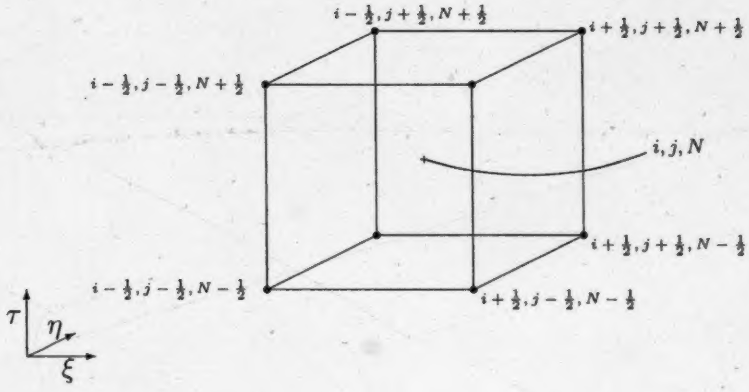
$i-\frac{1}{2}, j+\frac{1}{2}, N+\frac{1}{2}$
$i+\frac{1}{2}, j+\frac{1}{2}, N+\frac{1}{2}$
$i-\frac{1}{2}, j-\frac{1}{2}, N+\frac{1}{2}$
i, j, N
$i+\frac{1}{2}, j+\frac{1}{2}, N-\frac{1}{2}$
$i-\frac{1}{2}, j-\frac{1}{2}, N-\frac{1}{2}$
$i+\frac{1}{2}, j-\frac{1}{2}, N-\frac{1}{2}$
T
η
ξ

Figure 4.1: Computational Finite Volume Grid Cell

Where the right hand side is called the residual or Res, and is a function of the internal energy (e), temperature (T), and the grid geometry through the transformation geometrics and the determinant of the Jacobian ($||J||$). Also:

$$G = e[-x_\tau(y_\eta) - y_\tau(-x_\eta)] = e[-||J||_{2D}\Delta t U_{grid}] \tag{4.7}$$

Where U_{grid} refers to the x contravariant grid velocity.

$$H = e[-x_\tau(-y_\xi) - y_\tau(x_\xi)] = e[-||J||_{2D}\Delta t V_{grid}] \tag{4.8}$$

Where V_{grid} refers to the y contravariant grid velocity.

$$I = (Ay_\eta \Delta t - Bx_\eta \Delta t) \tag{4.9}$$

$$K = (Bx_\xi \Delta t - Ay_\xi \Delta t) \tag{4.10}$$

Figure (4.1) illustrates a single finite volume grid cell in computational space. The variables e, T, k, and $||J||_{2D}$ in Equation (4.3) exist in the centre of the control volume (at the i, j, N position). Conversely the x, y grid points themselves are defined in space at the corners of the control volume at a given timestep (i.e. at the $i-\frac{1}{2}, j-\frac{1}{2}, N$ etc. positions). To compute the x, y grid locations at the corners of the space-time grid cell (i.e. at the $i-\frac{1}{2}, j-\frac{1}{2}, N+\frac{1}{2}$ etc. positions) one simply averages the x, y values between the respective time levels. For example, average $N+1$ and N to get $N+\frac{1}{2}$.

Since the geometry of the grid at the new time level (N+1) is determined by the thermal state of the solid through the average phase at that time level, an iterative approach to the solution of Eqn. (4.6) must be taken. To achieve second order accuracy in time we discretize Eqn.(4.6) in a single step technique shown below:

$$\frac{e^{N+1}||J||_{2D}^{N+1} - e^{N}||J||_{2D}^{N}}{\Delta\tau} = \text{Res}(e, T, ||J||)^{N+\frac{1}{2}} \tag{4.11}$$

The control volume discretization of the Residual must be done as below to maintain second order accuracy of both time and space while automatically satisfying the geometric conservation law (GCL) described in section(3.5.3):

$$\begin{aligned}\text{Res}(e, T, ||J||_{2D})_{ij}^{N+\frac{1}{2}} &= -\frac{G_{i+\frac{1}{2}j}^{N+\frac{1}{2}} - G_{i-\frac{1}{2}j}^{N+\frac{1}{2}}}{\Delta\xi} - \frac{H_{ij+\frac{1}{2}}^{N+\frac{1}{2}} - H_{ij-\frac{1}{2}}^{N+\frac{1}{2}}}{\Delta\eta} \\ &+ \frac{I_{i+\frac{1}{2}j}^{N+\frac{1}{2}} - I_{i-\frac{1}{2}j}^{N+\frac{1}{2}}}{\Delta\xi} + \frac{K_{ij+\frac{1}{2}}^{N+\frac{1}{2}} - K_{ij-\frac{1}{2}}^{N+\frac{1}{2}}}{\Delta\eta}\end{aligned} \tag{4.12}$$

The first two terms in Equation (4.12) contain the grid geometrics. An example of these two terms is defined below:

$$G_{i-\frac{1}{2}j}^{N+\frac{1}{2}} = e_{i-\frac{1}{2}j}^{N+\frac{1}{2}}[-||J||_{2D}\Delta t U_{grid}]_{i-\frac{1}{2}j}^{N+\frac{1}{2}} \tag{4.13}$$

$$H_{ij-\frac{1}{2}}^{N+\frac{1}{2}} = e_{ij-\frac{1}{2}}^{N+\frac{1}{2}}[-||J||_{2D}\Delta t V_{grid}]_{ij-\frac{1}{2}}^{N+\frac{1}{2}} \tag{4.14}$$

Where:

$$e_{i-\frac{1}{2}j}^{N+\frac{1}{2}} = \frac{1}{2}(e_{i-\frac{1}{2}j}^{N+1} + e_{i-\frac{1}{2}j}^{N}) \tag{4.15}$$

As discussed earlier in section (3.5.3), the construction of the contravariant grid velocities must be done such that it ensures geometric conservation. This is done spatially by defining the grid geometrics on the faces of the control volume at time level N (see figure 4.1), i.e. on the $i+\frac{1}{2}, j, N$ etc. grid faces [62]. The temporal geometrics are calculated using simple backward euler differencing between $N+1$ and N, thus defining them on the $N+\frac{1}{2}$ faces of the space-time control volume in Figure (4.1). The spatial geometrics inside the contravariant grid velocities (Equations 4.7 and 4.8) must be averaged to this same $N+\frac{1}{2}$ face [49]. This is shown mathematically below:

$$\begin{aligned} -\|J\|_{2D}\Delta t U_{grid}^{N+\frac{1}{2}} &= -x_\tau^{N+\frac{1}{2}}\frac{(y_\eta^N + y_\eta^{N+1})}{2} - y_\tau^{N+\frac{1}{2}}\frac{(-x_\eta^N - x_\eta^{N+1})}{2} \\ &= -x_\tau^{N+\frac{1}{2}}(y_\eta^{N+\frac{1}{2}}) - y_\tau^{N+\frac{1}{2}}(-x_\eta^{N+\frac{1}{2}}) \end{aligned} \tag{4.16}$$

$$\begin{aligned} -\|J\|_{2D}\Delta t V_{grid}^{N+\frac{1}{2}} &= -x_\tau^{N+\frac{1}{2}}\frac{(-y_\xi^N - y_\xi^{N+1})}{2} - y_\tau^{N+\frac{1}{2}}\frac{(x_\xi^N + x_\xi^{N+1})}{2} \\ &= -x_\tau^{N+\frac{1}{2}}(-y_\xi^{N+\frac{1}{2}}) - y_\tau^{N+\frac{1}{2}}(x_\xi^{N+\frac{1}{2}}) \end{aligned} \tag{4.17}$$

Where:

$$x_\tau^{N+\frac{1}{2}} = \frac{x^{N+1} - x^N}{\Delta\tau} \; ; \; y_\tau^{N+\frac{1}{2}} = \frac{y^{N+1} - y^N}{\Delta\tau} \tag{4.18}$$

And the spatial geometrics are computed like the examples below:

$$\begin{aligned} x_\xi\big|_{ij-\frac{1}{2}}^{N} &= \frac{x_{i+\frac{1}{2}j-\frac{1}{2}}^N - x_{i-\frac{1}{2}j-\frac{1}{2}}^N}{\Delta\xi} \; ; \; x_\eta\big|_{i-\frac{1}{2}j}^{N} = \frac{x_{i-\frac{1}{2}j+\frac{1}{2}}^N - x_{i-\frac{1}{2}j-\frac{1}{2}}^N}{\Delta\eta} \\ y_\xi\big|_{ij-\frac{1}{2}}^{N} &= \frac{y_{i+\frac{1}{2}j-\frac{1}{2}}^N - y_{i-\frac{1}{2}j-\frac{1}{2}}^N}{\Delta\xi} \; ; \; y_\eta\big|_{i-\frac{1}{2}j}^{N} = \frac{y_{i-\frac{1}{2}j+\frac{1}{2}}^N - y_{i-\frac{1}{2}j-\frac{1}{2}}^N}{\Delta\eta} \end{aligned} \tag{4.19}$$

The treatment of the temporal geometrics in the above fashion guarantees automatic satisfaction of the geometric conservation law. This scheme avoids using the so called Jacobian transport equation (3.103) to update $||J||_{2D}$ in time. This is numerically more efficient, simpler, and is a far more logical method than treating Equation (3.103) as a physical transport equation.

The I and K terms in Eqn.(4.12) are computed by averaging their evaluations at their respective time levels. Examples are shown below:

$$I^{N+\frac{1}{2}}_{i-\frac{1}{2}j} = \frac{1}{2}\left[(Ay_\eta \Delta t - Bx_\eta \Delta t)^{N+1}_{i-\frac{1}{2}j} + (Ay_\eta \Delta t - Bx_\eta \Delta t)^{N}_{i-\frac{1}{2}j}\right] \tag{4.20}$$

Where:

$$\begin{aligned}(Ay_\eta \Delta t - Bx_\eta \Delta t)^{N}_{i-\frac{1}{2}j} &= \left[k\frac{\partial T}{\partial \xi}\left(\frac{y_\eta^2 + x_\eta^2}{x_\xi y_\eta - x_\eta y_\xi}\right)\Delta t \right.\\ &\quad \left. + k\frac{\partial T}{\partial \eta}\left(\frac{-x_\xi x_\eta - y_\xi y_\eta}{x_\xi y_\eta - x_\eta y_\xi}\right)\Delta t\right]^{N}_{i-\frac{1}{2}j}\end{aligned}$$

$$k^N_{i-\frac{1}{2}j} = \left(\frac{k^N_{i-1j} + k^N_{ij}}{2}\right)$$

$$\left(\frac{\partial T}{\partial \xi}\right)^N_{i-\frac{1}{2}j} = \frac{T^N_{ij} - T^N_{i-1j}}{\Delta \xi}$$

$$\left(\frac{\partial T}{\partial \eta}\right)^N_{i-\frac{1}{2}j} = \left[\frac{\left(\frac{T^N_{i-1j+1} - T^N_{i-1j-1}}{2\Delta \eta}\right) + \left(\frac{T^N_{ij+1} - T^N_{ij-1}}{2\Delta \eta}\right)}{2}\right]$$

Etc. and:

$$K^{N+\frac{1}{2}}_{ij-\frac{1}{2}} = \frac{1}{2}\left[(Bx_\xi \Delta t - Ay_\xi \Delta t)^{N+1}_{ij-\frac{1}{2}} + (Bx_\xi \Delta t - Ay_\xi \Delta t)^{N}_{ij-\frac{1}{2}}\right] \tag{4.21}$$

Where:

$$
\begin{aligned}
(Bx_\xi \Delta t - Ay_\xi \Delta t)^N_{ij-\frac{1}{2}} &= \left[k\frac{\partial T}{\partial \eta}\left(\frac{y_\xi^2 + x_\xi^2}{x_\xi y_\eta - x_\eta y_\xi}\right)\Delta t \right. \\
&\quad \left. + k\frac{\partial T}{\partial \xi}\left(\frac{-x_\xi x_\eta - y_\xi y_\eta}{x_\xi y_\eta - x_\eta y_\xi}\right)\Delta t\right]^N_{ij-\frac{1}{2}}
\end{aligned}
$$

$$k^N_{ij-\frac{1}{2}} = \left(\frac{k^N_{ij-1} + k^N_{ij}}{2}\right)$$

$$\left(\frac{\partial T}{\partial \eta}\right)^N_{ij-\frac{1}{2}} = \left(\frac{T^N_{ij} - T^N_{ij-1}}{\Delta \eta}\right)$$

$$\left(\frac{\partial T}{\partial \xi}\right)^N_{ij-\frac{1}{2}} = \left[\frac{\left(\frac{T^N_{i+1j-1} - T^N_{i-1j-1}}{2\Delta \xi}\right) + \left(\frac{T^N_{i+1j} - T^N_{i-1j}}{2\Delta \xi}\right)}{2}\right]$$

4.2.2 Iterative Time Integration Scheme of the Energy Equation in the Solid

Recall Eqn. (4.11):

$$\frac{e^{N+1}||J||^{N+1}_{2D} - e^N||J||^N_{2D}}{\Delta \tau} = \mathrm{Res}(e, T, ||J||_{2D})^{N+\frac{1}{2}}$$

The (N+1) time level solutions to both energy (e) and the Jacobian ($||J||$) are unknown and cannot be explicitly solved for with this discretization. Therefore an iterative procedure must be applied to this algebraic equation. To construct this scheme all of the terms on the left hand side must be moved to the right:

$$0 = -e^{N+1}||J||^{N+1}_{2D} + e^N||J||^N_{2D} + \mathrm{Res}(e, T, ||J||_{2D})^{N+\frac{1}{2}} \tag{4.22}$$

It should be noted that $\Delta\tau = 1$. The variables e, T, and $||J||_{2D}$ at time level (N+1) are now written as the iteration variables $\tilde{e}$, $\tilde{T}$, and $||\tilde{J}||_{2D}$. The expression is then set equal to the derivative of $\tilde{e}||\tilde{J}||_{2D}$ with respect to a pseudo-time variable t^*:

$$\frac{\partial \tilde{e}||\tilde{J}||_{2D}}{\partial t^*} = -\tilde{e}||\tilde{J}||_{2D} + e^N||J||_{2D}^N + \text{Res}(e, T, ||J||_{2D})^{N+\frac{1}{2}} \tag{4.23}$$

The terms on the right hand side of equation (4.23) are known as the residual of the iterative scheme (Res_2). The goal of the iteration process is to drive this residual to zero. When this residual is zero, the energy equation is solved and the iteration variables are exactly the (N+1) solution.

$$\frac{\partial \tilde{e}||\tilde{J}||_{2D}}{\partial t^*} = \text{Res}_2 \tag{4.24}$$

Jameson's four level multistage scheme is used to drive the residual to zero. One cycle of the scheme is shown below (note that m is the pseudo-time level):

$$\begin{aligned}
\tilde{e}^{(1)}||\tilde{J}||_{2D}^{(1)} &= \tilde{e}^{(m)}||\tilde{J}||_{2D}^{(m)} + \alpha_1 \Delta t^* \text{Res}_2^{(m)} \\
\tilde{e}^{(2)}||\tilde{J}||_{2D}^{(2)} &= \tilde{e}^{(1)}||\tilde{J}||_{2D}^{(1)} + \alpha_2 \Delta t^* \text{Res}_2^{(1)} \\
\tilde{e}^{(3)}||\tilde{J}||_{2D}^{(3)} &= \tilde{e}^{(2)}||\tilde{J}||_{2D}^{(2)} + \alpha_3 \Delta t^* \text{Res}_2^{(2)} \\
\tilde{e}^{(m+1)}||\tilde{J}||_{2D}^{(m+1)} &= \tilde{e}^{(3)}||\tilde{J}||_{2D}^{(3)} + \alpha_4 \Delta t^* \text{Res}_2^{(3)}
\end{aligned} \tag{4.25}$$

This cycle is repeated until $\text{Res}_2 < 10^{-10}$, where the iteration process is considered converged. At this point the iteration variables are taken to be the $N+1$ solution, thus completing one time step.

This iteration scheme is similar to a four stage Runge-Kutta scheme except for a few modifications that accelerate convergence. The α stage coefficients need not maintain time accuracy since this is a pseudo-time integration to steady state. Both the stage coefficients and the pseudo-time step size can be chosen such that they accelerate convergence. The parameters used in the current work are $\alpha_1 = 0.25, \alpha_2 = 0.5, \alpha_3 = 0.75, \alpha_4 = 1$, and $\Delta t^* = 0.1$.

4.2.3 Newton Iteration Solution of Temperature

In the solid the primitive variable that is updated in time is the internal energy (e), as shown in Equation (4.3). However, temperature (T) is also required to calculate the residual in Equation (4.11). The specific internal energy is a function of temperature as follows:

$$e(T) = c_p T + H\xi(T) \tag{4.26}$$

Where $\xi(T)$ is defined by Equations (3.49) and (3.50). Equation (4.26) is highly nonlinear due to the mathematical representation of phase. It is therefore impossible to analytically solve for temperature (T) as a function of internal energy (e). A Newton rootfinding method is employed to calculate a temperature from a given internal energy.

The Newton iteration is written as:

$$T^{[m+1]} = T^{[m]} - \frac{e(T^{[m]}) - e^{[m]}}{e'(T^{[m]})} \tag{4.27}$$

Where the superscript $[m]$ is an iteration counter local to the Newton root finding scheme. The $e(T)$ term in Equation (4.27) refers to the function in Equation (4.26), the e term refers to the calculated internal energy from the multistage scheme, and the $e'(T)$ term represents the derivative of the function in Equation (4.26) with respect to temperature (T). The derivative is expanded out below:

$$e'(T) = \frac{\partial e}{\partial T} = \frac{\partial}{\partial T}[c_p T + H\xi(T)] = c_p + H\frac{\partial \xi(T^{[m]})}{\partial T} \tag{4.28}$$

Substituting Equations (4.26) and (4.28) into the Newton iteration (Equation 4.27) results in the following:

$$T^{[m+1]} = T^{[m]} - \frac{(c_p T^{[m]} + H\xi(T^{[m]}) - e^{[m]})}{\left(c_p + H\frac{\partial \xi(T^{[m]})}{\partial T}\right)} \tag{4.29}$$

The above equation is used to calculate $T^{[m+1]}$ iteratively until the difference between two successive solutions is below a tolerance level of 10^{-12}:

$$|T^{[m+1]} - T^{[m]}| < \text{Tolerance} = 10^{-12} \tag{4.30}$$

This Newton iteration must be converged for each grid cell in the solid, at each timestep and within all of the multistage levels of the energy equation solution sequence.

4.3 Solution of the Vorticity and Energy Transport Equations in the Fluid

4.3.1 Discretization of the Model Equation

Recall the transformed model equation used to describe the transport equations in the fluid:

$$\begin{aligned} &\frac{\partial [W||J||_{2D}]}{\partial \tau} + \frac{\partial [W||J||_{2D}\Delta t U]}{\partial \xi} + \frac{\partial [W||J||_{2D}\Delta t V]}{\partial \eta} \\ &= \frac{\partial (Ay_\eta \Delta t - Bx_\eta \Delta t)}{\partial \xi} + \frac{\partial (Bx_\xi \Delta t - Ay_\xi \Delta t)}{\partial \eta} \end{aligned} \tag{4.31}$$

Where:

$$\begin{aligned}\frac{\partial(Ay_\eta\Delta t - Bx_\eta\Delta t)}{\partial\xi} &= \frac{\partial}{\partial\xi}\left[\left(\frac{y_\eta^2 + x_\eta^2}{||J||_{2D}}\right)\Delta t\frac{\partial W}{\partial\xi}\right. \\ &\left. + \left(\frac{-y_\xi y_\eta - x_\xi x_\eta}{||J||_{2D}}\right)\Delta t\frac{\partial W}{\partial\eta}\right] \end{aligned} \tag{4.32}$$

$$\begin{aligned}\frac{\partial(Bx_\xi\Delta t - Ay_\xi\Delta t)}{\partial\eta} &= \frac{\partial}{\partial\eta}\left[\left(\frac{-y_\xi y_\eta - x_\xi x_\eta}{||J||_{2D}}\right)\Delta t\frac{\partial W}{\partial\xi}\right. \\ &\left. + \left(\frac{y_\xi^2 + x_\xi^2}{||J||_{2D}}\right)\Delta t\frac{\partial W}{\partial\eta}\right] \end{aligned} \tag{4.33}$$

A description of the numerical procedures used to solve the vorticity and energy equations in the fluid will be done on the above equation for brevity. With W representing vorticity and temperature. We can write the above equation in the form:

$$\frac{\partial[W||J||_{2D}]}{\partial\tau} = -\frac{\partial G}{\partial\xi} - \frac{\partial H}{\partial\eta} + \frac{\partial I}{\partial\xi} + \frac{\partial K}{\partial\eta} \tag{4.34}$$

Where:

$$\begin{aligned} G &= W[u(y_\eta\Delta t) + v(-x_\eta\Delta t) - x_\tau(y_\eta) - y_\tau(-x_\eta)] \\ &= W||J||_{2D}\Delta tU \end{aligned} \tag{4.35}$$

$$\begin{aligned} H &= W[u(-y_\xi\Delta t) + v(x_\xi\Delta t) - x_\tau(-y_\xi) - y_\tau(x_\xi)] \\ &= W||J||_{2D}\Delta tV \end{aligned} \tag{4.36}$$

$$I = (Ay_\eta\Delta t - Bx_\eta\Delta t) \tag{4.37}$$

$$K = (Bx_\xi \Delta t - Ay_\xi \Delta t) \tag{4.38}$$

And U and V are the ξ and η contravariant velocities respectively. The right hand side of Equation (4.34) is known as the residual (Res) of the scheme. The finite volume approximation will be constructed by differencing the G, H, I, and K flux terms on the cell half faces. See Figure (4.1) for the location of terms on the finite volume grid cell.

$$\begin{aligned}\frac{\partial[W||J||_{2D}]}{\partial\tau}\bigg|_{ij}^{N} &= \mathrm{Res}(W_{ij}^N, ||J||_{2Dij}^N) \\ &= -\frac{G_{i+\frac{1}{2}j}^N - G_{i-\frac{1}{2}j}^N}{\Delta\xi} - \frac{H_{ij+\frac{1}{2}}^N - H_{ij-\frac{1}{2}}^N}{\Delta\eta} \\ &\quad + \frac{I_{i+\frac{1}{2}j}^N - I_{i-\frac{1}{2}j}^N}{\Delta\xi} + \frac{K_{ij+\frac{1}{2}}^N - K_{ij-\frac{1}{2}}^N}{\Delta\eta} \end{aligned} \tag{4.39}$$

Two main differences are evident between the energy equation in the solid and the transport equations in the fluid. The first is that the grid geometry at the next timestep $(N+1)$ has already been calculated, therefore an iterative time integration is not required. An explicit time advancement scheme will be employed. The second difference is that the energy equation in the solid was parabolic, meaning that information transmits equally in all directions. The transport equations in the fluid have hyperbolic convection terms, meaning that they transmit information in the direction of wave propagation, as well as some elliptic diffusion terms that transmit information evenly in all directions. The G and H terms are the convective hyperbolic part and will be constructed using a Uniformly Non-oscillatory Second Order (UNO2) upwinding interpolation to the half faces. The I and K terms are the elliptic diffusive part and will be constructed using linear interpolation to the half faces, similar to the construction in the solid.

4.3.2 Construction of the Convective Terms

As previously stated, the convection terms in the model equation are hyperbolic in form. Hyperbolic equations do not have smooth solutions, and information is not transferred equally in all directions. There is a convection velocity which governs the direction in which information travels. As a result linear interpolation is not acceptable for interpolation of the independent variables to the cell faces for convection terms.

The convection velocities are merely the contravariant velocities shown in Equations (4.35) and (4.36). The u and v velocities are simply constructed at the cell faces from the velocity decomposition, Equations (3.33) and (3.34), at time level N. The temporal geometrics (or grid velocities) must be constructed such that they automatically satisfy the geometric conservation law, exactly in the same manner as with the energy equation in the solid. The temporal geometrics will always be defined on the face of the control volume in the time direction shown in Figure (4.1). See Equations (4.18) and (4.19) for the mathematical construction of these terms. Now that the convection velocities are defined at the half cells the interpolation technique can now be described.

The interpolation technique used for the convection term is a nonoscillatory quadratic interpolation scheme known as the Uniformly Nonoscillatory Second Order Accurate upwinding method (UNO2). This method was developed by Harten and Osher [21]. The explanation here is the one given by

Yokota [63], [65].

For simplicity the method will be described using a one dimensional model wave equation that represents the hyperbolic part of the transport equations in the fluid.

$$\frac{\partial W}{\partial t} + c\frac{\partial W}{\partial x} = 0 \tag{4.40}$$

Where W represents the independent variable that is being transported, and c represents the wave speed or convection velocity of the transport equation. Note that c is assumed positive for the following definitions. The spatial descretization is:

$$\frac{\partial W}{\partial t} + c\frac{W_{i+\frac{1}{2}} - W_{i-\frac{1}{2}}}{\Delta x} = 0 \tag{4.41}$$

Interpolations of the independent variable is completed in the following manner, with S_i^x representing the slope of W in the x direction.

$$W_{i+\frac{1}{2}} = W_i + S_i^x\frac{\Delta x}{2} \tag{4.42}$$

The UNO2 scheme uses the following selection process to determine the value of the slope.

$$S_i^x = \frac{\text{median}(0, W_{i+\frac{1}{2}}^c - W_i, W_i - W_{i-\frac{1}{2}}^c)}{\frac{\Delta x}{2}} \tag{4.43}$$

where the median of three numbers can be mathematically defined as:

$$\text{median}(x, y, z) = x + \text{minmod}(y - x, z - x) \tag{4.44}$$

The $W_{i+\frac{1}{2}}^c$ values in Equation (4.43), are constructed using a quadratic interpolation:

$$W_{i+\frac{1}{2}}^c = \frac{1}{2}(W_i + W_{i+1}) - \frac{1}{4}D_{i+\frac{1}{2}} \tag{4.45}$$

where:

$$D_{i+\frac{1}{2}} = \text{minmod}(W_{i+1} - 2W_i + W_{i-1}, W_{i+2} - 2W_{i+1} + W_i) \tag{4.46}$$

and minmod is defined mathematically as:

$$\text{minmod}(a, b) = \text{sign}(a)\text{max}(0, \text{sign}(ab)\text{min}(|a|, |b|)) \tag{4.47}$$

The $D_{i+\frac{1}{2}}$ term represents the extension of the $W^c_{i+\frac{1}{2}}$ term from a linear interpolation in van Leer's *Minmod* [55] to the quadratic interpolation in UNO2.

It should again be noted that the above is a definition of the interpolation procedure for positive wave speeds (c). The interpolations corresponding to negative wave speeds would be done in the following manner:

$$W_{i+\frac{1}{2}} = W_{i+1} - S^x_{i+1}\frac{\Delta x}{2} \tag{4.48}$$

with slopes (S_{i+1} etc.) being constructed in exactly the same manner as Equation (4.43).

The face centered values, $W_{i+\frac{1}{2}}$, must be constructed for the convection term at each stage of the multistage time integration scheme described in section (4.3.4).

4.3.3 Construction of the Diffusive Terms

The diffusive or elliptic spatial derivatives are the I and K terms in Equation (4.34). They represent the viscous part of the vorticity equation and the conduction part of the energy equation. Since they are elliptic in nature, information travels in all directions evenly. Therefore a simple linear averaging to the half cell faces is sufficient to construct the flux quantities $I_{i+\frac{1}{2}j}, K_{ij+\frac{1}{2}}$ etc. An example of these terms is given below:

$$I^N_{i-\frac{1}{2}j} = (Ay_\eta \Delta t - Bx_\eta \Delta t)^N_{i-\frac{1}{2}j} \tag{4.49}$$

Where:

$$\begin{aligned}(Ay_\eta \Delta t - Bx_\eta \Delta t)^N_{i-\frac{1}{2}j} &= \left[\frac{\partial W}{\partial \xi} \left(\frac{y_\eta^2 + x_\eta^2}{||J||_{2D}} \right) \Delta t \right. \\ &\qquad \left. + \frac{\partial W}{\partial \eta} \left(\frac{-x_\xi x_\eta - y_\xi y_\eta}{||J||_{2D}} \right) \Delta t \right]^N_{i-\frac{1}{2}j}\end{aligned}$$

$$\left(\frac{\partial W}{\partial \xi} \right)^N_{i-\frac{1}{2}j} = \frac{W^N_{ij} - W^N_{i-1j}}{\Delta \xi}$$

$$\left(\frac{\partial W}{\partial \eta} \right)^N_{i-\frac{1}{2}j} = \left[\frac{\left(\frac{W^N_{i-1j+1} - W^N_{i-1j-1}}{2\Delta \eta} \right) + \left(\frac{W^N_{ij+1} - W^N_{ij-1}}{2\Delta \eta} \right)}{2} \right]$$

Etc. and:

$$K^N_{ij-\frac{1}{2}} = (Bx_\xi \Delta t - Ay_\xi \Delta t)^N_{ij-\frac{1}{2}} \tag{4.50}$$

Where:

$$\begin{aligned}(Bx_\xi \Delta t - Ay_\xi \Delta t)^N_{ij-\frac{1}{2}} &= \left[\frac{\partial W}{\partial \eta} \left(\frac{y_\xi^2 + x_\xi^2}{||J||_{2D}} \right) \Delta t \right. \\ &\qquad \left. + \frac{\partial W}{\partial \xi} \left(\frac{-x_\xi x_\eta - y_\xi y_\eta}{||J||_{2D}} \right) \Delta t \right]^N_{ij-\frac{1}{2}}\end{aligned}$$

$$\left(\frac{\partial W}{\partial \eta} \right)^N_{ij-\frac{1}{2}} = \left(\frac{W^N_{ij} - W^N_{ij-1}}{\Delta \eta} \right)$$

$$\left(\frac{\partial W}{\partial \xi}\right)^N_{ij-\frac{1}{2}} = \left[\frac{\left(\frac{W^N_{i+1j-1} - W^N_{i-1j-1}}{2\Delta\xi}\right) + \left(\frac{W^N_{i+1j} - W^N_{i-1j}}{2\Delta\xi}\right)}{2}\right]$$

These constructions must be made for each stage of the multistage time integration described in the next section.

4.3.4 Second Order Accurate Multistage Time Integration of the Transport Equations

The numerical technique used to approximate the time derivative in the fluid region is a 2nd order time accurate Explicit Multistage scheme. Recall Equation (4.39):

$$\frac{\partial [W||J||_{2D}]}{\partial \tau}\bigg|^N_{ij} = \mathrm{Res}(W^N_{ij}, ||J||^N_{2Dij})$$

One complete timestep for this technique is shown below:

$$\begin{aligned}
W^{(0)} &= W^{[N]} \qquad (4.51)\\
W^{(1)}||J||^{N+1}_{2D} &= W^{(0)}||J||^N_{2D} + \alpha_1 \Delta t\, \mathrm{Res}(W^{(0)}, ||J||^N_{2D})\\
W^{(2)}||J||^{N+1}_{2D} &= W^{(0)}||J||^N_{2D} + \alpha_2 \Delta t \Big[\, \mathrm{Res}(W^{(0)}, ||J||^N_{2D})\\
&\quad + \mathrm{Res}(W^{(1)}, ||J||^{N+1}_{2D})\Big]\\
W^{(N+1)} &= W^{(2)}
\end{aligned}$$

The superscripts $(0), (1)$, and (2) represent the stage number, and the superscripts N and $N+1$ represent the respective time levels. The stage coefficients $\alpha_1 = 1.0$ and $\alpha_2 = 0.5$ achieve 2nd order accuracy in time by recovering the Taylor Series expansion of the time derivative. This can be shown by collapsing the above scheme line by line:

$$\begin{aligned}
W^{[N+1]}||J||_{2D}^{N+1} &= W^{[N]}||J||_{2D}^{N} + \alpha_2\Delta\tau\left[\frac{\partial(W^{[N]}||J||_{2D}^{N})}{\partial\tau}\right.\\
&\quad \left. + \frac{\partial(W^{(1)}||J||_{2D}^{N+1})}{\partial\tau}\right]\\
&= W^{[N]}||J||_{2D}^{N} + \alpha_2\Delta\tau\left[\frac{\partial(W^{[N]}||J||_{2D}^{N})}{\partial\tau}\right.\\
&\quad \left. + \frac{\partial[W^{[N]}||J||_{2D}^{N} + \alpha_1\Delta\tau\,\mathrm{Res}(W^{[N]}, ||J||_{2D}^{N})]}{\partial\tau}\right]\\
&= W^{[N]}||J||_{2D}^{N} + \alpha_2\Delta\tau\left[\frac{\partial(W^{[N]}||J||_{2D}^{N})}{\partial\tau}\right.\\
&\quad \left. + \frac{\partial(W^{[N]}||J||_{2D}^{N})}{\partial\tau} + \alpha_1\Delta\tau\frac{\partial^2(W^{[N]}||J||_{2D}^{N})}{\partial\tau^2}\right]\\
&= W^{[N]}||J||_{2D}^{N} + 2\alpha_2\Delta\tau\frac{\partial(W^{[N]}||J||_{2D}^{N})}{\partial\tau}\\
&\quad +\alpha_1\alpha_2\Delta\tau^2\frac{\partial^2(W^{[N]}||J||_{2D}^{N})}{\partial\tau^2}
\end{aligned} \tag{4.52}$$

Which is equal to the second order accurate Taylor series expansion of $W^{[N+1]}||J||_{2D}^{N+1}$ around $W^{[N]}||J||_{2D}^{N}$ with $\alpha_1 = 1.0$ and $\alpha_2 = 0.5$. Note that if the geometry of the flow domain is not moving, this further simplifies to a 2-stage time accurate Runge-Kutta scheme.

4.4 Convergence of the Viscous Stream Function

At each time step the viscous correction stream function corresponding to the new vorticity must be found. The new stream function is used to construct the velocity at the new time step. The stream function is related to vorticity as follows:

$$\frac{\partial^2\psi}{\partial x^2} + \frac{\partial^2\psi}{\partial y^2} = \omega \tag{4.53}$$

The above equation is an elliptic partial differential equation. The solution to an elliptic equation is completely dictated from the boundary conditions and source terms. This means that for any given set of boundary conditions there exists a unique solution to the elliptic equation. To numerically solve this equation an iterative procedure must be constructed and the iteration variable must be driven to some convergence criteria. The method chosen to solve this equation is an approximate LU factorization scheme. The convergence of the solution is accelerated by applying multigrid.

An approximate LU factorization is also used for the solution of the potential field for the flow, Equation (4.2). An explanation of the solution scheme will be given for the viscous stream function equation. The process would be the same for the potential equation, the only difference being there is a different source term on the right hand side of Equation (4.2).

4.4.1 Approximate LU Factorization

The LU scheme is based on the implicit time marching of a pseudo-time dependant equation. The goal is to march this pseudo-time dependant equation to steady state and this steady state solution is exactly equal to the solution of the elliptic equation (4.53). Since only the steady state solution is of interest, an implicit method is used, thus allowing the scheme to pseudo-time advance with as large a pseudo-timestep as possible.

The first step in deriving this method is to convert Equation (4.53) into a pseudo-time dependent partial differential equation. This is done by moving the source term (ω) to the left hand side of the equation, and setting the entire result equal to a pseudo-time derivative of the independant variable

ψ:

$$\frac{\partial \psi}{\partial \tilde{t}} = \frac{\partial^2 \psi}{\partial x^2} + \frac{\partial^2 \psi}{\partial y^2} - \omega = 0 \tag{4.54}$$

The time variable, $\tilde{t}$, is a pseudo time variable that differs from the global time variable. Solving Equation (4.54) means driving the pseudo time derivative to zero to produce the desired steady state solution.

Written with an implicit parameter, λ, this equation becomes:

$$\frac{\partial \psi}{\partial \tilde{t}} = \left((1 - \lambda) \left[\frac{\partial^2 \psi}{\partial x^2} + \frac{\partial^2 \psi}{\partial y^2} - \omega \right]^m + \lambda \left[\frac{\partial^2 \psi}{\partial x^2} + \frac{\partial^2 \psi}{\partial y^2} - \omega \right]^{m+1} \right) \tag{4.55}$$

When $\lambda = 0$ the equation is explicit, when $\lambda = 1$ the equation is fully implicit. The time derivative and counter, m, refer to the sequential steps of the pseudo time integration.

Approximating the pseudo time derivative as:

$$\frac{\partial \psi}{\partial \tilde{t}} = \frac{\psi^{m+1} - \psi^m}{\Delta \tilde{t}} = \frac{\Delta \psi^m}{\Delta \tilde{t}} \tag{4.56}$$

Applying Equation (4.56) to (4.55) and collecting terms with the implicit parameter on the left hand side we get:

$$\begin{aligned} \Delta \psi^m - \Delta \tilde{t} \lambda \left(\left[\frac{\partial^2 \psi}{\partial x^2} + \frac{\partial^2 \psi}{\partial y^2} \right]^{m+1} - \left[\frac{\partial^2 \psi}{\partial x^2} + \frac{\partial^2 \psi}{\partial y^2} \right]^m \right) = \\ \Delta \tilde{t} \left[\frac{\partial^2 \psi}{\partial x^2} + \frac{\partial^2 \psi}{\partial y^2} - \omega \right]^m \end{aligned} \tag{4.57}$$

Note here that ω is a constant so $\omega^{m+1} - \omega^m = 0$. Making use of the identity matrix I and putting into operator form we get:

$$\left[I - \Delta \tilde{t} \lambda \left(\frac{\partial^2}{\partial x^2} + \frac{\partial^2}{\partial y^2} \right) \right] \Delta \psi^m = \Delta \tilde{t} \left[\frac{\partial^2 \psi}{\partial x^2} + \frac{\partial^2 \psi}{\partial y^2} - \omega \right]^m \tag{4.58}$$

The term on the right hand side in square brackets is the residual (Res). Due to the fact that elliptic equations transmit information evenly in all directions, the second derivatives in the residual are discretized using a central difference approximation. $\Delta\tilde{t}$ is the time step of the pseudo integration. $\Delta\psi^m$ is the change in ψ with each pseudo time integration.

The approximate factorization is applied to the term on the left hand side in square brackets [65].

$$\begin{aligned} \left[I + \Delta\tilde{t}\lambda(\delta_x^- + \delta_y^-)\right]\left[I - \Delta\tilde{t}\lambda(\delta_x^+ + \delta_y^+)\right]\Delta\psi^m &= r\Delta\tilde{t}\,\mathrm{Res}^m \qquad (4.59) \\ \mathrm{LU}\Delta\psi^m &= r\Delta\tilde{t}\,\mathrm{Res}^m \end{aligned}$$

where r is a relaxation factor, L is the lower diagonal matrix, and U is the upper diagonal matrix. The approximate factorization is beneficial in that it minimizes array storage requirements, and allows a numerical solution procedure that is effectively two explicit sweeps through the domain. The four delta operators are defined below as:

$$\delta_x^+\Delta\psi = \frac{\Delta\psi_{i+1j} - \Delta\psi_{ij}}{\Delta x} \qquad (4.60)$$

$$\delta_x^-\Delta\psi = \frac{\Delta\psi_{ij} - \Delta\psi_{i-1j}}{\Delta x} \qquad (4.61)$$

$$\delta_y^+\Delta\psi = \frac{\Delta\psi_{ij+1} - \Delta\psi_{ij}}{\Delta y} \qquad (4.62)$$

$$\delta_y^-\Delta\psi = \frac{\Delta\psi_{ij} - \Delta\psi_{ij-1}}{\Delta y} \qquad (4.63)$$

Equation (4.59) is solved in two steps:

$$\begin{aligned} &(1) \quad \left[I + \Delta\tilde{t}\lambda(\delta_x^- + \delta_y^-)\right]\Delta\psi' = r\Delta\tilde{t}\,\mathrm{Res}^m \qquad (4.64) \\ &(2) \quad \left[I - \Delta\tilde{t}\lambda(\delta_x^+ + \delta_y^+)\right]\Delta\psi^m = \Delta\psi' \end{aligned}$$

The unknown in step (1) is $\Delta\psi'$. It is solved for by directly inverting the lower diagonal matrix constructed from the term in square brackets in step (1) of Equation (4.64). The unknown in step (2) is the change in the stream function, $\Delta\psi^m$. It is solved for by directly inverting the upper diagonal matrix constructed from the term in square brackets in step two of Equation (4.64). These two steps are effectively two explicit sweeps through the numerical domain shown below:

Step 1: Multiply through the operators in step 1 of Equation (4.64):

$$\Delta\psi'_{ij} + \Delta\tilde{t}\lambda(\Delta\psi'_{ij} - \Delta\psi'_{i-1j} + \Delta\psi'_{ij} - \Delta\psi'_{ij-1}) = r\Delta\tilde{t}\mathrm{Res}^m_{ij} \quad (4.65)$$

Rearranging we get:

$$\Delta\psi'_{ij} = \frac{r\Delta\tilde{t}\mathrm{Res}^m_{ij} + \Delta\tilde{t}\lambda(\Delta\psi'_{i-1j} + \Delta\psi'_{ij-1})}{1 + 2\Delta\tilde{t}\lambda} \quad (4.66)$$

By setting $\Delta\psi'_{ij}$ equal to zero in the boundary cells, the above equation is an explicit calculation of $\Delta\psi'_{ij}$.

Step 2: Multiplying through the operators in step 2 of Equation (4.64) and noting that $\Delta\psi'_{ij}$ was calculated everywhere in the domain using Equation (4.66) we get:

$$\Delta\psi^m_{ij} - \Delta\tilde{t}\lambda(\Delta\psi^m_{i+1j} - \Delta\psi^m_{ij} + \Delta\psi^m_{ij+1} - \Delta\psi^m_{ij}) = \Delta\psi'_{ij} \quad (4.67)$$

Rearranging we get:

$$\Delta\psi^m_{ij} = \frac{\Delta\psi'_{ij} + \Delta\tilde{t}\lambda(\Delta\psi^m_{i+1j} + \Delta\psi^m_{ij+1})}{1 + 2\Delta\tilde{t}\lambda} \quad (4.68)$$

Which is an explicit calculation of $\Delta\psi_{ij}^{m}$, with $\Delta\psi_{ij}^{m}$ being set to zero in the boundary cells. Note that the explicit sweep across the domain in this step is in the reverse direction.

The stream function ψ is updated every pseudo-time iteration using the following formula:

$$\psi_{ij}^{m+1} = \psi_{ij}^{m} + \Delta\psi_{ij}^{m} \tag{4.69}$$

The implicit parameter and relaxation factor for this scheme are both given values of 1. The technique described above is also used to solve the potential equation, Equation (4.2). For this equation the implicit parameter is 0.5 and the relaxation factor is 1.

4.4.2 Multigrid Convergence Acceleration

Equation (4.53) is a steady state elliptic equation which must be iterated to convergence for each time step. Steady state elliptic equations have their solutions governed by the boundary conditions. The faster that information on the boundaries can influence the interior of the domain the faster the solution will converge. Multigrid methods increase the speed at which information at the boundaries is spread throughout the numerical domain [62]. This can be interpreted as low frequency error damping. The approximate LU factorization scheme has excellent high frequency error damping. Therefore, combining multigrid with the LU scheme greatly decreases the number of iterations required to converge the solution [63].

Multigrid increases the transmission speed of boundary condition information by performing calculations on coarse meshes. The difference between the coarse mesh calculation and the fine mesh calculation interpolated to the coarse mesh, is used as a correction to the fine mesh solution. The multigrid technique used in the current work employs geometric coarsening of the mesh. This occurs by eliminating every second grid point thus combining four fine grid cells into a single coarse grid cell. Figure (4.2) is an example of the coarsening of the grid. The h level of the grid is the finest grid, and each level lower is labeled as $h - n$ where n represents the number of times the grid cells have been combined.

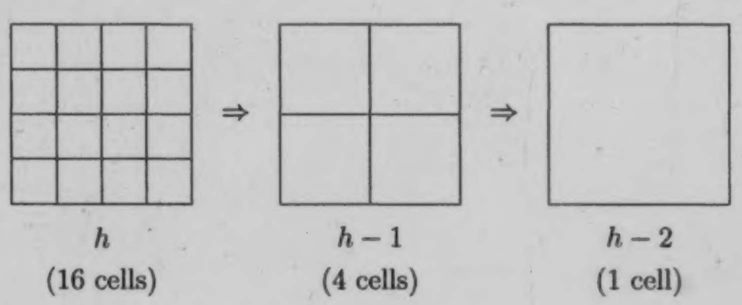

Figure 4.2: Multigrid Grid Levels

A multigrid cycle begins by calculating a solution correction on the fine grid and the new solution after this correction is applied [62]. This is shown below written in operator form.

$$\mathrm{LU}_h \Delta\psi_h^m = \Delta\tilde{t}\mathrm{Res}_h^m \tag{4.70}$$

$$\psi_h^{m+1} = \psi_h^m + \Delta\psi_h^m \tag{4.71}$$

where L and U are lower and upper operators respectively, Res_h is the residual on the h grid level and $\Delta\psi_h^m$ is the correction to ψ on the h grid level. m is the iteration counter indicating the number of multigrid cycles performed.

This new solution is passed down to the next coarsest grid by an area weighted accumulation method, denoted by the operator T.

$$\psi^t_{h-1} = T^h_{h-1}\psi_h \tag{4.72}$$

where ψ^t_{h-1} represents the transferred ψ solution on the coarser $(h-1)$ grid. The residuals that were calculated on the fine grid are passed down to the next coarsest grid by a direct summation thus getting 'transferred' residuals that correspond to the grid cells of the coarser grid. This direct summation is denoted by the operator $\tilde{T}$

$$\mathrm{Res}^t_{h-1} = \tilde{T}^h_{h-1}\mathrm{Res}_h \tag{4.73}$$

The transferred solution, ψ^t_{h-1}, is now used to calculate a coarse grid residual, denoted Res^c_{h-1}.

$$\begin{aligned} \mathrm{Res}^c_{h-1} &= \mathrm{Res}(\psi^t_{h-1})_{h-1} \\ &= \mathrm{Res}(T^h_{h-1}\psi_h)_{h-1} \end{aligned} \tag{4.74}$$

The difference between the residual passed down from the fine grid (transferred residual) and the calculated residual on the coarse grid is known as the forcing function, FF.

$$\begin{aligned} \mathrm{FF}_{h-1} &= \mathrm{Res}^t_{h-1} - \mathrm{Res}^c_{h-1} \\ &= \tilde{T}^h_{h-1}\mathrm{Res}_h - \mathrm{Res}(T^h_{h-1}\psi_h)_{h-1} \end{aligned} \tag{4.75}$$

The new solution residual on the coarse grid is the sum of the residual calculated with the solution at the coarse grid, and the forcing function.

$$\begin{aligned} \mathrm{LU}_{h-1}\Delta\psi_{h-1} &= \Delta\tilde{t}(\mathrm{Res}_{h-1} + \mathrm{FF}_{h-1}) \\ &= \Delta\tilde{t}(\mathrm{Res}_{h-1} + \tilde{T}^{h}_{h-1}\mathrm{Res}_{h} - \mathrm{Res}(T^{h}_{h-1}\psi_h)_{h-1}) \end{aligned} \tag{4.76}$$

The new coarse grid solution (ψ'_{h-1}) is calculated using the solution correction ($\Delta\psi_{h-1}$) below:

$$\psi'_{h-1} = \psi_{h-1} + \Delta\psi_{h-1} \tag{4.77}$$

It should be noted that more than one iteration of solving for a coarse grid solution may be done at any given grid level. This manner of calculating on the present grid and passing information to coarser grids continues until the lowest grid level is reached.

At this point the process of passing the coarse grid correction values upwards to the finer grids begins. At each up-pass the difference between the transferred fine grid solution and the coarse grid solution is interpolated up to the fine grid. This is used to calculate a new fine grid solution.

$$\psi'_h = \psi_h + \tilde{I}^{h-1}_{h}(\psi'_{h-1} - T^{h}_{h-1}\psi_h) \tag{4.78}$$

Where $\tilde{I}$ is an operator that interpolates a coarse grid correction up to a fine grid. The interpolation operator is a weighted bilinear average [62]. Passing the solution corrections up to the finer meshes continues in a 'W' cycle until the uppermost mesh is reached, see Figure (4.3).

The operators T and $\tilde{I}$ are transfer and interpolation operators used to pass information down and up, respectively, between the grid levels. They are not inverses of each other.

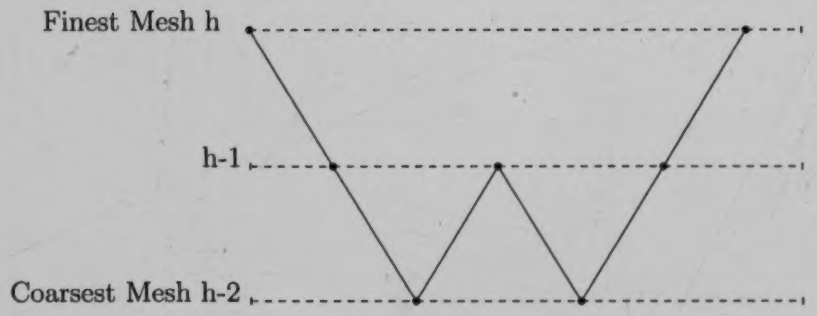

Figure 4.3: Schematic of Three Level ‘W’ Cycle used in Multigrid Scheme

A three level ‘W’ cycle is the multigrid scheme used for the current work. At each time-step the maximum residual is reduced to the order of $O(10^{-9})$ before the equation is considered to be converged. One complete multigrid cycle is shown in Figure (4.3).

4.5 Numerical Stability and the Global Timestep

The time stepping method being used to time advance the transport equations in the fluid, Equations (3.107) and (3.110), is an explicit technique; the method used to time advance the energy equation in the solid, Equation (3.113), is a single step technique with multi-stage iterative convergence. Therefore the numerical stability with respect to the global time step is an issue.

As mentioned previously, the time integration technique used to solve the transport equations in the fluid, (3.107) and (3.110), reduces to a two-stage explicit Runge-Kutta scheme when the grid is stationary. Yokota [64] solves transport equations similar in form to Equations (3.107) and (3.110), using this method. He indicated that to maintain both time accuracy and stability a global timestep should be used such that the Courant number in the smallest grid cell is one half. This indicates that as long as the timestep is small, numerical stability is achieved.

The single step time integration scheme used to solve the energy equation in the solid, Equation (4.11), reduces to a scheme similar in form to the one Reaume [42] solved in the solid when the grid is stationary. The Von Neumann stability analysis performed there indicated that the scheme placed no limitations on the allowable time step size in the solid.

The stability criteria for stationary grid calculations above were deemed satisfactory for the present scheme provided a convergence test was performed with differing time-step sizes. The present code was ran through four cycles of periodic vortex shedding with timestep sizes of $\Delta t = 0.2(10^{-4})$s and $\Delta t = 0.2(10^{-5})$s. The vorticity and temperature solutions in the fluid were compared at the end of these simulations. The maximum difference in the vorticity and temperature fields at the end of these two simulations were found to be less than 1%. Therefore a time-step of $\Delta t = 0.2(10^{-4})$s was considered to be stable for the numerical scheme used in this work, and is used in all of the calculations done.

4.6 Numerical Domain

The numerical grid upon which the governing equations will be solved will now be described. The geometry of both the fluid and solid domains are dependent on the phase of the SMA wire, in turn each individual grid cell moves and changes shape over time. Therefore there is no single grid upon which solutions will be found. However, they all have the same general form. A grid generation algorithm is employed to reconstruct the grid at each timestep. The outer boundaries of the flow domain are held fixed, therefore only the solid boundary and internal grid cells are allowed to change.

Figure (4.4) is an example of a grid geometry in the flow domain. It displays a pair of SMA wires in the infinite cascade. Calculations need only be done on the grid surrounding the lower SMA wire, provided that information is allowed to pass through the upper and lower periodic boundaries of the flow domain. The fluid region is an 'O' type grid consisting of 96 x 48 grid cells, corresponding to the number of cells in the ξ and η directions of the computational space. The grid is tightly packed near the solid boundary to accurately capture the viscous effects, including the boundary layer, that dominate the flow there. The left side of the grid is the inflow boundary, and the right side is the outflow boundary. Both the inflow and outflow boundaries are curved to ensure smooth grid lines at these locations.

Figure (4.5) is the developed grid in the solid domain. The only physical boundary in the solid region is the outer most grid line, corresponding to the fluid solid interface. The solid domain consists of 96 x 12 grid cells and is also in an 'O' type grid configuration.

The number of grid cells in the fluid and solid was chosen by performing calculations using grids that contained both more and fewer grid cells. Calculations were done in the fluid region with grids of size 96 x 32, 96 x 48, and 96 x 64. Calculations were done in the solid region with grids of size 96 x 12 and 96 x 24. Comparisons between those calculations resulted in the current choice of the number of grid cells and packing, 96 x 48 in the fluid, and 96 x 12 in the solid.

The unwrapping of the O-grid mesh in the fluid domain is illustrated in Figure (4.6). This is the specific mapping of the grid from $x - y$ space to $\xi - \eta$ space. The inflow boundary is between the grid points G-H. The outflow boundary is between the grid points I-H and E-D. The solid boundary is between the grid points A-B-C. The periodic boundary of the cascade is between grid points H-G and F-E. Due to the manner in which the O-grid is unwrapped a seam is formed in the interior of the flow domain shown in Figure (4.6) between grid points I-A and C-D. These boundaries are periodic with one another allowing information to pass directly through.

The O-grid in the solid is unwrapped in exactly the same manner as the grid in the fluid.

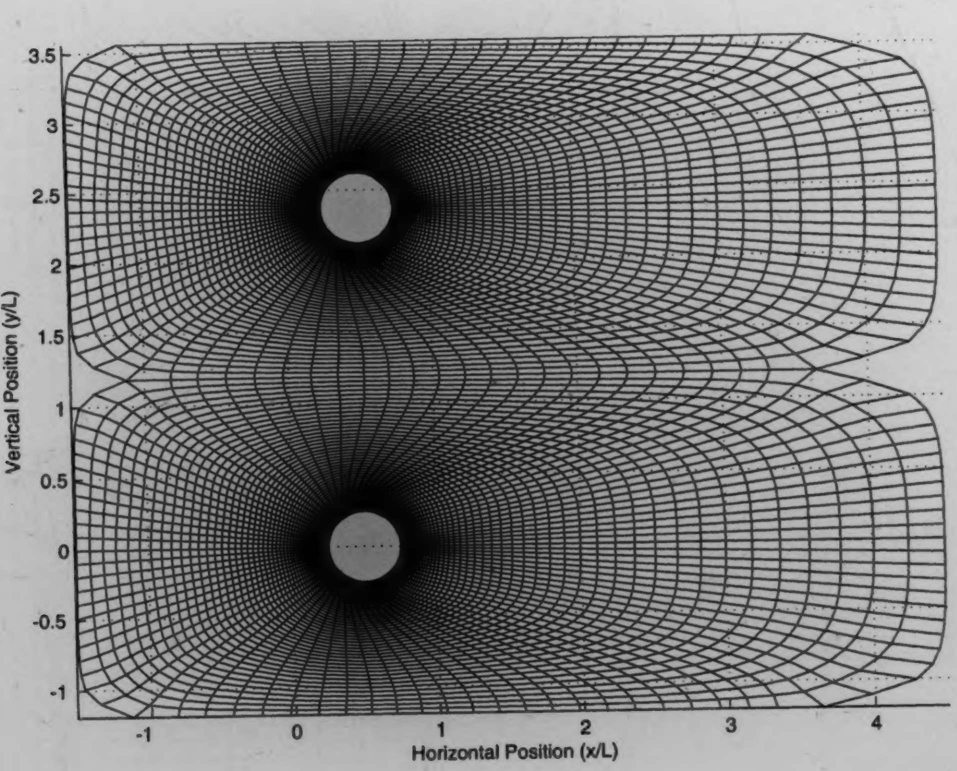

Figure 4.4: Developed Grid in Fluid Domain

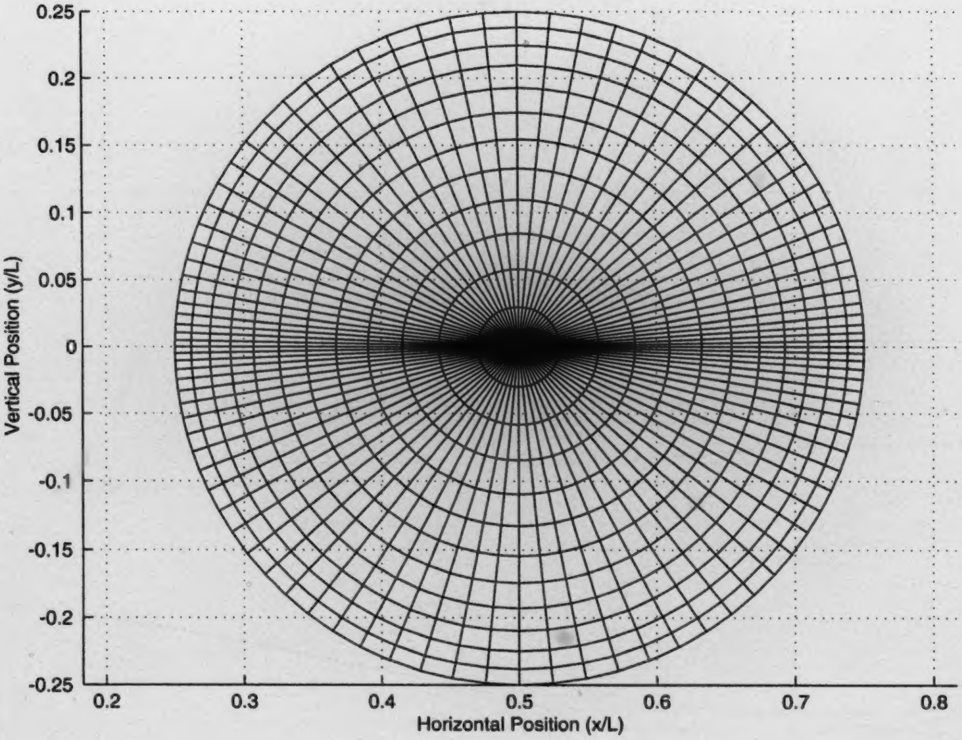

Figure 4.5: Developed Grid in Solid Domain

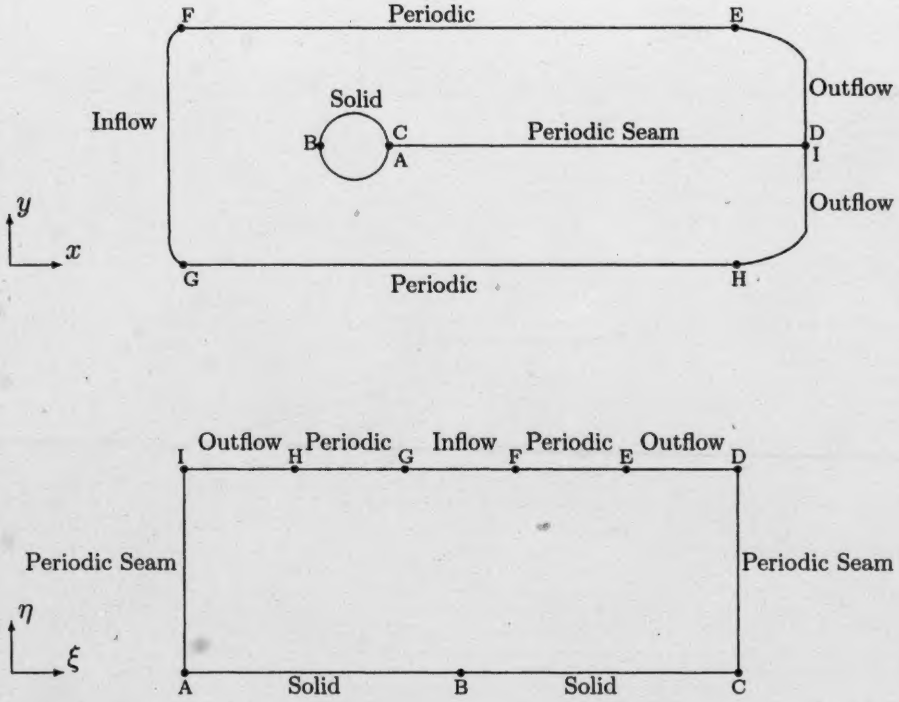

Figure 4.6: O-Grid Mapping to Computational Space

4.6.1 Initial Grid Construction

The method used to develop the initial numerical fluid domain grid used in this work will now be described. The problem discription called for a cascade of SMA wires with a diameter of 0.5mm. This cascade could be simulated by a boundary fitted structured O-grid around one individual SMA wire. The packing was required to be very tight near the boundary of the solid to capture important viscous effects. The vertical spacing between SMA wire centres was set equal to that of Reaume [42] at 2.37mm. The SMA wire's centre was set at (0.5mm, 0), with respect to the domain axes. The inflow boundary was set at $x = -1.5$mm and the outflow boundary was set at $x = 4.5$mm.

Figure (4.7) is the initial constructed grid that met the above requirements. It should be reiterated here that the radial grid lines are lines of constant ξ and the encircling grid lines are lines of constant η. With the outer boundaries of the domain defined, the first grid cell up from the solid boundary was set to have a constant thickness of 0.01mm all around. These first grid cells were the smallest grid cells and an iterative geometric packing algorithm was used to construct each grid cell up from the surface in the η direction. An example of this mathematically, along a horizontal grid line, is:

$$x_{ij} = x_{ij-1} + (x_{ij-1} - x_{ij-2})^a \qquad (4.79)$$

where x_{ij} is the x position of the ij grid point and $a > 1$ is a constant. The parameter a increases the size of the grid cells towards the domain boundary (η direction), along a given radial (ξ) line. It is determined iteratively such that all of the grid cells lie inside the set domain boundaries. The radial grid lines were set to be perpendicular to the solid surface for the first 13 grid cells up, and then the angle was changed such that the radial grid lines intersected with the set boundaries.

It is obvious that from Figure (4.7) that the grid lines are not smooth, and contain many discontinuities in their curvature. The discontinuous nature of these grid lines may have a deleterious effect upon numerical solutions found using this grid. Therefore a grid smoothing algorithm was constructed and used to obtain a smooth grid.

The principles of grid smoothing are based in elliptic grid generation. A full explanation of numerical elliptic grid generation can be found in Thompson *et al* [53]. Elliptic grid generation is essentially treating the grid coordinates as solutions to a system of elliptic partial differential equations, who's boundary conditions are the physical boundaries of the domain being discretized. The Laplacian of the computational coordinates is the most common system of elliptic equations used to generate a grid [53]:

$$\begin{aligned} \nabla^2 \xi &= 0 \\ \nabla^2 \eta &= 0 \end{aligned} \tag{4.80}$$

These two equations can be inverted such that (x, y) are the dependant variables:

$$\begin{aligned} \alpha \frac{\partial^2 x}{\partial \xi^2} - 2\beta \frac{\partial^2 x}{\partial \xi \partial \eta} + \gamma \frac{\partial^2 x}{\partial \eta^2} &= 0 \\ \alpha \frac{\partial^2 y}{\partial \xi^2} - 2\beta \frac{\partial^2 y}{\partial \xi \partial \eta} + \gamma \frac{\partial^2 y}{\partial \eta^2} &= 0 \end{aligned} \tag{4.81}$$

where:

$$\begin{aligned} \alpha &= \left(\frac{\partial x}{\partial \eta}\right)^2 + \left(\frac{\partial y}{\partial \eta}\right)^2 \\ \beta &= \left(\frac{\partial x}{\partial \xi}\right)\left(\frac{\partial x}{\partial \eta}\right) + \left(\frac{\partial y}{\partial \xi}\right)\left(\frac{\partial y}{\partial \eta}\right) \\ \gamma &= \left(\frac{\partial x}{\partial \xi}\right)^2 + \left(\frac{\partial y}{\partial \xi}\right)^2 \end{aligned} \tag{4.82}$$

If the above equations were used in their current form they would completely smooth out the packing that was constructed in Figure (4.7). This is due to their elliptic nature. We only want to use the smoothing effect of these equations to smooth the grid lines such that they have continuous curvature. Therefore Equation (4.81) is converted into a pseudo-time ($\tilde{t}$) dependant equation by adding a pseudo-time derivative to the right hand side:

$$\begin{aligned}\frac{\partial x}{\partial \tilde{t}} &= \alpha\frac{\partial^2 x}{\partial \xi^2} - 2\beta\frac{\partial^2 x}{\partial \xi \partial \eta} + \gamma\frac{\partial^2 x}{\partial \eta^2} \\ \frac{\partial y}{\partial \tilde{t}} &= \alpha\frac{\partial^2 y}{\partial \xi^2} - 2\beta\frac{\partial^2 y}{\partial \xi \partial \eta} + \gamma\frac{\partial^2 y}{\partial \eta^2}\end{aligned} \tag{4.83}$$

These new equations are parabolic in nature. Their pseudo-time dependance allows us to time step to intermediate grid solutions that have smooth grid lines and still retain the packing that was constructed in Figure (4.7). These equations are discretized spatially using central differencing and marched through pseudo-time using a four stage Runge-Kutta scheme. By running the grid developed in Figure (4.7) through 150 smoothing iterations, the final grid is constructed and shown in Figure (4.8). The level of smoothness, and hence the number of smoothing iterations, was chosen solely on the qualitative appearance of the grid. The level of smoothness shown in Figure (4.8) was deemed sufficient for the numerical simulations performed in this work. Note that the inflow and outflow boundaries are curved thus ensuring smooth grid lines at these locations.

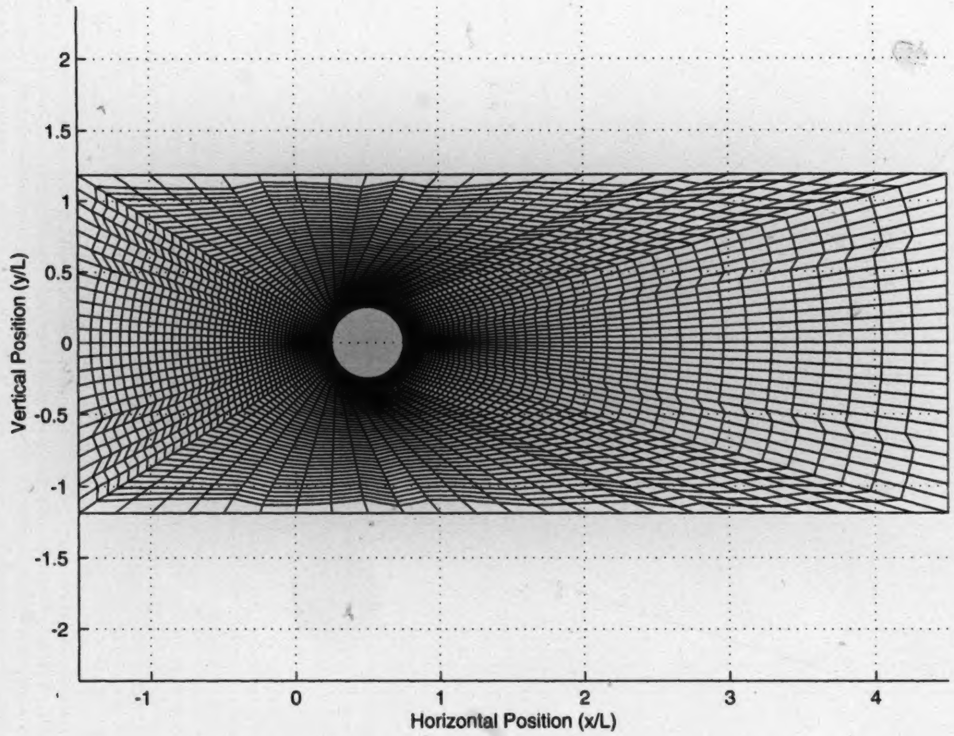

Figure 4.7: Unsmoothed Grid in the Fluid Domain

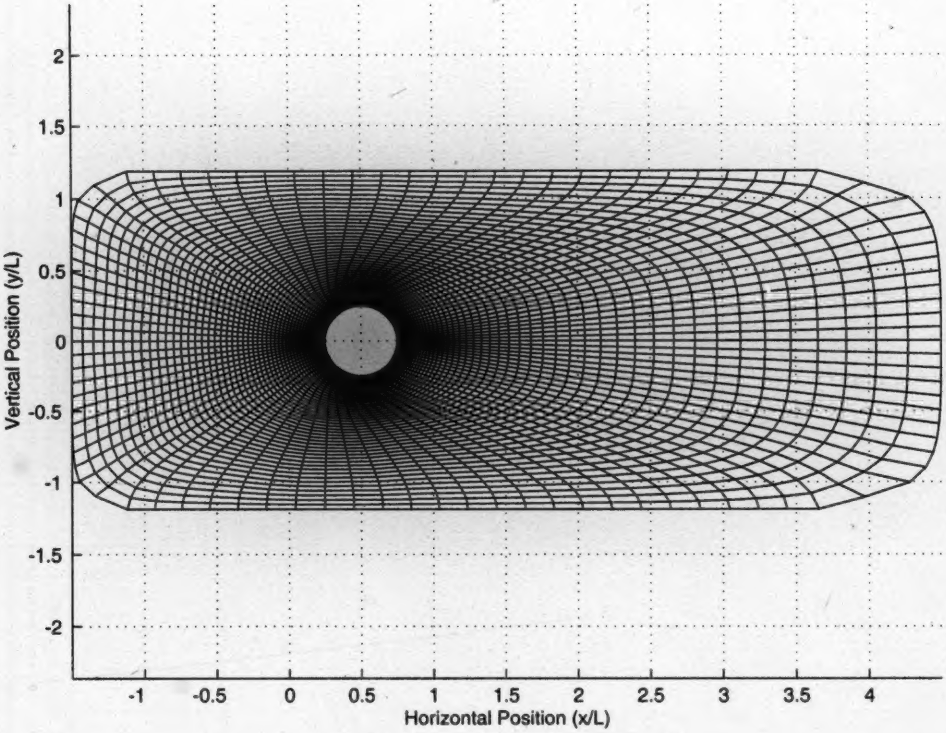

Figure 4.8: Smoothed Grid in the Fluid Domain

4.6.2 Grid Generation Procedure for Changing Grid

The grid generation method used to create the initial numerical grid in the last section cannot be used to reconstruct the grid every timestep as the SMA wire changes shape. Therefore a simple grid changing algorithm is employed. The initial grid is read in and stored as the basis for all of the grids generated during the numerical simulation. As the shape of the SMA changes, the code uses the initial grid as a starting point and adjusts the positions of the grid points to accomodate this shape change, while holding the outer boundaries fixed. This occurs every global timestep.

The adjustment process involves storing the change in x and y between successive grid points along each radial ξ grid line. These Δx's and Δy's are then normalized to the total linear distance of the radial ξ grid line:

$$\begin{aligned} \text{x proportion}_{ij} &= \frac{\Delta x_{ij}}{\text{Length}_i} \\ \text{y proportion}_{ij} &= \frac{\Delta y_{ij}}{\text{Length}_i} \end{aligned} \tag{4.84}$$

The change in SMA geometry results in a new total linear length of each radial grid line in the fluid domain. This new length is now multiplied against the proportions calculated in Equation (4.85) to get new Δx's and Δy's:

$$\begin{aligned} \Delta x_{ij} &= (\text{x proportion}_{ij})(\text{New Length}_i) \\ \Delta y_{ij} &= (\text{y proportion}_{ij})(\text{New Length}_i) \end{aligned} \tag{4.85}$$

The new Δx's and Δy's are then used to reconstruct the fluid grid. Unfortunately this technique does not guarantee that each grid line will have continuous curvature. Therefore, a grid smoother is once again employed, but is only used for 5 smoothing iterations. An example of a grid constructed using this procedure is shown in Figure (4.9). This grid is for an SMA who's cross-section is elliptical in shape.

It should be noted that at all times the radial grid lines of the grid cells adjacent to the solid boundary are kept perpendicular to the solid boundary. This grid generation procedure is performed every timestep to construct the flow domain for that timestep.

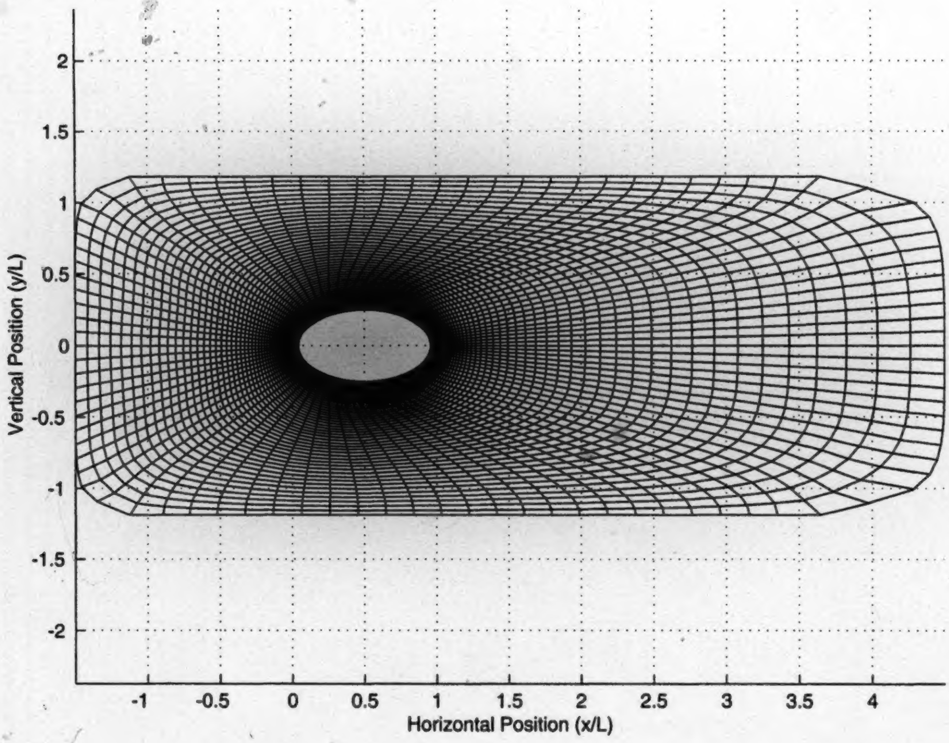

Figure 4.9: Constructed Grid Around Elliptical SMA

4.6.3 Solid Grid Generation

The solid domain grid is generated in a much simpler manner than the fluid domain grid, due to the simplicity of the geometry in the solid. Figure (4.5) is an example of a grid in the solid domain. The solid grid is constructed every timestep by taking the outer domain shape of the SMA at that timestep, and constructing concentric η grid lines with exactly the same proportional geometric shape. The spacing between these concentric η grid lines gets progressivly larger, in a linear fashion, as they approach the centre.

4.7 Boundary Conditions

The computational domain shown in Figure (4.6) has four different boundaries in the fluid: the inflow boundary, outflow boundary, periodic boundaries, and fluid-solid interface. In the solid there is only one physical boundary, occurring at the fluid-solid interface. The variables that require boundary conditions are the inviscid potential, ϕ, the viscous correction stream function, ψ, the vorticity, ω, and the temperature, T.

4.7.1 Periodic Boundary

The periodic boundary condition is constructed to represent the ability of fluid to pass between separate channels of a cascade of infinite SMA wires. Instead of constructing numerous cascade passages, only the flow in a single channel is calculated. The true flow is simulated by having flow information that leaves the bottom of the flow domain enter through the top of the flow domain and vice-versa. Computationally this means that the boundary cells of the lower boundary are filled with information from the cells along the upper boundary and vice-versa. This same technique is also used to pass information across the seam of the 'O'-grid used in the current work.

4.7.2 Inflow Boundary

The flow field boundary conditions at the inlet are constructed to model a uniform flow entering the domain. Recalling the velocity decompositions in Equations (3.33) and (3.34), a uniform flow across the inlet requires that there be no change in any of the flow variables across the inlet. The temperature at the inlet is set to the freestream temperature of the fluid (T_∞). Since uniform flow is assumed at the inlet, no vorticity can exist at the inlet, therefore the vorticity (ω) is set to zero there. These are represented mathematically by the following equations:

$$\left.\frac{\partial \phi}{\partial \eta}\right|_{inlet} = 0 \tag{4.86}$$

$$\left.\frac{\partial \psi}{\partial \eta}\right|_{inlet} = 0 \tag{4.87}$$

$$\omega_{inlet} = 0 \tag{4.88}$$

$$T_{inlet} = T_\infty \tag{4.89}$$

4.7.3 Outflow Boundary

The outflow boundary conditions were chosen to allow all flow phenomena to convect smoothly out of the domain. Therefore the derivatives of ψ and ω with respect to η are set to zero across the outlet, while the second derivative of T with respect to η is set to zero across the outlet. On the inlet and solid boundaries the derivative of the flow potential (ϕ) has been specified, i.e. Neuman boundary conditions. The flow potential equation (4.2) is solved to compute ϕ, and can only give solutions unique to a constant if only Neuman boundary conditions are given. Therefore it is necessary to prescribe a value for ϕ at the outlet such that we always achieve unique solutions. For simplicity the arbitrary value specified for ϕ is zero. These are represented mathematically by the following equations:

$$\phi_{outlet} = 0 \tag{4.90}$$

$$\left.\frac{\partial \psi}{\partial \eta}\right|_{outlet} = 0 \tag{4.91}$$

$$\left.\frac{\partial \omega}{\partial \eta}\right|_{outlet} = 0 \tag{4.92}$$

$$\left.\frac{\partial^2 T}{\partial \eta^2}\right|_{outlet} = 0 \tag{4.93}$$

4.7.4 Solid Boundary

Solid Boundary Condition for ψ

The viscous correction stream function (ψ) is calculated from Equation (4.1). All of the boundary conditions defined thus far for ψ have been Neumann or derivative boundary conditions. We can therefore only find solutions for ψ that are unique up to a constant. Therefore it is necessary to prescribe the value of ψ on the solid wall. The value for ψ is set to zero on the solid wall.

$$\psi_{wall} = 0 \tag{4.94}$$

No-Flux Boundary Condition

One of the most important boundary conditions in the flow field is the enforcement of the no-flux condition. It states that no fluid can flow across the boundary of the solid. The no flux condition is enforced through the construction of the potential, ϕ, at the solid boundary.

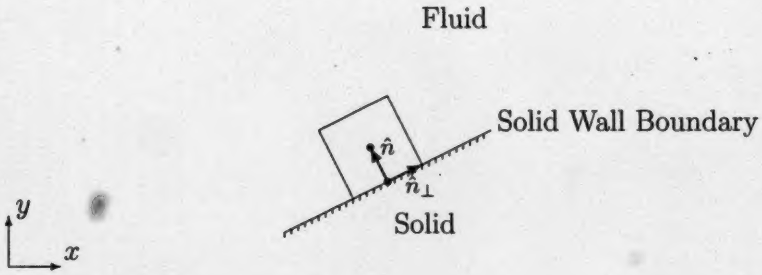

Figure 4.10: Solid Boundary Cell

Figure (4.10) is a diagram of a grid cell adjacent to the solid boundary. $\hat{n}$ is a vector perpendicular to the solid surface. Its length is equal to the perpendicular distance from the solid wall to the geometric cell centre of the adjacent grid cell. Since the geometry of the solid is changing, the solid walls have velocities equal to the grid velocities or time geometrics described by Equation (4.18). The difference between the fluid velocity and the wall velocity is the relative velocity at the wall. The no-flux condition mathematically is that this relative velocity perpendicular to the wall must equal zero.

$$[\vec{v}_{rel} \cdot \hat{n}]_{wall} \;=\; 0$$

$$(\vec{v} - \vec{v}_{grid}) \cdot \hat{n} \;=\; 0 \tag{4.95}$$

Defining n_x and n_y to be the projections of $\hat{n}$ in the x and y directions respectively and applying the velocity decompositions from Equations (3.33) and (3.34) to Equation (4.95) we get:

$$\frac{\left(U_\infty n_x + \frac{\partial\phi}{\partial x}\Big|_{wall} n_x - \frac{\partial\psi}{\partial y}\Big|_{wall} n_x - \frac{\partial x}{\partial t}\Big|_{wall} n_x\right)}{\Delta n} + \frac{\left(\frac{\partial\phi}{\partial y}\Big|_{wall} n_y + \frac{\partial\psi}{\partial x}\Big|_{wall} n_y - \frac{\partial y}{\partial t}\Big|_{wall} n_y\right)}{\Delta n} = 0 \tag{4.96}$$

At the solid surface the grid is constructed such that the grid lines in the ξ and η directions are exactly perpendicular. This allows us to use the following definitions:

$$\frac{\partial\phi}{\partial n}\Big|_{wall} = \frac{\partial\phi}{\partial\eta}\Big|_{wall} = \frac{\left(\frac{\partial\phi}{\partial x}\Big|_{wall} n_x + \frac{\partial\phi}{\partial y}\Big|_{wall} n_y\right)}{\Delta n} \tag{4.97}$$

$$\frac{\partial\psi}{\partial n_\perp}\Big|_{wall} = \frac{\partial\psi}{\partial\xi}\Big|_{wall} = \frac{\left(-\frac{\partial\psi}{\partial y}\Big|_{wall} n_x + \frac{\partial\psi}{\partial x}\Big|_{wall} n_y\right)}{\Delta n} \tag{4.98}$$

Where $\hat{n}_\perp$ is a vector the same length of $\hat{n}$ but directed along the wall, see Figure (4.10). We know from Equation (4.94) that ψ is constant on the wall so $\frac{\partial\psi}{\partial\xi}\Big|_{wall} = 0$. Applying this and Equations (4.97) and (4.98) to Equation (4.96) we get a definition for the derivative of ϕ with respect to η on the wall:

$$\frac{\partial\phi}{\partial\eta}\Big|_{wall} = -\frac{\left(U_\infty n_x - \frac{\partial x}{\partial t}\Big|_{wall} n_x - \frac{\partial y}{\partial t}\Big|_{wall} n_y\right)}{\Delta n} \tag{4.99}$$

The above boundary condition enforces the no-flux requirement at the moving solid wall. In addition to this, the transport equation fluxes at the wall are set to zero during the construction of the residuals (Equation 4.39). This is done to further enforce the no-flux requirement for moving solid boundaries.

No-Slip Boundary Condition

The no-slip boundary condition is also one of the most important boundary conditions in the flow field. The no-slip condition is the cause of the viscous effects in the fluid, and is what ultimately sets up the boundary layer that exists near the surface of the solid. These viscous effects are the major source of vorticity in the fluid. Thus the no-slip condition is used to construct the wall vorticity that is generated at any given timestep. The first step is to expand the the viscous correction stream function at the wall using a second order Taylor series:

$$\psi_{wall+1} = \psi_{wall} + \left.\frac{\partial \psi}{\partial n}\right|_{wall} \Delta n + \frac{1}{2!}\left.\frac{\partial^2 \psi}{\partial n^2}\right|_{wall} \Delta n^2 + O(\Delta n^3)... \qquad (4.100)$$

Where ψ_{wall+1} indicates the cell centred value of ψ in the first grid cell from the wall and $\hat{n}$ is the vector illustrated in Figure (4.10). Recalling the relationship between ω and ψ, Equation (4.1), we can conclude that $\left.\frac{\partial^2\psi}{\partial n^2}\right|_{wall} = \omega$. Applying this and Equation (4.94) to Equation (4.100) we get:

$$\psi_{wall+1} = \left.\frac{\partial \psi}{\partial n}\right|_{wall} \Delta n + \frac{1}{2}\omega_{wall}\Delta n^2 \qquad (4.101)$$

Rearranging this gives an expression for the vorticity at the wall:

$$\omega_{wall} = \frac{2(\psi_{wall+1} - \left.\frac{\partial \psi}{\partial n}\right|_{wall} \Delta n)}{\Delta n^2} \qquad (4.102)$$

The $\left.\frac{\partial\psi}{\partial n}\right|_{wall}$ term is constructed from the no-slip condition as follows. Define a vector $\hat{n}_\perp$ that is perpendicular to and the same size of the $\hat{n}$ vector in Figure (4.10), and is directed along the wall. The no-slip condition states that the relative fluid velocity, that is the difference between the fluid velocity and the velocity of the solid wall, along the wall is zero. Mathematically this is:

$$(\vec{v} - \vec{v}_{grid}) \cdot \hat{n}_\perp = 0 \tag{4.103}$$

Defining $n_{\perp x}$ and $n_{\perp y}$ to be the projections of $\hat{n}_\perp$ in the x and y directions respectively and applying the velocity decompositions from Equations (3.33) and (3.34) to Equation (4.103) we get:

$$\begin{aligned}&\frac{\left(U_\infty n_{\perp x} + \left.\frac{\partial\phi}{\partial x}\right|_{wall} n_{\perp x} - \left.\frac{\partial\psi}{\partial y}\right|_{wall} n_{\perp x} - \left.\frac{\partial x}{\partial t}\right|_{wall} n_{\perp x}\right)}{\Delta n}\\ &\qquad + \frac{\left(\left.\frac{\partial\phi}{\partial y}\right|_{wall} n_{\perp y} + \left.\frac{\partial\psi}{\partial x}\right|_{wall} n_{\perp y} - \left.\frac{\partial y}{\partial t}\right|_{wall} n_{\perp y}\right)}{\Delta n} = 0\end{aligned} \tag{4.104}$$

We can take advantage of the fact that $v_{n_\perp} = \frac{\partial\phi}{\partial n_\perp} - \frac{\partial\psi}{\partial n}$, and define:

$$-\left.\frac{\partial\psi}{\partial n}\right|_{wall} = \frac{\left(-\left.\frac{\partial\psi}{\partial y}\right|_{wall} n_{\perp x} + \left.\frac{\partial\psi}{\partial x}\right|_{wall} n_{\perp y}\right)}{\Delta n} \tag{4.105}$$

Applying this to Equation (4.104) and rearranging we end up with:

$$\begin{aligned}\left.\frac{\partial\psi}{\partial n}\right|_{wall} = \frac{1}{\Delta n}\Bigg(&U_\infty n_{\perp x} + \left.\frac{\partial\phi}{\partial x}\right|_{wall} n_{\perp x} - \left.\frac{\partial x}{\partial t}\right|_{wall} n_{\perp x}\\ &+ \left.\frac{\partial\phi}{\partial y}\right|_{wall} n_{\perp y} - \left.\frac{\partial y}{\partial t}\right|_{wall} n_{\perp y}\Bigg)\end{aligned} \tag{4.106}$$

Applying the above equation to Equation (4.102) completely defines the vorticity generation at the wall and satisfies the no slip condition for a moving boundary.

4.7.5 Thermal Interaction Boundary Condition

Reaume [42] developed the thermal interaction boundary condition used in this work. Numerically the thermal interaction boundary condition is what ties together the energy equations in the fluid and solid, Equations (3.73) and (3.74). Since it is the temperature of the SMA that determines the phase (ξ) and ultimately determines the geometry of the entire grid, any heat transfer to or from the surrounding fluid is of great interest.

The most common treatments of a thermal boundary condition between a solid and a surrounding fluid come in two separate classes. The first being to specify the temperature at the surface of the solid [12],[23],[24],[27],[44],[58]. The second being to specify the heat flux at the surface of the solid [24],[44],[58]. Neither of these two options are acceptable for the present work. These two classes of boundary conditions are unacceptable because they dictate the thermal state of the solid, and the main purpose of the current work is to allow for the natural time evolution of the thermal state of the solid.

The naturally occurring thermal boundary condition is that any heat transfer from the solid must flow into the fluid and vice-versa [42]. Both the solid and fluid domain are discretized at the wall such that each fluid boundary cell is adjacent to only one solid boundary cell. This is illustrated in Figure (4.11). Therefore the heat flux from any given solid boundary cell is transferred to it's adjacent fluid boundary cell. Mathematically this is written as:

$$q''_{fluid} = q''_{solid} \tag{4.107}$$

Conduction is the only mechanism of heat flux in the solid. Heat flux in

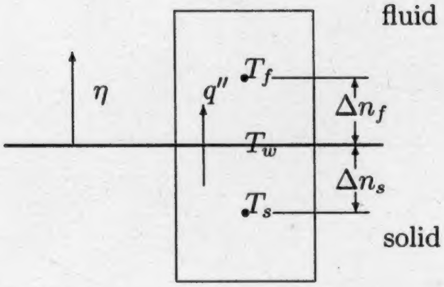

Figure 4.11: Heat Transfer at Boundary Cell

the fluid will be assumed to be a function of only conduction at the surface and temperature gradients are therefore linear in the fluid perpendicular to the solid surface. This is only valid if the viscous boundary layer is resolved by a fine enough grid at the solid surface. By using a flat plate boundary layer assumption to calculate the approximate boundary layer thickness it can be shown that the viscous boundary layer is contained in more than one grid cell from the surface of the solid [38], [42]. Therefore the grid is sufficiently fine to capture the viscous boundary layer, and the assumption of linear temperature gradients is valid. Thus, mathematically, Equation (4.107) becomes:

$$\left(k\frac{\partial T}{\partial n}\right)\bigg|_{fluid} = \left(k\frac{\partial T}{\partial n}\right)\bigg|_{solid} \tag{4.108}$$

Discretizing Equation (4.108) over the half cell we get:

$$k_f\left(\frac{T_f - T_w}{\Delta n_f}\right) = k_s\left(\frac{T_w - T_s}{\Delta n_s}\right) \tag{4.109}$$

Rearranging for the temperature at the wall (T_w) gives the thermal boundary condition at the wall:

$$T_w = \left[\frac{T_f + \left(\frac{k_s}{k_f}\right)\left(\frac{\Delta n_f}{\Delta n_s}\right) T_s}{1 + \left(\frac{k_s}{k_f}\right)\left(\frac{\Delta n_f}{\Delta n_s}\right)} \right] \tag{4.110}$$

CHAPTER 5

RESULTS

To demonstrate the usefulness of the numerical scheme developed, a number of test cases will be presented. The first being constant geometry examples followed by examples where the physical geometry of the SMA is changing. The real value of the numerical scheme to SMA actuator designers is in the differences in actuation behaviour between the presented test cases.

5.1 Fluid and Solid Material Properties

Property	Symbol	Value
Thermal conductivity	k	0.5W/mK
Density	ρ_o	1050kg/m^3
Volumetric thermal expansion coefficient	β	0.361(10^{-3})K^{-1}
Specific heat capacity	c_p	3.85(10^3)J/kgK
Viscosity	μ	2.09(10^{-3})kg/ms^2

Table 5.1: Fluid Material Properties

Prior to performing calculations, the fluid and solid material properties as well as the dimensionless numbers must be prescribed. The present work uses the same fluid and solid properties as Reaume [42].

The fluid properties are estimations for those of blood at 37°C. The source of the data is from Victor and Shah [56], and are shown in Table (5.1).

Table (5.2) contains the property values used for the SMA and are taken from Amalraj et al [1].

Property	Symbol	Value
Martensitic thermal conductivity	k_M	1.8W/mK
Austenitic thermal conductivity	k_A	18W/mK
SMA Density	ρ	6278kg/m^3
Volume specific heat capacity	ρc_p	2.12(10^6)J/m^{3}K
Latent energy of phase change	ρH	0.148(10^9)J/m^3
Austenitic Start Temperature	A_s^o	288K
Austenitic Finish Temperature	A_f^o	298K
Martensitic Start Temperature	M_s^o	262K
Martensitic Finish Temperature	M_f^o	252K

Table 5.2: Solid Material Properties

The reference parameters used for length is the maximum axial length of the SMA when it is in it's elliptic shape, 1mm. The freestream velocity (U_∞) of the fluid is 0.1m/s. The initial temperature of the solid ($T^{(solid)}_{(initial)}$) is 273K, and the initial temperature of the fluid ($T^{(fluid)}_{(initial)}$) is 310K. These parameters along with the material properties in Tables (5.1) and (5.2) are used to determine the dimensionless numbers shown in Table (5.3).

Dimensionless Group	Symbol	Value
Reynolds number	Re	50
Prantl number	Pr	16
Grashof number	Gr	245
Peclet number	Pe	118

Table 5.3: Dimensionless Numbers

5.2 Initial Periodic Flow Field

An initial condition is needed for the flow field around the SMA. Simply using the inviscid potential solution for flow around a solid cylinder as the initial condition is unacceptable to accurately model the early stages of the heat transfer with the viscous fluid. Transients from this physically inaccurate initial condition will alter the solution that develops over time. This problem is circumvented by performing an isothermal calculation around the solid cylinder until a viscous flow field develops that is free of initial start up transients. The viscous flow field around the cylinder in cross flow eventually develops into periodic vortex shedding. The periodic vortex shedding begins after a time equivalent to about four shedding cycles.

The initial condition for every two dimensional test case presented in this work is the flow field that results from an isothermal calculation of an additional three vortex shedding cycles after the first vortex is shed. This is done to guarantee that no initial start up transients exist in the flow field that could pollute the evolution of the thermal solution in the solid. Figures 5.1(a) to 5.1(e) show the vorticity contours over one full cycle of vortex shedding around a 0.5mm diameter cylinder. These plots illustrate one of the major unsteady characteristics of the flow field, namely the periodic vortex shedding nature of the flow.

Text resumes on page 112

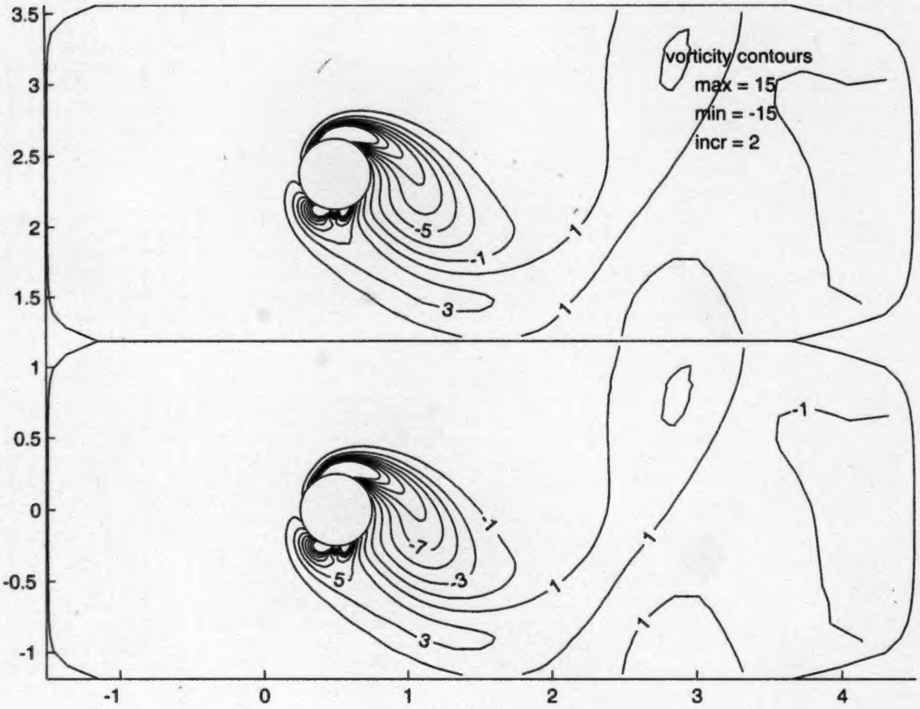

Figure 5.1(a): Vorticity Contours in Fluid Region, t = 0.008s

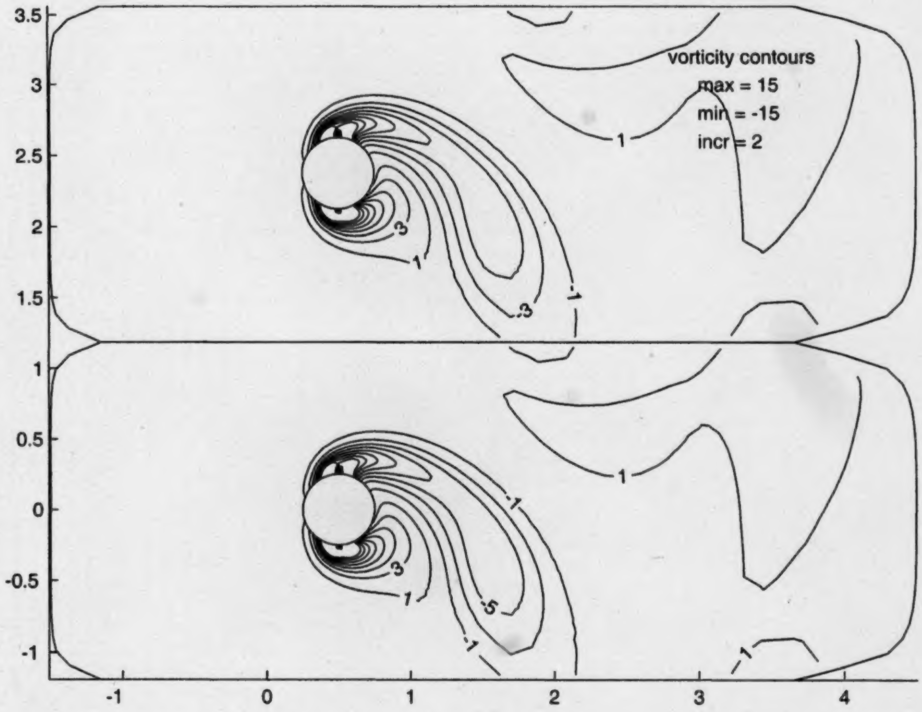

Figure 5.1(b): Vorticity Contours in Fluid Region, t = 0.016s

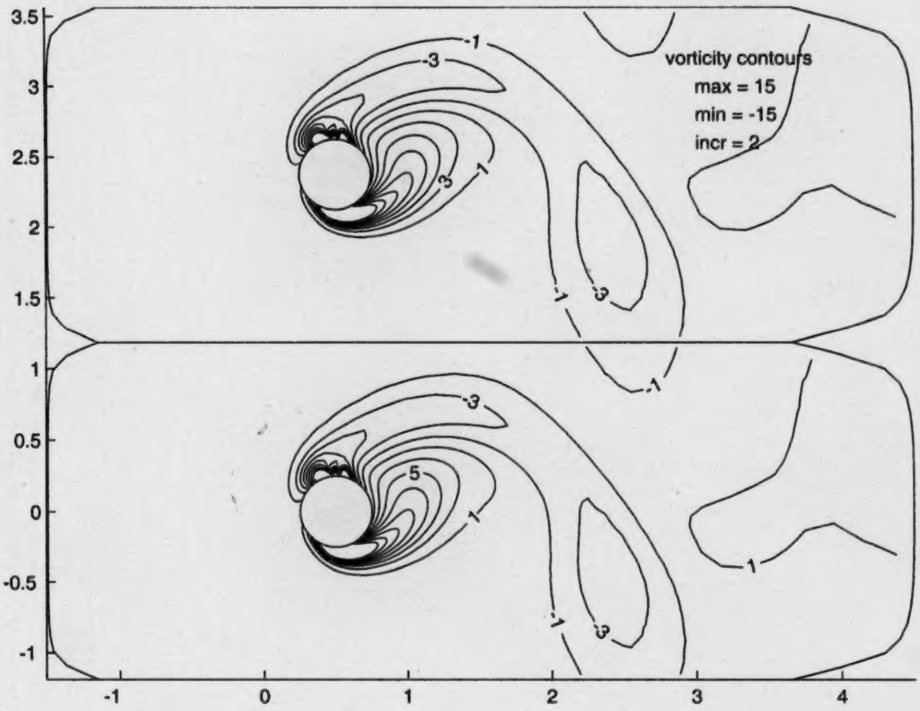

Figure 5.1(c): Vorticity Contours in Fluid Region, t = 0.024s

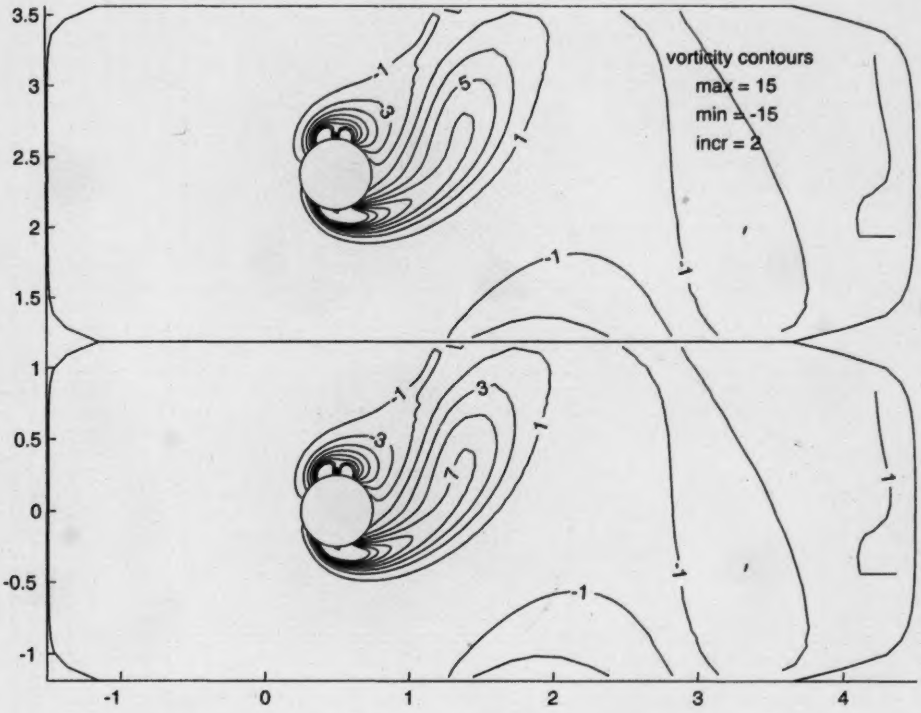

Figure 5.1(d): Vorticity Contours in Fluid Region, t = 0.032s

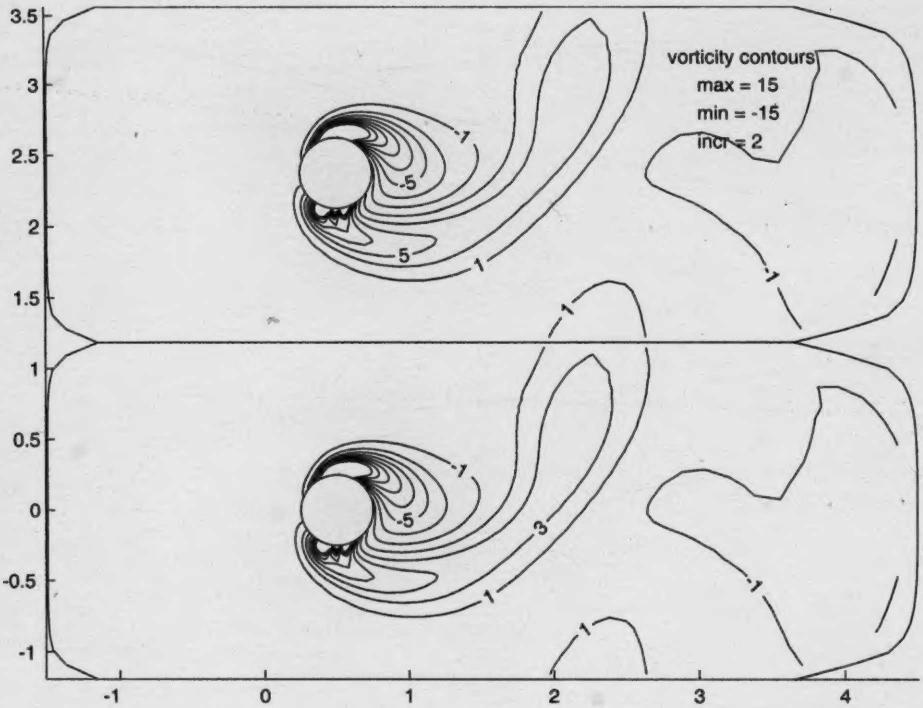

Figure 5.1(e): Vorticity Contours in Fluid Region, t = 0.040s

5.3 Constant Geometry Test Cases

5.3.1 Simulation of 0.5mm Diameter SMA Wire

The first test case to be presented is that of a shape memory alloy wire with a constant geometry. The geometry is shown in Figure (4.4), and is a circular wire with a diameter of 0.5mm. The initial temperature of the wire is 273K and the freestream temperature is 310K. The flow field initial condition used is the periodic solution from the isothermal simulation described in the last section. The dimensionless numbers used in the simulation are shown in Table (5.3), and the SMA properties are shown in Table (5.2).

As the calculation advances in time the SMA wire heats up and in turn changes its phase. Figures 5.2(a) to 5.2(e) are contour plots of the temperature in the cross section over a single cycle of vortex shedding. From these plots we can see the influence the vortex shedding has on the evolution of temperature in the solid. The location of the maximum temperature near the leading edge oscillates from top to bottom depending on the location of the stagnation point in the fluid domain. The stagnation point shifts due to the periodic shedding of vortices.

An area weighted average time history is shown in Figure (5.3). One of the main features of the time history of the solid is the initially high rate of temperature change, this is due to the large difference in initial temperatures of the solid and fluid. The large temperature difference causes a high initial heat transfer rate, thus increasing the temperature rapidly near the outer boundary of the solid. The second major feature is the small subtle oscillations that are most evident between $t = 0.10$s and $t = 0.14$s, as well as between $t = 0.03$s and $t = 0.09$s. These are due to the influence of the vortex shedding described earlier. The final major feature is the flattening out of the average temperature between $t = 0.02$s and $t = 0.10$s. This phenomenon is due to the fact that the temperature in this region is in between the austenitic start and finish temperatures (288K and 298K respectively), meaning that the phase of the solid is changing. Most of the heat energy that is being added to the solid during this time goes into changing the phase of the solid instead of increasing the temperature. Indeed this is the case when the area weighted average phase (ξ) history is plotted, Figure (5.4), and compared to the temperature history. The period of time that phase change is greatest corresponds exactly to the flattened part of the temperature history plot.

Close examination of the average phase history, Figure (5.4), reveals some influence of the vortex shedding as well. It manifests itself in the slight oscillation of the average phase throughout its actuation time.

The late time behaviour of the SMA in Figure (5.3) is simply an asymptotic approach to the freestream temperature. In this region the SMA has changed phase completely and is consequently of very little interest with respect to the actuation behaviour of SMA wires. For this reason all further test cases have only been run to the point of 99% complete phase change or $\xi = 0.99$.

The vortex shedding frequency for this test case was 54.5Hz, which corresponds to a Strouhal number (St) of 0.273. This Strouhal number is much higher than that predicted by Williamson [61] for a cylinder in an isothermal cross-flow, St=0.125. A higher Strouhal number was expected in the current work due to the fact that the bouyancy forces, caused by thermal gradients, tend to increase the shedding frequency, a fact pointed out by Chang and Sa [12]. In addition, the fact that the current simulation is of an infinite cascade of cylinders, also leads to the expectation of a higher shedding frequency than those predicted by Williamson [61].

Text resumes on page 122

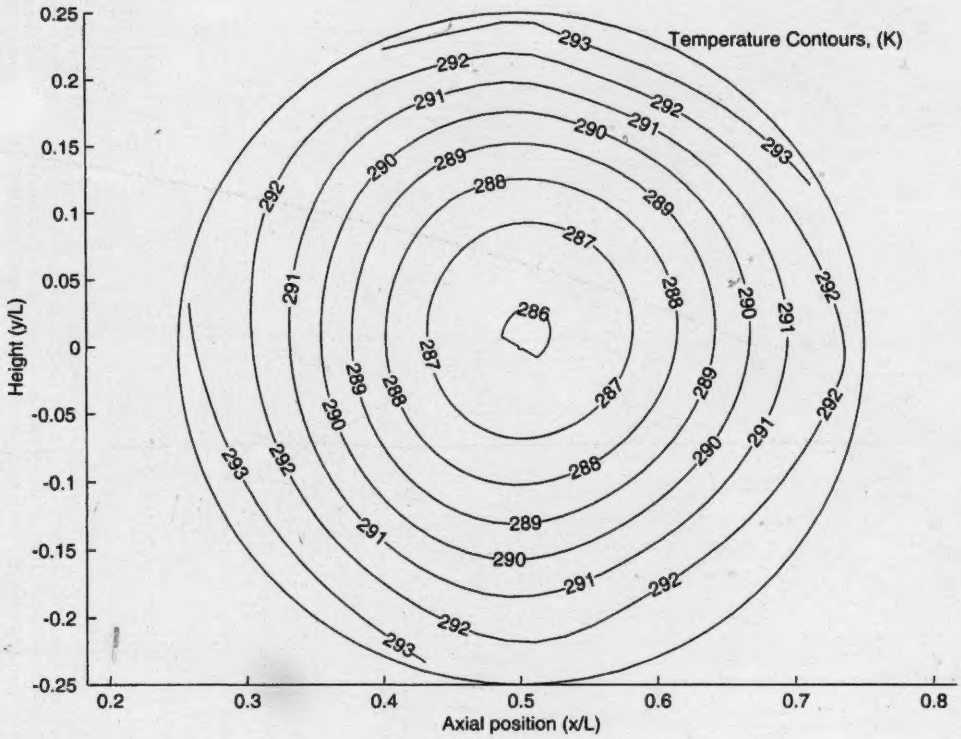

Figure 5.2(a): Temperature Contours of 0.5mm Diameter Constant Geometry, t = 0.02s

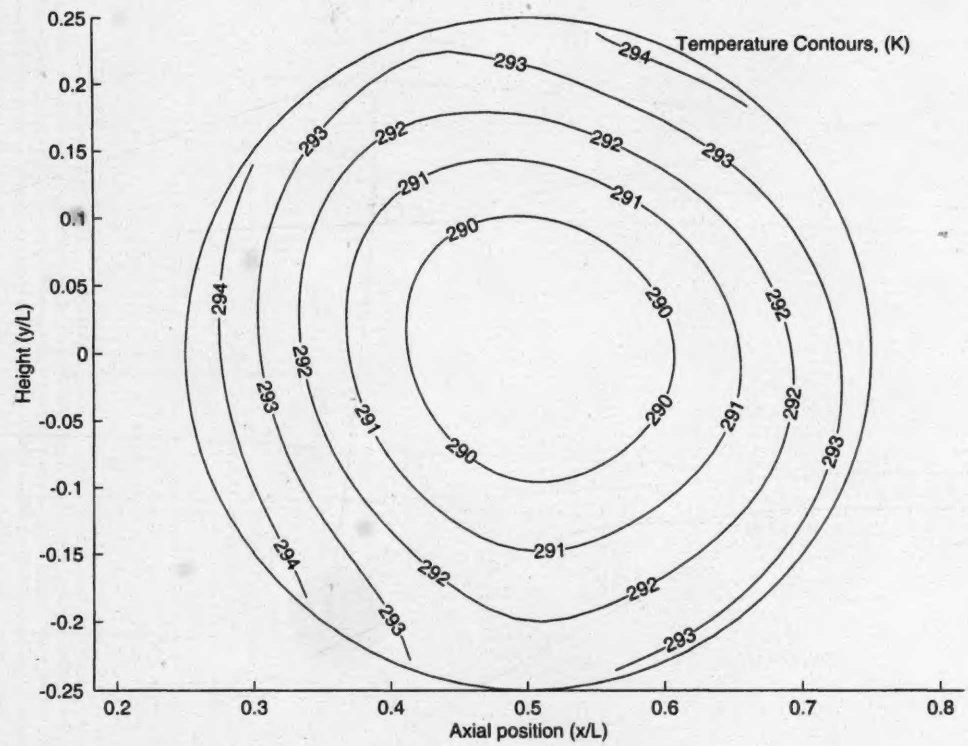

Figure 5.2(b): Temperature Contours of 0.5mm Diameter Constant Geometry, t = 0.03s

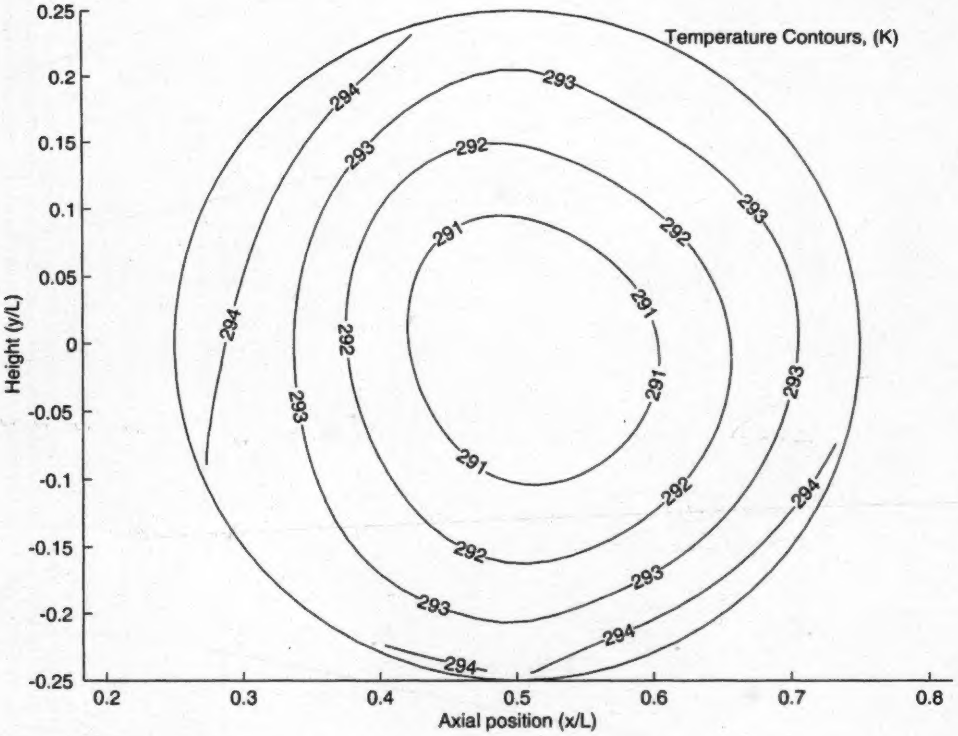

Figure 5.2(c): Temperature Contours of 0.5mm Diameter Constant Geometry, t = 0.04s

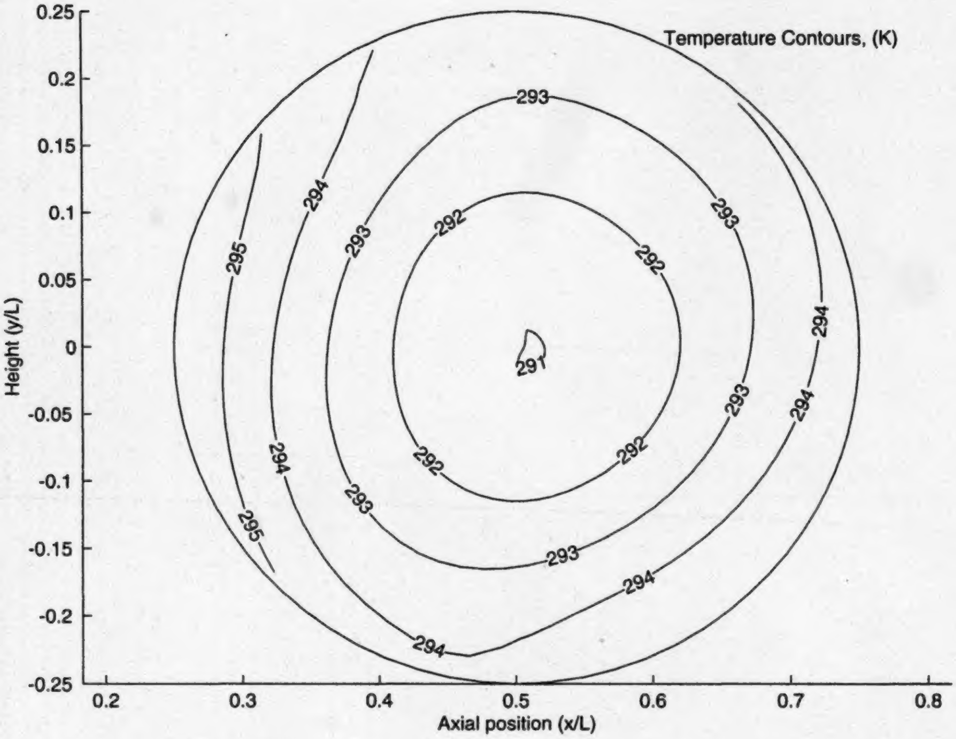

Figure 5.2(d): Temperature Contours of 0.5mm Diameter Constant Geometry, t = 0.05s

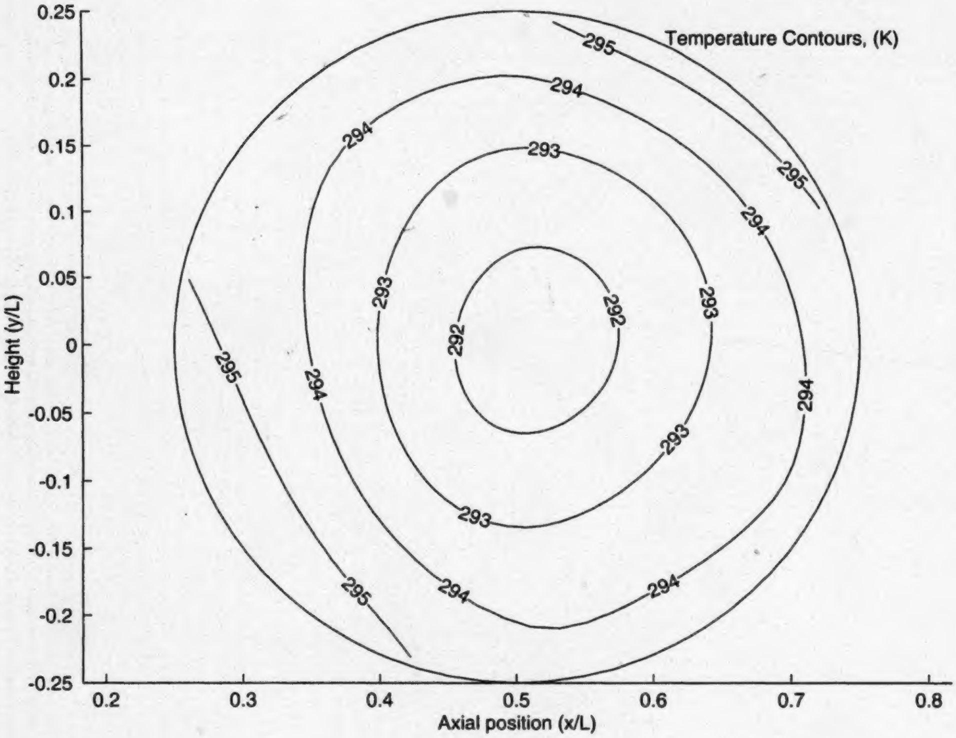

Figure 5.2(e): Temperature Contours of 0.5mm Diameter Constant Geometry, t = 0.06s

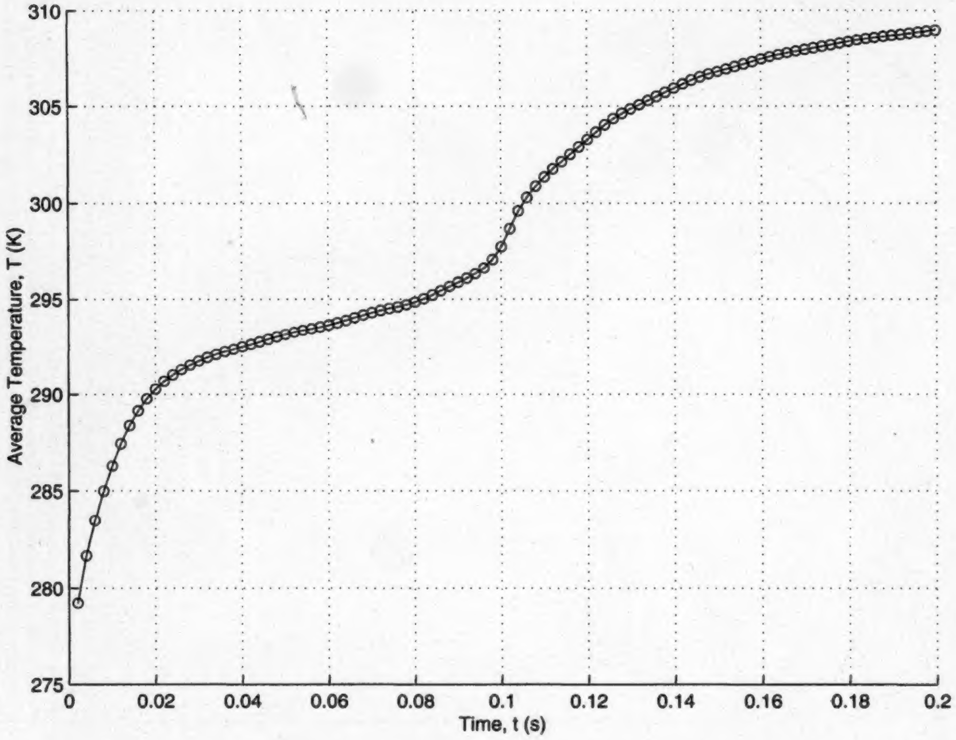

Figure 5.3: Average Temperature History for 0.5mm Diameter Constant Geometry

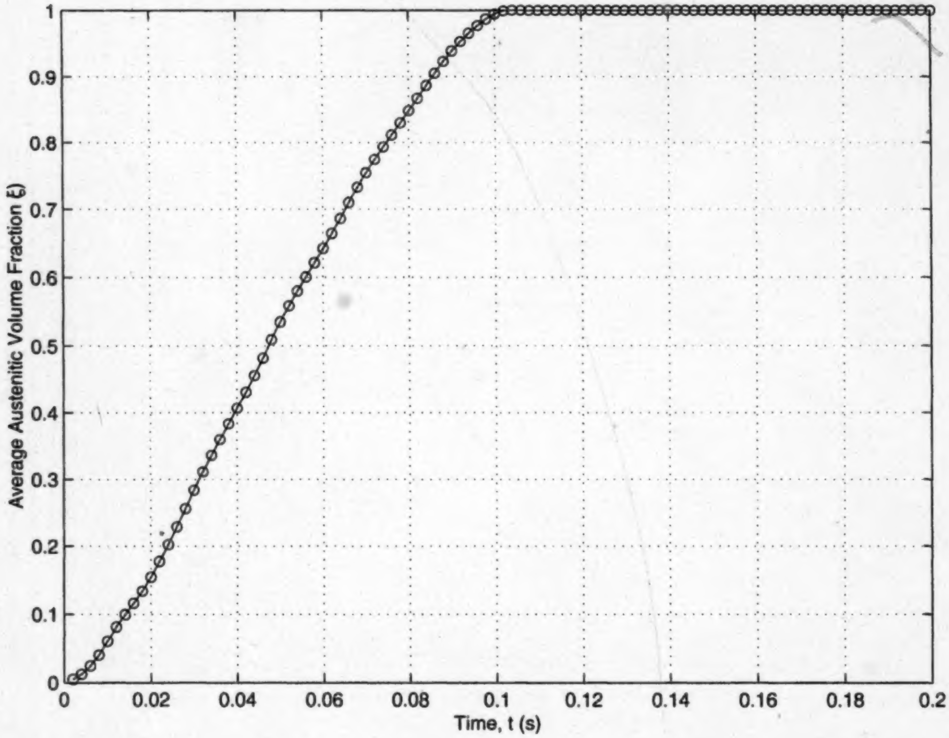

Figure 5.4: Average Phase History for 0.5mm Diameter Constant Geometry

5.3.2 Comparison to a Lumped Heat Capacitance Model

A lumped heat capacitance model can be used to approximate the heat transfer between a solid and a fluid [22]. The major assumption in this method is that the temperature of the solid is uniform over the cross section, in other words no temperature gradients. It is obvious from Figures 5.2(a) to 5.2(e) that the cross-sectional temperatures are not uniform. Due to the popularity of lumped heat capacitance approximation in the literature and for completeness, a comparison of a lumped heat capacitance model to the 2D analysis will be done.

From Fourier's law ($\vec{q} = -k\nabla T$), heat conduction without temperature gradients implies infinite thermal conductivity. This is clearly impossible. However, if the resistance to conduction within the solid is small compared with the resistance to heat transfer between the solid and its surroundings, the lumped heat capacitance model is sometimes satisfactory [22]. The lumped heat capacitance model uses the following expression for transient problems:

$$-V\rho\frac{de}{dt} = hA_s(T - T_\infty) \tag{5.1}$$

where V is the volume of the solid, e is the specific internal energy, A_s is the surface area of the solid, T is the average temperature of the solid, T_∞ is the freestream temperature of the fluid, and h is the convective heat transfer coefficient. The difficulty in using this model is finding an h that mimics the real multidimensional problem. h is a single constant parameter that is supposed to account for all of the thermodynamic effects due to conditions in the boundary layer, surface geometry, fluid properties, and transport properties

[22].

By performing the lumped heat capacitance calculation and adjusting the h to match certain aspects of the 2D calculation it is possible to roughly approximate it. The question now is which aspects of the 2D calculation are the most logical to use to determine a heat transfer coefficient? Two possibilities were determined to be the most useful, the first was to match the time that the average cross-sectional phase of the 2D SMA reached $\xi_{av} = 0.99$, to the time it takes for the phase of the lumped heat capacitance model to reach the same value. A heat transfer coefficient of $h = 13500\frac{\mathrm{W}}{\mathrm{m^2K}}$ was found using this criteria. A comparison of the temperature histories and a comparison of the phase histories are shown in Figures (5.5) and (5.6) respectively. The temperature history comparison shows that the lumped heat capacitance temperature prediction deviates from the 2D calculation near the start and end of the phase change and is completely different in the late time portion of the history. The phase history comparison shows that the lumped heat capacitance phase consistently differs from the 2D calculation by 8% at any given time throughout most of the actuation until both reach $\xi = 0.99$ where the two were forced to match.

The second method used was to match the late time temperature of the 2D simulation to the lumped heat capacitance approximation to determine the appropriate heat transfer coefficient. A heat transfer coefficient of $h = 10500\frac{\mathrm{W}}{\mathrm{m^2K}}$ was found by choosing to match the lumped heat capacitance approximation temperature at $t = 0.2$s to the temperature of the 2D simulation at $t = 0.2$s, which is $T = 309$K. Figure (5.5) and Figure (5.6) also show the temperture and phase history comparisons for this case. From these histories it is evident that this method of determining a heat transfer coefficient (h) is worse than the previous. We can conclude from these two comparisons that it is nearly impossible to choose a single value of h that can reproduce the complete results of the 2D analysis. Regardless of the lumped heat capacitance approximation's inability to accurately mimic the 2D calculation, the two h's used above could only be determined by performing the complete 2D calculation. That by itself is justification for the multidimensional method used in this work.

The problem of choosing h's expands when actual shape change is considered. In that case the surface areas and cross sectional areas of the SMA wire are changing, leaving the designer with multiple choices to make in an attempt to mimic the true two dimensional calculation. In addition steady state experiments have shown that the value of h is very sensitive to changes in wire diameter [6], [14]. Therefore the validity of using a lumped heat capacitance model on a changing geometry is low.

There is an additional test to measure whether or not a lumped heat capacitance analysis is valid. This is done by computing the Biot number:

$$\mathrm{Bi} = \frac{hL}{k_s} \tag{5.2}$$

where h is the convective heat transfer coefficient, L is the characteristic length (e.g. diameter of wire), and k_s is the thermal conductivity of the solid. The Biot number is the ratio of thermal resistance of the solid to the convective thermal resistance. A lumped heat capacitance model is expected to give acceptable results for $|Bi| \ll 1.0$. Using $h = 13500 \frac{\mathrm{W}}{\mathrm{m^2K}}$ the Biot number is $\mathrm{Bi} = 3.75$ which is well above the required level. Therefore the lumped heat capacitance analysis is not expected to give accurate results by this criteria.

Text resumes on page 128

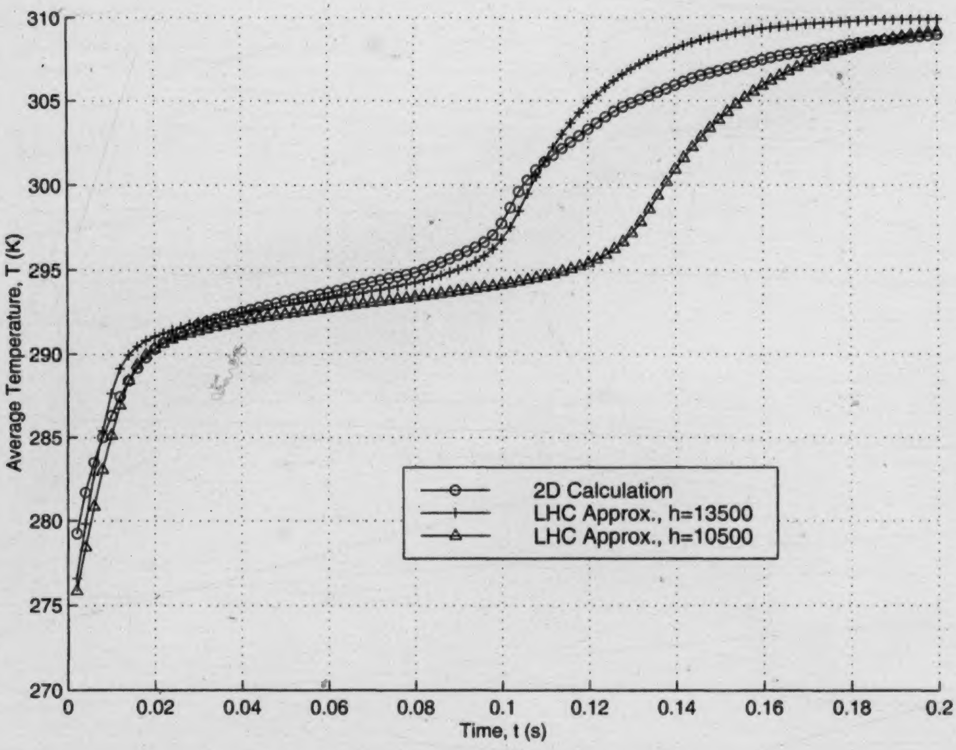

Figure 5.5: Comparison Between Lumped Heat Capacitance and 2D Temperature Histories

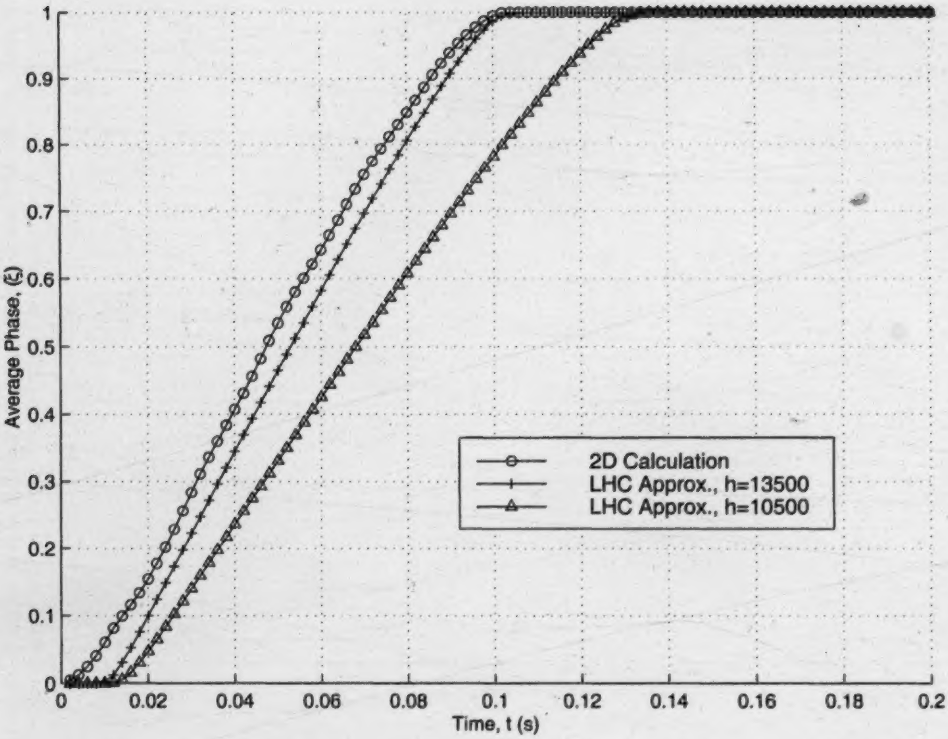

Figure 5.6: Comparison Between Lumped Heat Capacitance and 2D Phase Histories

5.3.3 Simulation of 0.7mm Diameter SMA wire

The second test case run was also with constant geometry. The SMA geometry was a circular cross section with a diameter of 0.7mm. A thicker SMA wire was expected to actuate slower than the thinner 0.5mm case simply due to a decrease in the ratio of circumference to cross-sectional area. In other words there is more solid wall per unit cross-sectional area in contact with the warm fluid in the small circular cross-section than the large circular cross-section. Mathematically the ratio of circumference to area can be displayed for a circle by the following formula:

$$\frac{\text{Circumference}}{\text{Area}} = \frac{\pi D}{\frac{\pi D^2}{4}} = \frac{4}{D} \tag{5.3}$$

where D is the diameter of the circle. The ratios for the small and large circle are 8mm^{-1} and 5.71mm^{-1} respectively. The results confirm this. Figure (5.7) is a comparison plot of the average phase histories. It is evident that the larger diameter wire has a much slower actuation behaviour throughout the actuation history. The maximum difference in actuation time occuring at $\xi = 0.99$ where the time difference was $\Delta t = 0.04$s. A relative difference of 40%.

The vortex shedding frequency for this test case was 51.3Hz, which corresponds to a Strouhal number of 0.359.

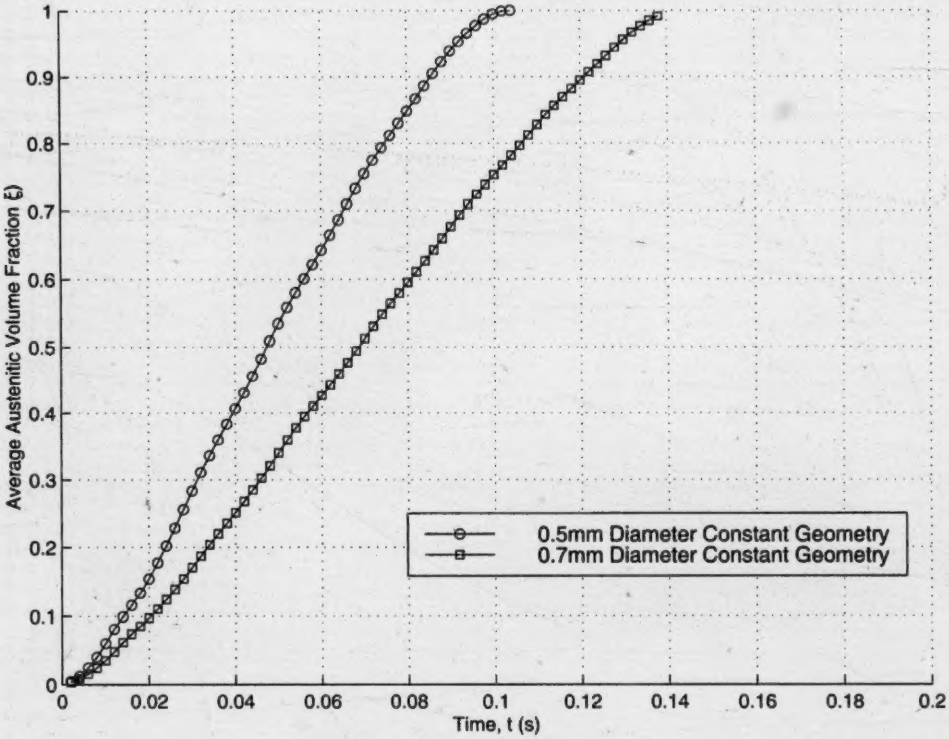

Figure 5.7: Comparison Between Constant Geometry Phase Histories

5.4 SMA Wires Undergoing Shape Change

The effect that shape change has on the actuation behaviours of SMA's is the focus of the present work. The next three test cases shed light on this influence.

5.4.1 Shape Change from Small Diameter to Large Diameter Cross-Section

The first changing geometry test case run was with the SMA wire changing shape from a 0.5mm circular cross section to a 0.7mm cross-section. As discussed in section (1.1), there is no straightforward theoretical or empirical model yet that describes the exact relationship between shape and phase in a two-dimensional sense. A simple idealized linear model was used due to this absence. This absence is acceptable for now since the focus of the current work is the effect of shape change on the thermal fluid-solid interaction. However, the code has the ability to accommodate any shape change model. The model used is a simple linear relationship between diameter and average cross sectional phase:

$$\text{Diameter} = 0.5\text{mm} + (0.7\text{mm} - 0.5\text{mm})\xi_{av} \tag{5.4}$$

where ξ_{av} is the average cross-sectional austenitic volume fraction.

Figures 5.8(a) to 5.8(e), are vorticity contour plots over one period of vortex shedding while the SMA is undergoing shape change. A qualitative comparison with Figures 5.1(a) - 5.1(e) reveals that the movement of the solid boundary has a substantial effect on the flow field that develops. These five plots serve two purposes, firstly to illustrate the actual shape change of the wire, and secondly to illustrate the three major unsteady aspects of the flow. The first being the periodic vortex shedding discussed in section 5.2. The shedding frequency of the small diameter is 54.5Hz and the shedding frequency of the large diameter cross-section is 51.3Hz. These correspond to Strouhal numbers of 0.273 and 0.359 respectively. It is obvious that the resultant shedding frequency of this test case is changing due to the fact that the overall geometry is changing adding further unsteadiness to the shedding phenomena. The second major source of flow unsteadiness is the momentum exchange between the moving solid boundary and the the fluid adjacent to the boundary. The solid boundaries, as they move into the fluid, must "push" the surrounding fluid to move it out of the way, thus exchanging momentum. The final unsteady aspect is the shrinking of the passage between the two wires, thereby transiently affecting the velocities between them.

Recall the difference between the actuation behaviours of the large and small diameter wires from the previous section, see Figure (5.7). Without considering the effect that the shape change induced unsteadiness has on the rate of heat transfer, a reasonable heuristic prediction of the actuation behaviour, for this test case, would be that the phase history should fall somewhere between the two constant geometry simulations.

Consider Figure (5.9), a comparison of average cross-sectional phase histories between the constant geometry test cases and the shape change test case. It is evident that the shape change of the SMA wire in this manner significantly increased the rate of phase change throughout most of the actuation compared to the small diameter constant geometry simulation. This result is quite different than the "reasonable" heuristic prediction above. The difference is due to the transient thermal fluid-solid interaction. These results indicate that this interaction is vitally important to the accurate prediction of actuation times. One cannot simply assume that the geometry, i.e. the circumference to cross-sectional area ratio, is the dominating factor in these transient heating problems. The effect that the shape change has on the fluid solid interaction cannot be ignored.

The average phase history of the shape changing case crosses over the small diameter constant geometry case at $\xi = 0.95$. In a real actuator, most of the useful actuation has taken place before this cross over point. From the beginning of actuation to this cross over point, the changing geometry test case consistently has a higher average phase. The maximum difference being $\Delta\xi = 0.08$, taking place at $t = 0.04$s. The conclusion one could draw from this test case is that designers of circular cross-sectional area actuators can increase the actuation response times if the actuator is designed such that it increases its diameter as it actuates.

Text resumes on page 139

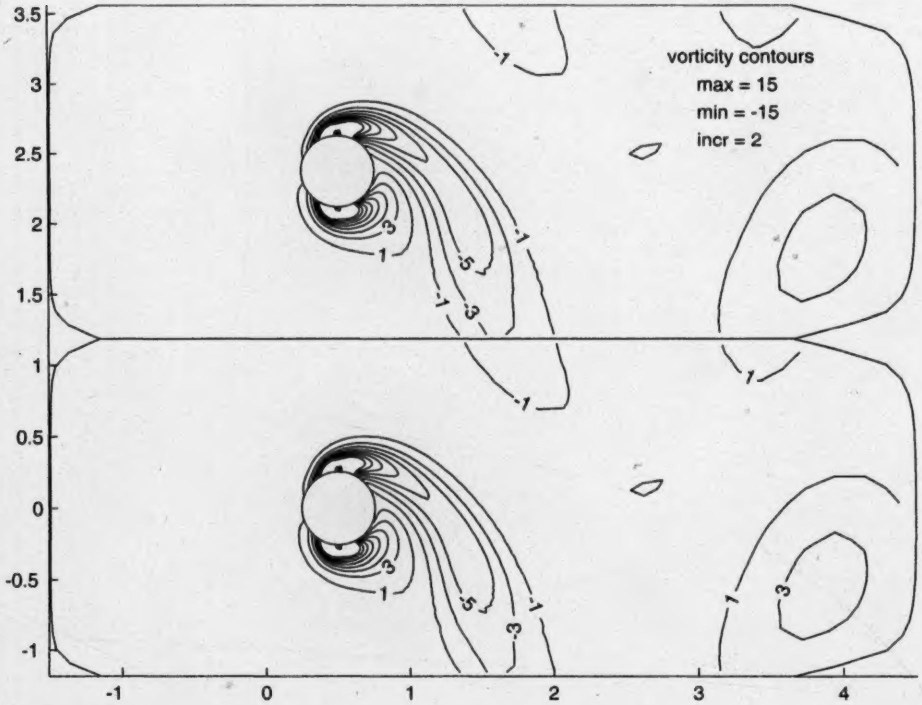

Figure 5.8(a): Small Circle to Large Circle Vorticity Contours, t = 0.008s

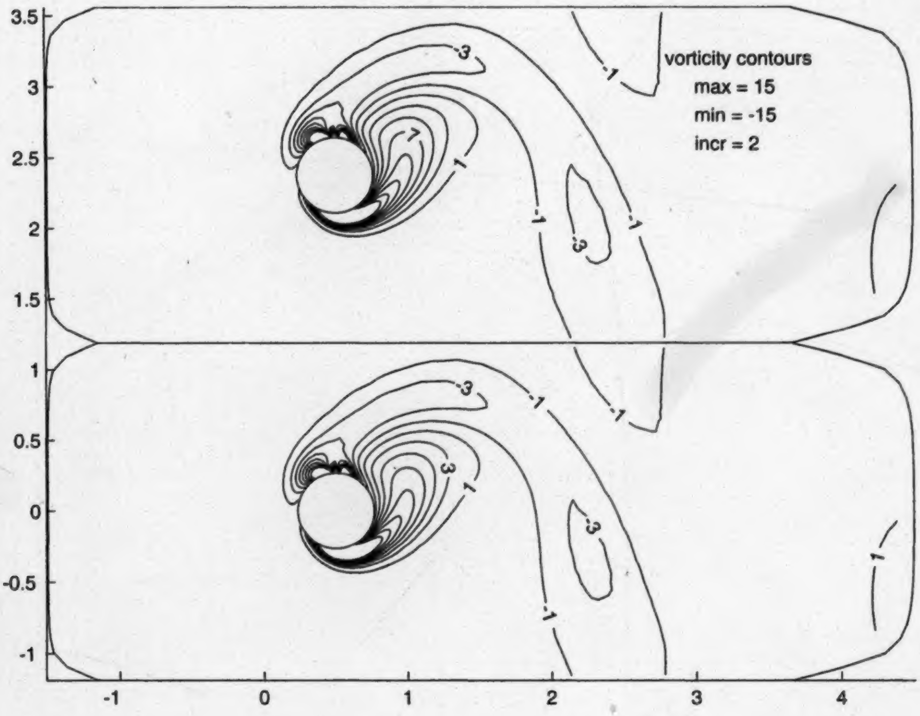

Figure 5.8(b): Small Circle to Large Circle Vorticity Contours, t = 0.016s

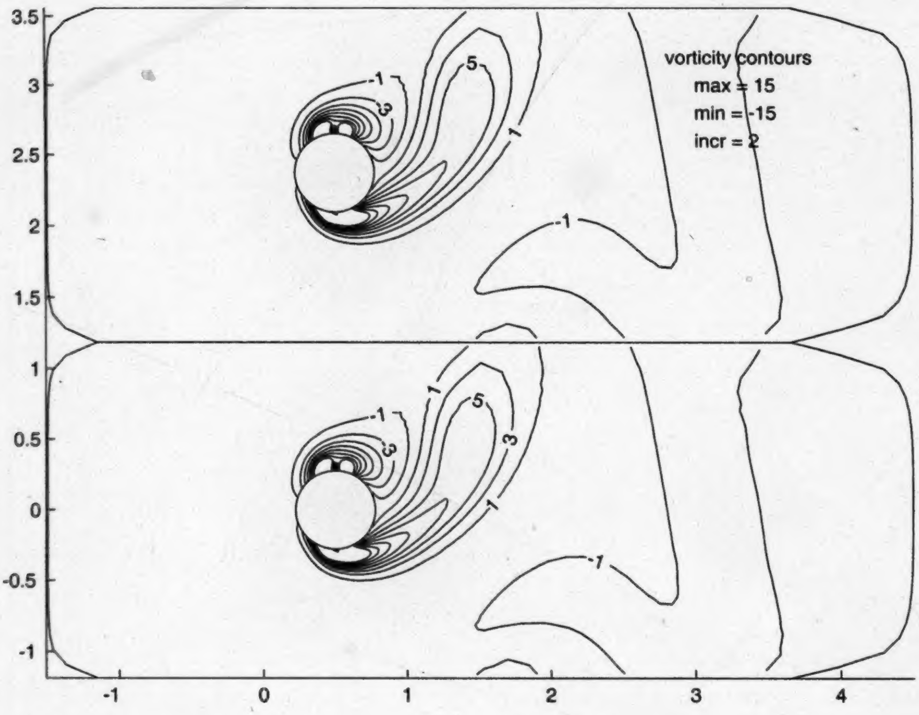

Figure 5.8(c): Small Circle to Large Circle Vorticity Contours, t = 0.024s

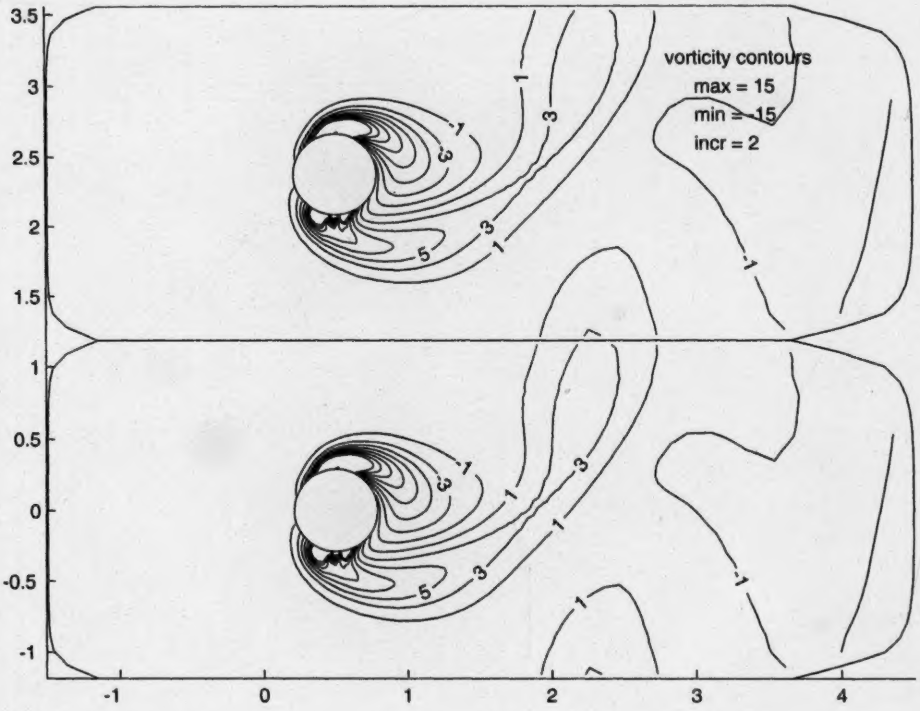

Figure 5.8(d): Small Circle to Large Circle Vorticity Contours, t = 0.032s

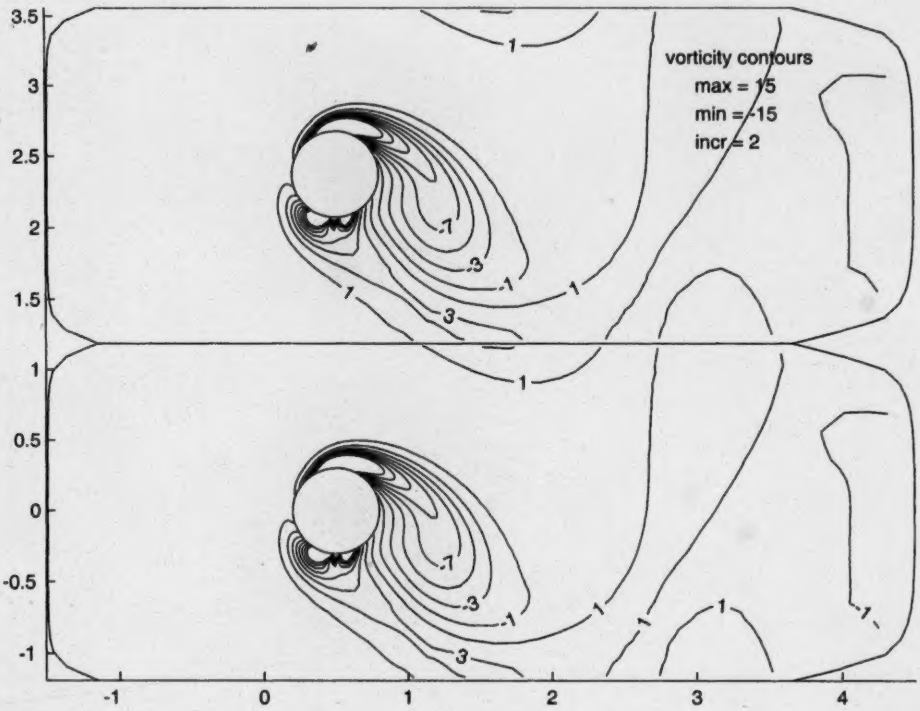

Figure 5.8(e): Small Circle to Large Circle Vorticity Contours, t = 0.040s

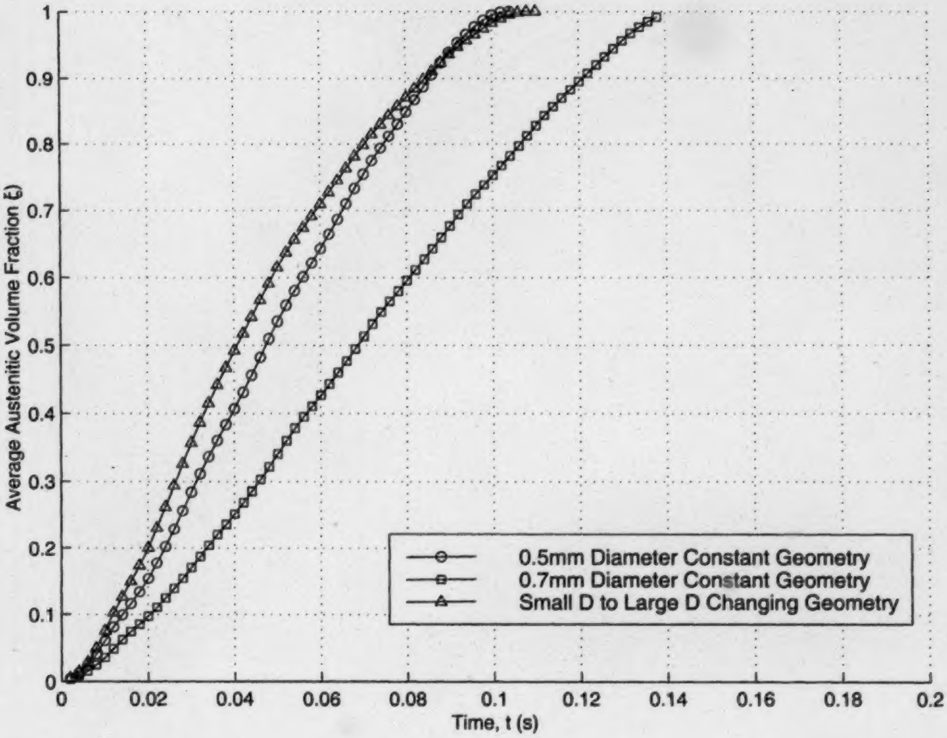

Figure 5.9: Comparison Between Constant and Changing Geometry Phase Histories

5.4.2 Shape Change from Large Diameter to Small Diameter Cross-section

The second changing geometry test case run was to investigate the actuation behaviour of an SMA changing shape from large diameter circle to a small diameter circle. The diameter of the circular wire was changed from 0.7mm to 0.5mm. In exactly the opposite fashion as the previous test case. The model used to determine the diameter based on average cross-sectional phase (ξ_{av}) is:

$$\text{Diameter} = 0.7\text{mm} + (0.5\text{mm} - 0.7\text{mm})\xi_{av} \tag{5.5}$$

The same arguement holds for this test case as the last, a reasonable heuristic prediction would be that it should have an average phase history that is somewhere between the constant geometry test cases. In light of the last test case however, this is probably not the case. Figure (5.10) is a comparison of average cross-sectional phase histories between this test case and the previous three test cases. This comparison shows that the shape change of the SMA wire from large diameter to small diameter significantly reduced the rate of phase change throughout most of the actuation compared to the large diameter constant geometry. Again this is due to the transient thermal fluid-solid interaction. But this time the unsteadiness in the fluid, caused by the shrinking of the solid, actually impeded heat transfer. Thus slowing down the actuation time.

As in the last test case there is a cross over point in the average phase histories at $\xi = 0.94$, however most of the useful actuation will have occured before this point. The average phase is consistently lower than the large diameter constant geometry test case at any given time up to the cross over point. The maximum difference being $\Delta\xi = 0.07$, occuring at $t = 0.062$s. This result indicates that designing a circular cross-section actuator that has a decreasing diameter as it actuates, will result in slower actuation response.

We can conclude from the two changing geometry test cases that if a designer wishes to minimize their circular actuator response times, they should design the actuator such that the diameter is increasing during actuation. Conversely, they could reduce actuation time by doing the opposite, namely have the actuator increase its diameter.

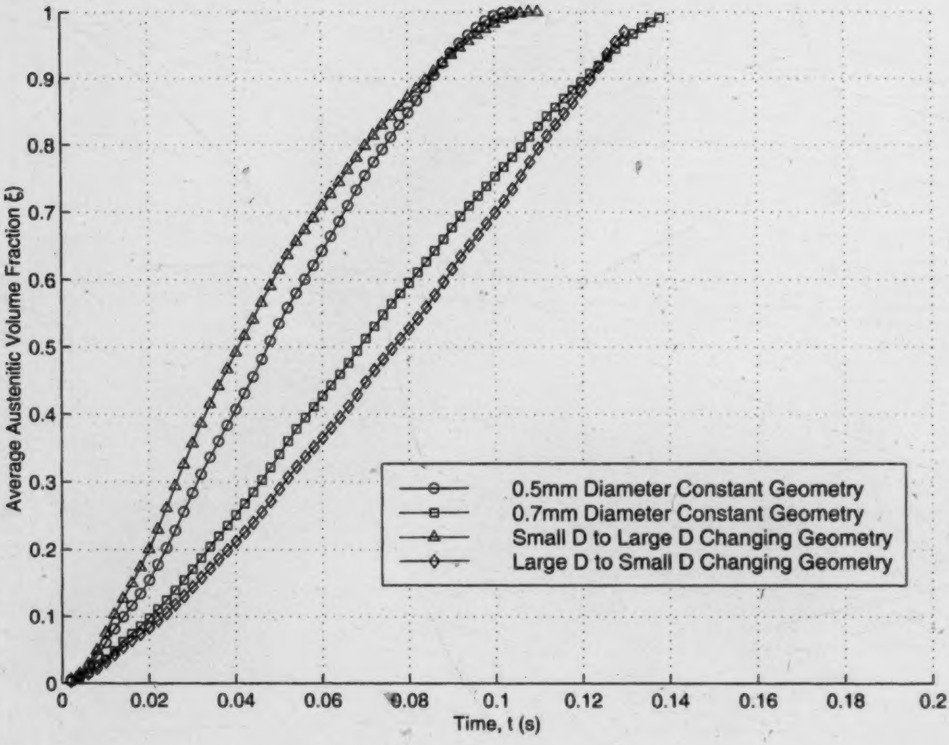

Figure 5.10: Comparison Between Constant and Changing Geometry Phase Histories

5.4.3 Shape Change from Circular Cross-section to an Elliptic Cross-section

The real power and versatility of the code is its ability to accommodate shape changes between any two cross-sectional geometries. This ability is demonstrated through a test case where the cross-sectional shape is changed from a 0.5mm diameter circle, to an ellipse with 1mm long major axis and 0.5mm long minor axis. The cross-sectional area of the ellipse is exactly equal to the cross-sectional area of the 0.7mm diameter circle. The major axis length is dependent upon average phase through the following linear relationship:

$$\text{Length}_{major} = 0.5\text{mm} + (1\text{mm} - 0.5\text{mm})\xi_{av} \tag{5.6}$$

Figures 5.11(a) - 5.11(e) are vorticity contour plots over one period of vortex shedding while the SMA is changing shape. These plots illustrate the shape change of the SMA wire and we can see that the changing shape has a substantial effect on the flow field. This results in different thermal heat transfer rates to the solid and ultimately a different actuation behaviour than the small diameter constant geometry test case.

Figure (5.12) is a plot of the average phase history of this test case compared with the 0.5mm diameter circle test case and the small to large circle changing geometry test case. We can see here that the transformation into an elliptic cross-section substantially increased the rate of phase change throughout the actuation compared to both the constant geometry and changing geometry test case. Again this is an unexpected result if one only considers the change in circumference to cross-sectional area ratios, 8mm^{-1} to 6mm^{-1}, circle to ellipse respectively.

The average phase in this test case is consistently higher than the circle to circle test case throughout the actuation time, meaning that it would actuate the fastest of any of the test cases presented thus far. The maximum phase difference between this test case and the circle to circle test case is $\xi = 0.14$, occuring at $t = 0.036$s. This result indicates that designers could tailor the physical geometries of their actuators to achieve even faster actuation rates than with the circle to circle shape changes.

The types of geometry changes that could be inputted into the code are infinite. It is therefore a powerful tool to designers, allowing them to compare and contrast many shape change geometries.

Text resumes on page 150

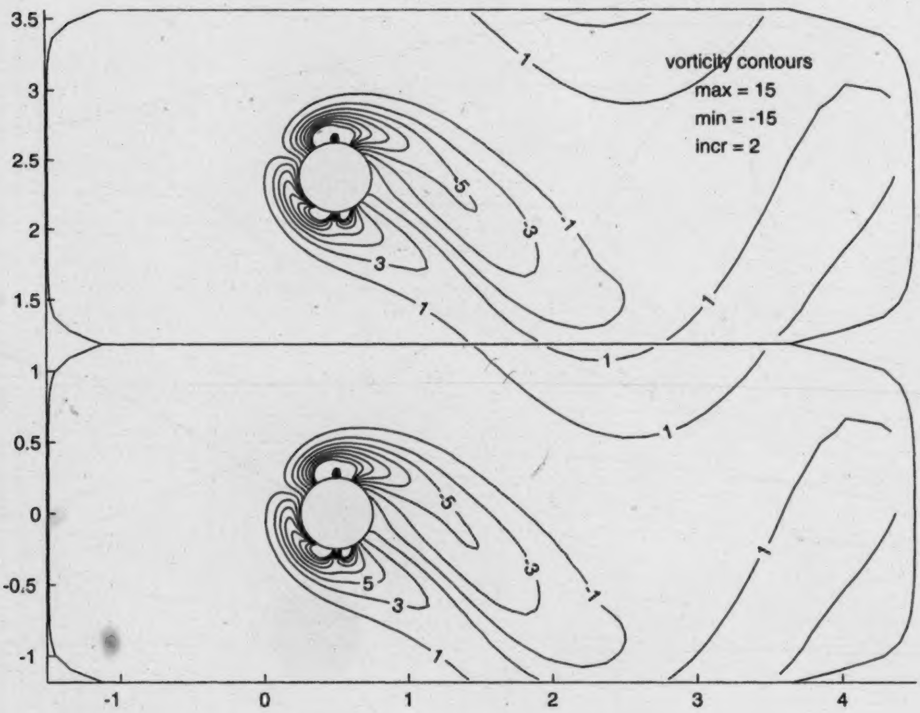

Figure 5.11(a): Circle to Ellipse Vorticity Contours, t = 0.002s

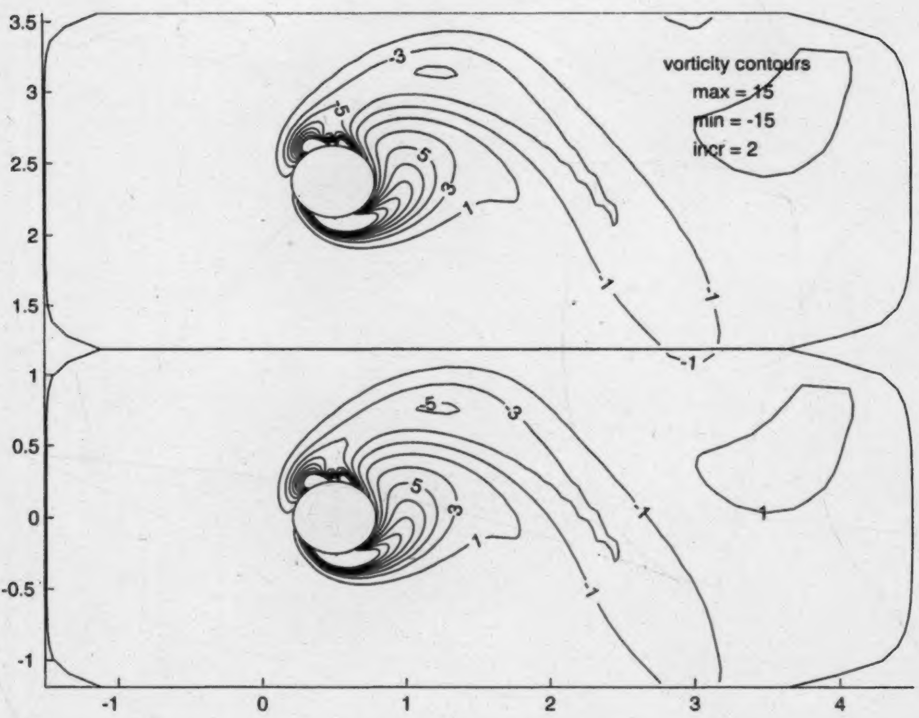

Figure 5.11(b): Circle to Ellipse Vorticity Contours, t = 0.012s

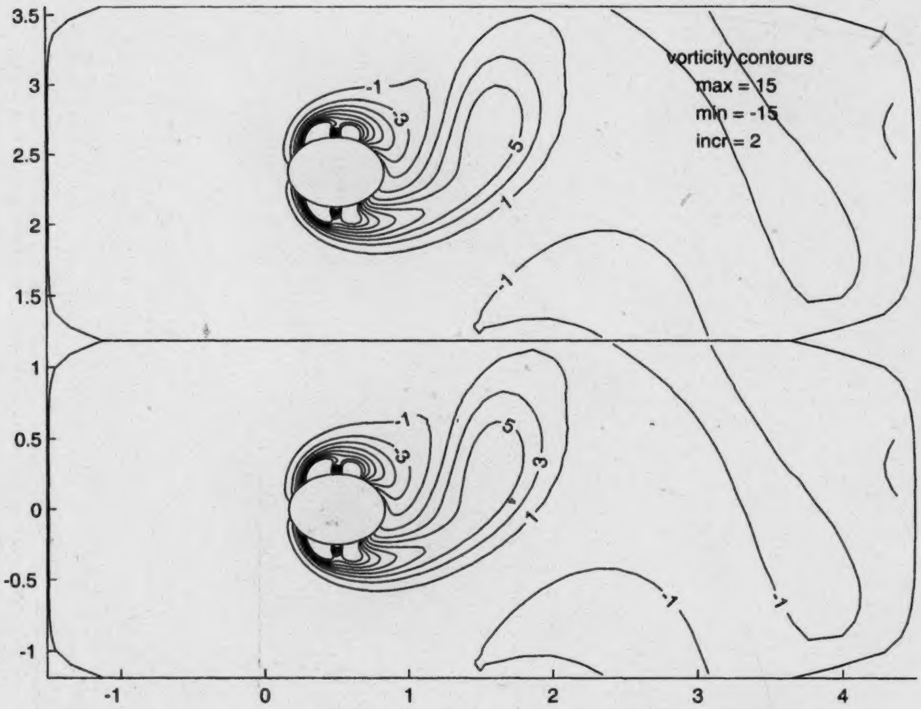

Figure 5.11(c): Circle to Ellipse Vorticity Contours, t = 0.022s

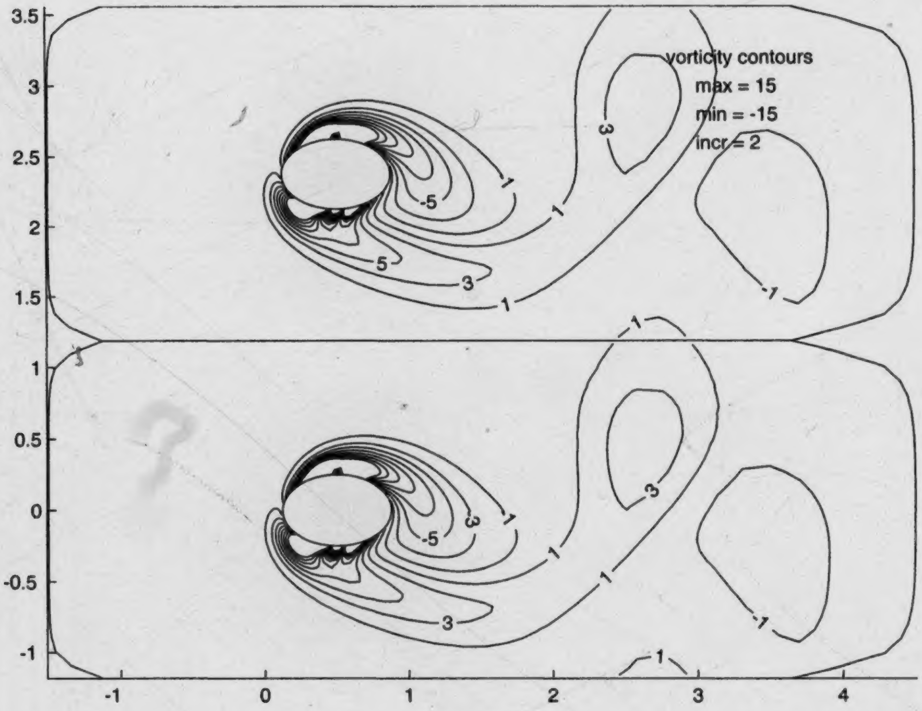

Figure 5.11(d): Circle to Ellipse Vorticity Contours, t = 0.032s

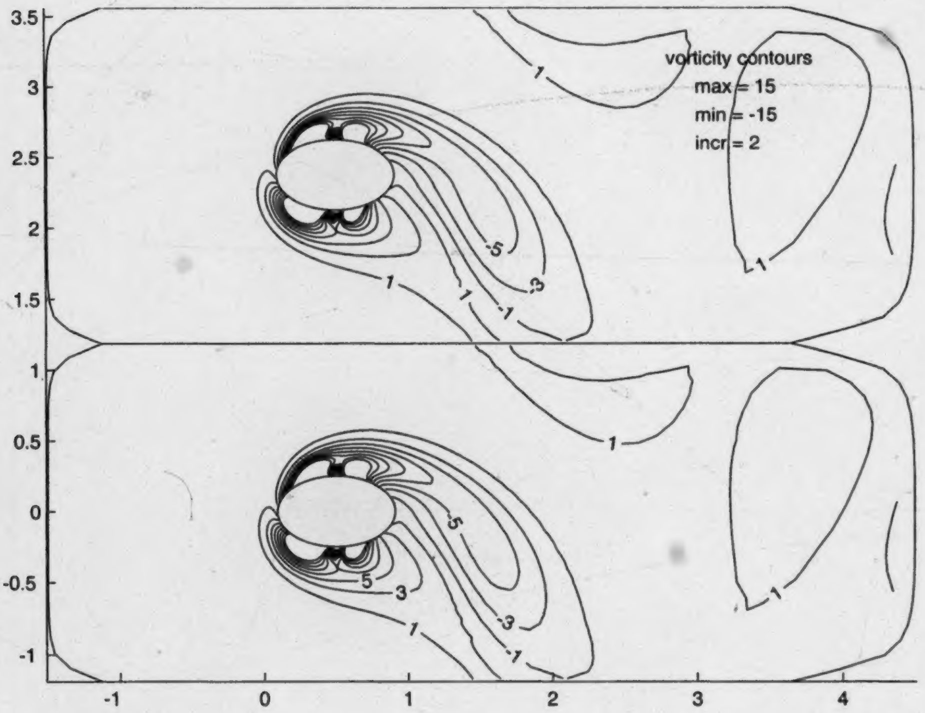

Figure 5.11(e): Circle to Ellipse Vorticity Contours, t = 0.042s

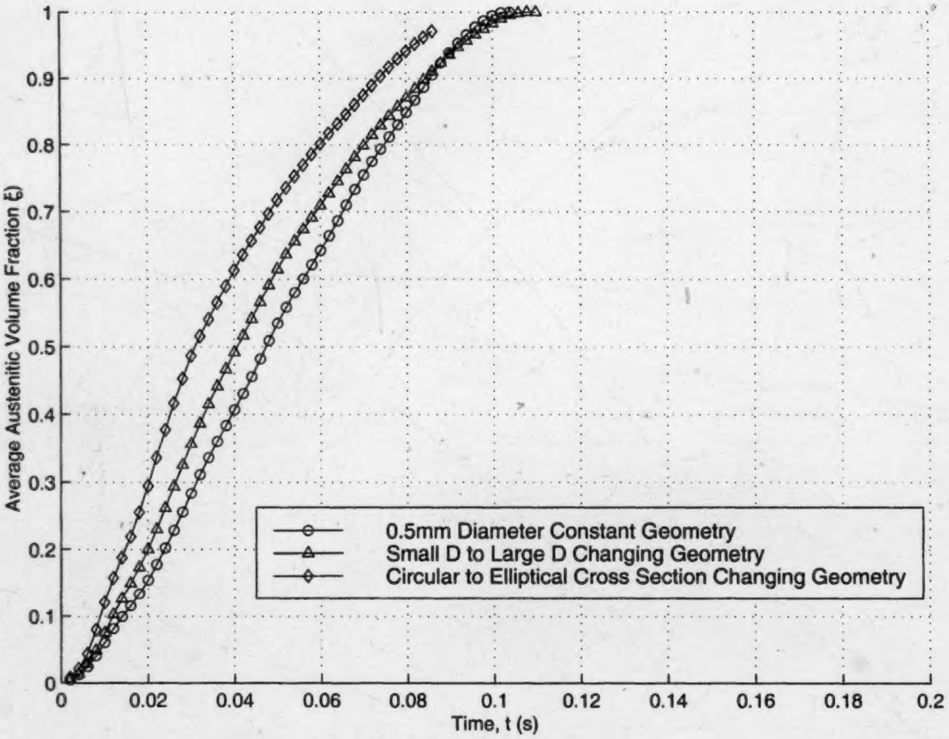

Figure 5.12: Comparison Between Circle to Circle and Circle to Ellipse Changing Geometry Phase Histories

CHAPTER 6

CONCLUSIONS

A numerical scheme has been developed to model the thermal interaction between a low Reynolds number viscous cross flow and a shape memory alloy (SMA) wire undergoing shape change. The material properties of the SMA wire, as well as its shape change, are induced by a solid state phase change. The phase change results from the transient heating of the SMA by the surrounding fluid. The effect that the shape change had on the transient heating and actuation of SMA wires was of primary interest.

As the SMA wire changes shape its solid boundaries move. The movement of these boundaries requires the deformation of the numerical grid. Due to the movement and deformation of individual grid cells the added problem of geometric conservation arises. Mathematically it is described by the so called geometric conservation law, which states that the change in volume of a grid cell with respect to time must be equal to the sum of the volumes swept by each individual grid cell boundary over the same increment of time. Spurious mass sources result if the geometric conservation law is not satisfied. The numerical scheme developed automatically satisfies the geometric conservation law by constructing the grid velocities and geometrics in a geometrically conservative manner. By automatically satisfying the geometric conservation law, the numerical scheme avoids having to explicitly solve the Jacobian transport equation. This is not only more numerically efficient, by performing less calculations, but is more logical due to the fact that the geometric conservation law is not a physical transport equation, and should not be treated as such.

Boundary conditions were applied that accurately modeled the interaction of the solid surface with the flow. A no-flux condition was applied at the solid wall that stated that the difference between the fluid and solid boundary velocities normal to the wall was zero. A no-slip condition was applied at the solid wall that stated that the difference between the fluid and solid velocities parallel to the wall was zero. The combination of these two boundary conditions allowed for the transfer of momentum between the solid and fluid. The added unsteadiness due to this motion was expected to have a substantial influence on the heat transfer between the SMA and the fluid.

The energy equation was solved in both the fluid and the solid. Therefore, a thermal boundary condition was used that calculated the heat flux between the fluid and solid based on temperatures adjacent to the solid boundary. This thermal boundary condition represents the real physics of the thermal interaction between a solid and a fluid. It does not rely on prescribing heat fluxes, temperatures, or heat transfer coefficients.

The phase of the SMA was expressed as a function of the temperature based on an existing constitutive model and approximation. The local phase of the SMA was used to compute the locally changing thermal conductivity.

The area weighted average phase was used to track the actuation behaviour of the SMA wires. It was also used to determine the shape of the SMA based on an idealized shape change model. The shape change model was chosen arbitrarily due to the absence of one in the literature. The numerical scheme is robust enough to accommodate any model that may be developed.

Five test cases were presented to demonstrate the effect that shape change has on the transient actuation behaviour of SMA wires. Two of the test cases involved simulating constant geometry SMA wires with large and small diameter circular cross-sections. Two of the test cases involved simulating the shape change between those two constant circular geometries. The final test case showed the effect of changing shape between two dissimilar cross-sectional shapes.

The constant geometry test cases showed that the small diameter cross-section actuated faster than the large-diameter cross section. The small diameter test case was compared to a lumped heat capacitance analysis. It was shown that using this simple analysis it was impossible to accurately mimic the two dimensional solution. The difficulty lied in the fact that a single constant, namely the convective heat transfer coefficient, was supposed to account for all of the complicated thermodynamic effects caused by the boundary layer, surface geometry, fluid properties, and transport properties. This problem would be further compounded when a changing geometry is considered.

The constant geometry phase histories were compared to the changing geometry test case who's diameter changed from small to large. This test case changed phase considerably faster, for most of its actuation, than the small diameter constant geometry. So by allowing the SMA actuator to change shape in this manner, a higher rate of actuation was achieved. The higher actuation rate is due to greater heat transfer caused by the thermal fluid-solid interaction. One can conclude that designers who desire faster actuation times should engineer cross-sections that increase in diameter as they change phase.

The reverse was found to be true when the shape changed from an SMA wire with a large diameter cross-section to a small diameter cross-section. This wire had slower actuation rates than the large diameter constant geometry test case. From this we can conclude that designers who desire slower actuation times could engineer their geometries such that the diameters decrease with phase change.

The final test case was with a cross-sectional geometry that changed from a small diameter circle to an ellipse, two dissimilar cross-sections. This SMA wire actuated the fastest, substantially faster than the small circle to large circle test case. Thus indicating that designers could further control the actuation behaviours by engineering completely different geometries. The robustness of the numerical code allows for the testing of any cross-sectional geometry change. Therefore making it an excellent tool, allowing designers to explore the effect different shape changes have on actuation behaviour.

A possibility for future work would be to incorporate a localized shape change model into the code. The reality is that the SMA would most likely change phase locally rather than in global sense that is based on the average phase. Unfortunately the material science has yet to provide a robust two-dimensional local shape change model that could be used.

An additional possibility for future work would be to add in a localized residual stress model. As each polycrystal changes phase they change shape locally. Since the polycrystals cannot move relative to each other a stress field would be established at their boundaries, analogous to press fit cylinders. This would in turn affect the temperatures at which phase change occur, and would likely have a significant effect on actuation behaviour.

BIBLIOGRAPHY

[1] Amalraj, J., Bhattacharyya, A., Faulkner, M.G. "Finite Element Modeling of Phase Transformation in Shape Memory Alloy Wires with Variable Material Properties," *Jounal of Smart Materials and Structures* vol.9, pp.622-631, 2000.

[2] Anderson, J.D. *Computational Fluid Dynamics, the Basics with Applications.* McGraw Hill Inc., New York, New York, 1995.

[3] Barrett, R., Farokhi, S., "Subsonic Aerodynamics and Performance of a Smart Vortex Generator System," *Journal of Aircraft*, vol.33, no.2, pp.393-398, 1996.

[4] Bein, T., Hanselka, H., Breitbach, E., "An Adaptive Spoiler to Control the Transonic Shock," *Journal of Smart Materials and Structures*, vol.9, pp.141-148, 2000.

[5] Bhattacharyya, A., Lagoudas, D.C., "A Stochastic Thermodynamic Model for the Gradual Thermal Transformation of SMA Polycrystals," *Journal of Smart Materials and Structures*, vol.6, pp.235-250, 1997.

[6] Bhattacharyya, A., Sweeney, L., Faulkner, M.G., "Experimental Characterization of Free Convection During Thermal Phase Transformations

in Shape Memory Alloy Wires," *Journal of Smart Materials and Structures*, vol.11, pp.411-422, 2002.

[7] Bhattacharyya, A., Faulkner, M.G., Amalraj, J., "Finite Element Modeling of Cyclic Thermal Response of Shape Memory Alloy Wires with Variable Material Properties," *Journal of Computational Materials Science*, vol.17, pp.93-104, 2000.

[8] Birman, V., "Review of Mechanisms of Shape Memory Alloy Structures," *Applied Mechanics Reviews*, vol.50, no.11, pt.1, pp.629-645, 1997.

[9] Boyd, J.G., Lagoudas, D.C., "A Thermodynamical Constitutive Model for Shape Memory Materials. Part I. The Monolithic Shape Memory Alloy," *International Journal of Plasticity*, vol.12, no.6, pp.805-841, 1996.

[10] Buehler, W.J., Gilfrich, J.V., Wiley, R.C., "Effect of Low-Temperature Phase Changes on the Mechanical Properties of Alloys near Composition TiNi," *Journal of Applied Physics*, vol.34, no. 5, pp.1475-1477, 1963.

[11] Chandrasekhar, S. *Hydrodynamic and Hydromagnetic Stability*. Oxford University Press, London, 1961.

[12] Chang, K.S., Sa, J.Y., "The Effect of Buoyancy on Vortex Shedding in the Near Wake of a Circular Cylinder," *Journal of Fluid Mechanics*, vol.220, pp.253-266, 1990.

[13] Chonan, S., Jiang, Z., Tani, J., Orikasa, S., Tanahashi, Y., Takagi, T., Tanaka, M., Tanikawa, J., "Development of an Artificial Uretheral

Valve Using SMA Actuators," *Journal of Smart Materials and Structures*, vol.6, pp.410-414, 1997.

[14] Churchill, S.W., Chu, H.H.S., "Correlating Equations for Laminar and Turbulent Free Convection From a Horizontal Cylinder," *International Journal of Heat and Mass Transfer*, vol.18, pp.1049-1053, 1975.

[15] Demirdžić, I., Perić, M., "Space Conservation Law in Finite Volume Calculations of Fluid Flow," *International Journal for Numerical Methods in Fluids*, vol.8, pp.1037-1050, 1988.

[16] Demirdžić, I., Perić, M., "Finite Volume Method for Prediction of Fluid Flow in Arbitrarily Shaped Domains with Moving Boundaries," *International Journal for Numerical Methods in Fluids*, vol.10, pp.771-790, 1990.

[17] Dubuc, L., Cantariti, F., Woodgate, M., Gribben, B., Badcock, K., Richards, B., "A Grid Deformation Technique for Unsteady Flow Computations," *International Journal for Numerical Methods in Fluids*, vol.32, pp.285-311, 2000.

[18] Duerig, T.W., Stöckel, D., Keeley, A., "Actuator and Work Production Devices," *Engineering Aspects of Shape Memory Alloys*, Duerig, T.W., Melton, K.N., Stöckel, D., Wayman, C.M. (eds), Butterworth - Heinemann, London, England, 1990.

[19] Dütsch, H., Melling, A., Durst, F., "Coupled Numerical Computations of the Fluid Damped Oscillations of a Lamina," *University of Erlangen-Nurmberg Internal Publication*, Erlangen, Germany, 2002.

[20] Faulkner, M.G., Amalraj, J.J., Bhattacharyya, A., "Experimental Determination of Thermal and Electrical Properties of Ni-Ti Shape Memory Wires," *Journal of Smart Materials and Structures*, vol.9, pp.632-639, 2000.

[21] Harten, A., Osher, S., "Uniformly Higher-Order Accurate Nonoscillatory Schemes I," *SIAM Journal of Numerical Analysis*, vol.24, pp.279-309, 1987.

[22] Incropera, F.P., Dewitt, D.P., *Introduction to Heat Transfer*. John Wiley & Sons, New York, New York, 1996.

[23] Jain, P.C., Goel, B.S., "A Numerical Study of Unsteady Laminar Forced Convection From a Circular Cylinder," *Transactions of the ASME, Journal of Heat Transfer*, vol.98, pp.303-307, 1976.

[24] Jaluria, Y., Torrance, K., *Computational Heat Transfer*. Hemisphere Publishing, Washington D.C., 1986.

[25] Janus, J.M., Hortzman, H.Z., Whitfield, D.L., "Unsteady Flowfield Simulation of Ducted Prop-Fan Configurations," *Journal of Propulsion and Power*, vol.15, no.1, pp.64-72, 1999.

[26] Jonnalagadda, K.D., Sottos, N.R, Qidwai, M.A., Lagoudas, D.C., "In Situ Displacement Measurements and Numerical Predictions of Embedded SMA Transformation," *Journal of Smart Materials and Structures*, vol.9, pp.701-710, 2000.

[27] Karanth, D., Rankin, G.W., Sridhar, K., "A Finite Difference Calculation of Forced Convective Heat Transfer from an Oscillating Cylinder,"

International Journal of Heat and Mass Transfer, vol.37, no.11, pp.1619-1630, 1994.

[28] Keefe, A.C., Carman, G.P., "Thermo-mechanical Characterization of Shape Memory Alloy Torque Tube Actuators," *Journal of Smart Materials and Structures*, vol.9, pp.665-672, 2000.

[29] Khattacharyya, K., Kohn, R.V., "Symmetry, Texture and the Recoverable Strain of Shape-Memory Polycrystals," *Acta materiala*, vol.44, no.2, pp.529-542, 1996.

[30] Lagoudas, D.C., Bhattacharyya, A., "Modeling of Thin Layer Extensional Thermoelectric SMA Actuators," *International Journal of Solids and Structures*, vol.35, pp.331-362, 1997.

[31] Lacroix, M., "Predictions of Natural-Convection-Dominated Phase-Change Problems by the Vorticity-Velocity Formulation of the Navier-Stokes Equations," *Numerical Heat Transfer, Part B*, vol.22, pp. 79-93, 1992.

[32] Lee, H.J., Lee, J.L., "Evaluation of the Characteristics of a Shape Memory Alloy Spring Actuator," *Journal of Smart Materials and Structures*, vol.9, pp.817-823, 2000.

[33] Marquart, J.E., Eastep, F.E., "Numerical Representation of Pitching and Non-pitching Airfoils Undergoing Linear Acceleration," *Journal of Aircraft*, vol.35, no.5, pp.761-768, 1998.

[34] Matsuzaki, Y., Naito, H., Ikeda, T., Funami, K., "Thermo-mechanical Behaviour Associated with Pseudoelastic Transformation of Shape

Memory Alloys," *Journal of Smart Materials and Structures*, vol.10, pp.884-892, 2001.

[35] Melton, K.N., "Ni-Ti Based Shape Memory Alloys," *Engineering Aspects of Shape Memory Alloys*, Duerig, T.W., Melton, K.N., Stöckel, D., Wayman, C.M. (eds), Butterworth - Heinemann, London, England, 1990.

[36] Miller, D., Lagoudas, D., "Thermomechanical Characterization of NiTiCu and NiTi SMA Actuators: Influence of Plastic Strains," *Journal of Smart Materials and Structures*, vol.9, pp.640-652, 2000.

[37] Nguyen, H.D., Paik, S., Douglass, R.W., "Unsteady Mixed Convection about a Rotating Circular Cylinder with Small Fluctuations in the Free-Stream Velocity," *International Journal of Heat and Mass Transfer*, vol.39, no.3, pp.511-525, 1996.

[38] Panton, R. *Incompressible Flow*. John Wiley & Sons Inc, New York, New York, 1996.

[39] Perkins, J., Hodgson, D., "The Two-Way Shape Memory Effect," *Engineering Aspects of Shape Memory Alloys*, Duerig, T.W., Melton, K.N., Stöckel, D., Wayman, C.M. (eds), Butterworth - Heinemann, London, England, 1990.

[40] Purdy, G.R., Parr, J.G., "A Study of the Titanium-Nickel System Between Ti_2Ni and TiNi," *Transactions of the Metallurgical Society of AIME*, vol.22, pp.636-639, 1961.

[41] Ramachandran, N., Gupta, J.P., Jaluria, Y., "Thermal and Fluid Flow Effects During Solidification in a Rectangular Enclosure", *International Journal of Heat and Mass Transfer*, vol. 25, no. 2, pp.187-194, 1982.

[42] Reaume, C.T., "Numerical Investigation of the Thermal Interaction between a Shape Memory Alloy and a Low Reynolds Number Viscous Flow", *M.Sc. Thesis*, University of Alberta, 2000, Edmonton, Alberta, Canada

[43] Saadat, S., Noori, M., Davoodi, H., Hou, Z., Suzuki, Y., Masuda, A. "Using NiTi Tendons for Vibration Control of Coastal Structures," *Journal of Smart Materials and Structures*, vol.10, pp.695-704, 2001.

[44] Schneider, G.E., LeDain, B.L. "Fully Developed Laminar Heat Transfer in Triangular Passages," *Journal of Energy*, vol.5, no.1, pp.15-21, 1981.

[45] Serrin, J., "Mathematical Principles of Classical Fluid Mechanics," *Encyclopedia of Physics*, Flugge, S., ed., Springer Verlag, Berlin, vol.VIII/1, pp.125-263, 1959.

[46] Shahin, A.R., Meckl, P.H., Jones, J.D., "Enhanced Cooling of Shape Memory Alloy Wires Using Semiconductor "Heat Pump" Modules," *Journal of Intelligent Material Systems and Structures*, vol.5, pp.95-104, 1994.

[47] Shaw, J.A., Kyriakides, S. "Thermomechanical Aspects of NiTi," *Journal of the Mechanics and Physics of Solids*, vol.43, pp.1243-1281, 1995.

[48] Sheu, T., Chen, H., "A Transient Analysis of Incompressible Fluid Flow in Vessels with Moving Boundaries," *International Journal of Numerical Methods for Heat and Fluid Flow*, vol.9, no.8, pp.833-846, 1999.

[49] Shyy, W., Pal, S., Udaykumar, H.S., Choi, D. "Structured Moving Grid and Geometric Conservation Laws for Fluid Flow Computation," *Numerical Heat Transfer, Part A*, vol.34, pp.369-397, 1998.

[50] Simon, M., Kaplow, R., Salzman, E., Freiman, D., "A Vena Cava Filter Using Thermal Memory Alloy," *Radiology*, vol.125, pp.89-94, 1977.

[51] Song, C., Campbell, P.A., Frank, T.G., Cuschieri, A., "Thermal Modeling of Shape Memory Alloy Fixator for Medical Application," *Journal of Smart Materials and Structures*, vol.11, pp.312-316, 2002.

[52] Thomas, P.D., Lombard, C.K., "Geometric Conservation Law and Its Application to Flow Computations on Moving Grids," *AIAA Journal*, vol.17, no.10, pp.1030-1037, 1979.

[53] Thompson, J.F., Warsi, Z.U.A, Mastin, C.W., *Numerical Grid Generation, Foundations and Applications.* Elsevier Science Publishing Co. Inc., New York, New York, 1985.

[54] Troisfontaine, N., Bidaud, P., Larnicol, M. "Optimal Design of Micro-Actuators Based on SMA Wires," *Journal of Smart Materials and Structures*, vol.8, pp.197-203, 1999.

[55] van Leer, B. "Towards the Ultimate Conservative Difference Scheme II, Monoticity and Conservation Combined in a Second Order Scheme," *Journal of Computational Physics*, vol.14, pp.361-370, 1974.

[56] Victor, S.A., Shah, V.L. "Steady State Heat Transfer to Blood Flowing in the Entrance Region of a Tube," *International Journal of Heat and Mass Transfer*, vol.19, pp.777-783, 1975.

[57] Vishwanath, R., and Jaluria, Y., "A Comparison of Different Solution Methodologies for Melting and Solidification Problems in Enclosures," *Numerical Heat Transfer Part B: Fundamentals*, vol. 24, pp. 77-105, 1993.

[58] Wang, P., Kahawita, R., Nguyen, T.H., "Numerical Computation of the Natural Convection Flow About a Horizontal Cylinder using Splines," *Numerical Heat Transfer, Part A*, vol.17, pp.191-215, 1990.

[59] Warsi, Z.U.A., "Conservation Form of the Navier-Stokes Equations in General Nonsteady Coordinates," *AIAA Journal*, vol.19, no.2, pp.240-242, 1981.

[60] Wayman, C.M., Duerig, T.W., "An Introduction to Martensite and Shape Memory," *Engineering Aspects of Shape Memory Alloys*, Duerig, T.W., Melton, K.N., Stöckel, D., Wayman, C.M. (eds), Butterworth - Heinemann, London, England, 1990.

[61] Williamson, C.H.K., "Oblique and Parallel Modes of Vortex Shedding in the Wake of a Circular Cylinder at Low Reynolds Numbers," *Journal of Fluid Mechanics*, vol.206, pp.579-627, 1989.

[62] Yokota, J.W. "An L-U Implicit Multigrid Algorithm to Solve the Euler Equations for Transonic Flow in Rotating Turbomachinery Passages," Ph.D. Thesis, Cornell University, 1987.

[63] Yokota, J.W. "Vorticity Dynamics of Inviscid Shear Layers," *AIAA Journal*, vol.31, no.8, pp.1430-1439, 1993.

[64] Yokota, J.W. "Unsteady Blade-Row Vortex Interaction," *Canadian Aeronautics and Space Journal*, vol.44, no.1, pp.25-32, 1998.

[65] Yokota, J.W. "A Kinematic Velocity Decomposition of Stratified Flow," *International Journal of Computational Fluid Dynamics*, vol.9, pp.122-135, 1998.

[66] Zwart, P.J., Raithby, G.D., Raw, M.J., "An Integrated Space-Time Finite Volume Method for Moving Boundary Problems," *Numerical Heat Transfer, Part B*, vol.34, pp.257-270, 1998.